

University of Warwick institutional repository: <http://go.warwick.ac.uk/wrap>

A Thesis Submitted for the Degree of PhD at the University of Warwick

<http://go.warwick.ac.uk/wrap/49630>

This thesis is made available online and is protected by original copyright.

Please scroll down to view the document itself.

Please refer to the repository record for this item for information to help you to cite it. Our policy information is available from the repository home page.

Library Declaration and Deposit Agreement

1. STUDENT DETAILS

Full name: **Wojciech M. Linhart**

University ID number: **0859435**

2. THESIS DEPOSIT

2.1 I understand that under my registration at the University, I am required to deposit my thesis with the University in BOTH hard copy and in digital format. The digital version should normally be saved as a single pdf file.

2.2 The hard copy will be housed in the University Library. The digital version will be deposited in the University's Institutional Repository (WRAP). Unless otherwise indicated (see 2.3 below) this will be made openly accessible on the Internet and will be supplied to the British Library to be made available online via its Electronic Theses Online Service (EThOS) service. [At present, theses submitted for a Masters degree by Research (MA, MSc, LLM, MS or MMedSci) are not being deposited in WRAP and not being made available via EThOS. This may change in future.]

2.3 In exceptional circumstances, the Chair of the Board of Graduate Studies may grant permission for an embargo to be placed on public access to the hard copy thesis for a limited period. It is also possible to apply separately for an embargo on the digital version. (Further information is available in the Guide to Examinations for Higher Degrees by Research.)

2.4 *If you are depositing a thesis for a Masters degree by Research, please complete section (a) below. For all other research degrees, please complete both sections (a) and (b) below:*

(a) Hard Copy

I hereby deposit a hard copy of my thesis in the University Library to be made publicly available to readers (please delete as appropriate) EITHER immediately OR after an embargo period of months/years as agreed by the Chair of the Board of Graduate Studies

I agree that my thesis may be photocopied.

YES / NO (*Please delete as appropriate*)

(b) Digital Copy

I hereby deposit a digital copy of my thesis to be held in WRAP and made available via EThOS

Please choose one of the following options:

EITHER My thesis can be made publicly available online.

YES / NO (*Please delete as appropriate*)

OR My thesis can be made publicly available only after..[date] (Please give date)

YES / NO (*Please delete as appropriate*)

OR My full thesis cannot be made publicly available online but I am submitting a separately identified additional, abridged version that can be made available online.

YES / NO (*Please delete as appropriate*)

OR My thesis cannot be made publicly available online.

YES / NO (*Please delete as appropriate*)

3. GRANTING OF NON-EXCLUSIVE RIGHTS

Whether I deposit my Work personally or through an assistant or other agent, I agree to the following:

Rights granted to the University of Warwick and the British Library and the user of the thesis through this agreement are non-exclusive. I retain all rights in the thesis in its present version or future versions. I agree that the institutional repository administrators and the British Library or their agents may, without changing content, digitise and migrate the thesis to any medium or format for the purpose of future preservation and accessibility.

4. DECLARATIONS

(a) I DECLARE THAT:

- I am the author and owner of the copyright in the thesis and/or I have the authority of the authors and owners of the copyright in the thesis to make this agreement. Reproduction of any part of this thesis for teaching or in academic or other forms of publication is subject to the normal limitations on the use of copyrighted materials and to the proper and full acknowledgement of its source.
- The digital version of the thesis I am supplying is the same version as the final, hard-bound copy submitted in completion of my degree, once any minor corrections have been completed.
- I have exercised reasonable care to ensure that the thesis is original, and does not to the best of my knowledge break any UK law or other Intellectual Property Right, or contain any confidential material.
- I understand that, through the medium of the Internet, files will be available to automated agents, and may be searched and copied by, for example, text mining and plagiarism detection software.

(b) IF I HAVE AGREED (in Section 2 above) TO MAKE MY THESIS PUBLICLY AVAILABLE DIGITALLY, I ALSO DECLARE THAT:

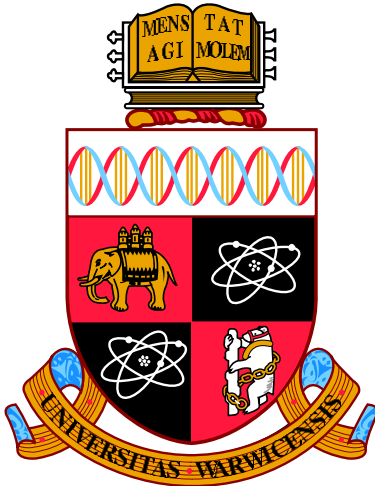
- I grant the University of Warwick and the British Library a licence to make available on the Internet the thesis in digitised format through the Institutional Repository and through the British Library via the EThOS service.
- If my thesis does include any substantial subsidiary material owned by third-party copyright holders, I have sought and obtained permission to include it in any version of my thesis available in digital format and that this permission encompasses the rights that I have granted to the University of Warwick and to the British Library.

5. LEGAL INFRINGEMENTS

I understand that neither the University of Warwick nor the British Library have any obligation to take legal action on behalf of myself, or other rights holders, in the event of infringement of intellectual property rights, breach of contract or of any other right, in the thesis.

Please sign this agreement and return it to the Grade School Office when you submit your thesis.

Student's signature: Date:



Electron accumulation and doping in InN and InGaN alloys

by

Wojciech M. Linhart

Thesis

Submitted to the University of Warwick

for the degree of

Doctor of Philosophy

Department of Physics

May 2012

THE UNIVERSITY OF
WARWICK

Contents

Acknowledgments	iv
Declarations	v
Abstract	ix
Abbreviations and common symbols	x
List of Figures	xiv
1 Introduction	1
1.1 Why group-III nitride semiconductors?	1
1.2 Crystal structure	2
1.3 Band gap and energy band structure	6
1.4 Surface states and the charge neutrality level	10
1.5 Doping of InN and $\text{In}_x\text{Ga}_{1-x}\text{N}$	14
1.5.1 Unintentional and intentional <i>n</i> -type doping of InN and $\text{In}_x\text{Ga}_{1-x}\text{N}$	15
1.5.2 <i>p</i> -type doping of InN and $\text{In}_x\text{Ga}_{1-x}\text{N}$	15
1.6 Control of surface electron accumulation	17
1.7 Thesis organisation	18
2 Theoretical Background	19
2.1 Band structure approximations	19
2.1.1 Parabolic approximation	21
2.1.2 $\mathbf{k} \cdot \mathbf{p}$ perturbation theory	21
2.2 Space charge calculations	27
2.2.1 Poisson's equation	27
2.2.2 Modified Thomas-Fermi approximation	28
2.3 Summary	30

3 Experimental and computational methods	31
3.1 X-ray photoemission spectroscopy	31
3.1.1 Background	34
3.1.2 Core-level peaks	35
3.1.3 Auger process	36
3.1.4 Scienta ESCA-300 Spectrometer	36
3.1.5 Omicron SPHERA 125 Spectrometer	38
3.2 Infrared reflectance spectroscopy	38
3.2.1 Two-oscillator dielectric function	40
3.2.2 Factorised dielectric model	41
3.2.3 IR reflectivity simulation - transfer matrix formalism	41
3.2.4 Bruker Vertex 70v Fourier Transform IR Spectrometer	44
3.3 Hall effect	45
3.3.1 Van der Pauw geometry	46
3.3.2 Hall effect measurements - Ecopia HMS-300 System	47
3.4 Electrochemical capacitance-voltage measurements	48
3.4.1 Simulating Mott-Schottky Plots	50
3.4.2 ECV measurements - Dage Wafer Profiler CVP21	50
3.5 Secondary Ion Mass Spectrometry	51
3.5.1 SIMS measurements - ATOMICA SIMS 4500 Instrument	53
4 Surface, bulk and interface electronic properties of non-polar InN	55
4.1 Introduction	55
4.2 Experimental details	56
4.3 Results and discussion	57
4.4 Conclusions	65
5 Giant reduction of InN surface electron accumulation	67
5.1 Introduction	67
5.1.1 Si-doped InN - previous results	68
5.2 Experimental details	69

5.3	Transition from electron accumulation layer to hole depletion layer by Mg-doping	70
5.3.1	Results and analysis	70
5.3.2	Discussion	75
5.4	Conclusions	80
6	Sulfur passivation of highly Mg-doped InN	82
6.1	Introduction	82
6.2	Experimental details	84
6.3	Results and analysis	85
6.4	Discussion	88
6.5	Conclusions	94
7	Surface electronic properties of In-rich InGaN alloys grown by MOCVD	95
7.1	Introduction	95
7.2	Experimental details	96
7.3	Results and analysis	97
7.4	Discussion	107
7.5	Conclusions	109
8	General conclusions	110
A	Perturbation theory	115
A.1	Symmetry	115
A.2	$k \cdot p$ theory with no spin-orbit interaction	117
B	Optical phonon parameters for Al_2O_3	120
	Bibliography	120

Acknowledgments

Firstly, I would like to give my sincere thanks to my principal supervisor Prof. Chris McConville, who accepted me as his Ph.D. student, for his continued encouragement and invaluable suggestions during this work, for helping me in understanding of InN material. A special thanks goes to Dr. Tim Veal for his invaluable insights, suggestions and help. I really appreciate his willingness to meet me at every time when I needed, and going through several drafts of my thesis. I would also like to thank the surface science technician, Rob Johnston, without whom this research would not have been possible. Dr. Richard Morris is acknowledged for SIMS measurements.

I also wish to thank my colleagues from the office 422 Dr. Marc Walker, Dr. Phil King, Dr. Louise Bailey, Dr. Jim Aldous, Dr. Ajay Shukla, Dr. Mukul Misra, Sepehr Vasheghani Farahani, Nessa Fereshteh Saniee, Mo Saghir, Andrzej Stacel, Chris Burrows, James Mudd, Liam Fishwick, David Duncan for making the time I spent at the Warwick University enjoyable and amusing.

A big ‘Thank you!’ also goes out to my all colleagues from the RAINBOW project, Arantxa Vilalta-Clemente, Geeta Rani Mutta, Duc Van Dinh, Daria Skuridina, Tommaso Brazzini, Steven Albert, Öcal Tuna, Albert Minj, Saurabh Pandey, Piero Gamarra, Simon Kraeusel, Naresh Gunasekar, Rui Yang, Egidijus Sakalauskas, Nils Kaufmann, Francesco Ivaldi and Christian Rauch for a great time during project meetings and conferences. I hope we will be in touch.

And finally I would like to thank my best friends, Bartek vel Wysokie Czoło, Kamila vel Kamyk and Gosia vel Dudyn for all their support which has kept me going forward these last three long years and lastly, I would like to express an exceptional thank you to my family for everything.

Declarations

I declare that this thesis contains an account of my research work carried out at the Department of Physics, University of Warwick between February 2009 and February 2012 under the supervision of Prof. C. F. McConville. The research reported here has not been previously submitted, wholly or in part, at this or any other academic institution for admission to a higher degree.

The InN Mg implantation was performed at the Surrey Ion Beam Centre by Dr. N. H. Peng (University of Surrey, UK). The valence band spectrum for *c*-plane InN reported in Figure 4.2 was collected by Dr. Philip King (University of Warwick, UK). The SIMS profile presented in Figure 4.6 was performed by Dr. Gregor Koblmüller (University of California at Santa Barbara, USA). The SIMS profiles presented in Figure 5.2 were performed by Dr. Richard Morris (University of Warwick, UK). The density-functional theory calculations presented in this work were performed by Dr. Frank Fuchs, Dr. André Schleife, Prof. Dr. Friedhelm Bechstedt, and Dr. Jürgen Furthmüller (Friedrich-Schiller-Universität, Jena, Germany). All of the remaining data collection and calculations were performed by the author. The data analysis, simulation and interpretation was all performed by the author.

Wojciech Mieczyslaw Linhart

February 2012

Several articles based on this research have been published, are in press, or have been submitted for publication:

W. M. Linhart, T. D. Veal, P. D. C. King, G. Koblmüller, C. S. Gallinat, J. S. Speck and C. F. McConville, *Surface, bulk, and interface electronic properties of nonpolar InN*, Appl. Phys. Lett. **97**, 112103 (2010)

W. M. Linhart, Ö. Tuna, T. D. Veal, J. J. Mudd, C. Giesen, M. Heuken and C. F. McConville, *Surface electronic properties of In-rich InGaN alloys grown by MOCVD*, Phys. Stat. Sol. C **9**, 662 (2012)

W. M. Linhart J. H. Chai, R. J. H Morris, M. G. Dowsett, C. F. McConville, S. M. Durbin, and T. D. Veal, *Giant reduction of InN surface electron accumulation: Compensation of surface donors by Mg dopants*, submitted to Phys. Rev. Lett.

W. M. Linhart, T. D. Veal, J. H. Chai, S. M. Durbin, and C. F. McConville, *Sulfur passivation of high Mg-doped InN surface electron accumulation* (in preparation).

J. H. Chai, T. H. Myers, Y.-W. Song, R. J. Reeves, **W. M. Linhart**, R. J. Morris, T. D. Veal, M. G. Dowsett, C. F. McConville and S. M. Durbin, *MBE growth and characterization of Mn-doped InN*, J. Vac. Sci. Technol. **30**, 02B124 (2012)

Ö. Tuna, C. Giesen, G. P. Yablonskii, E. V. Lutsenko, N. Gunesekar, C. T. Coovan, **W. M. Linhart**, T. D. Veal, C. F. McConville, B. Holländer, H. Kalisch, A. Vescan, M. Heuken, *Structural, Electrical and Optical Characterization of MOCVD InGaN Layers with Various In Contents* (in preparation)

The work presented in this thesis has been presented at the following national and international conferences.

Electron accumulation and doping in III-V semiconductors (oral presentation),
4th Rainbow Workshop, September 2011, Bologna, Italy.

Giant reduction of InN surface electron accumulation: Compensation of surface donors by Mg dopants (oral presentation), 9th International Conference of Nitride Semiconductors (ICNS-9), July 2011, Glasgow, UK.

Electrochemical capacitance-voltage study of non-polar InN (poster presentation),
9th International Conference of Nitride Semiconductors (ICNS-9), July 2011, Glasgow, UK.

Dramatic reduction of InN electron accumulation by high Mg-doping (oral presentation), European Materials Research Society (E-MRS) - Spring Meeting, May 2011, Nice, France.

"Unpinned" surface Fermi level in Mg-doped InN? (poster presentation), 18th International Conference of Surface Science (ISSC-18), April 2011, University of Warwick, UK.

Electronic properties of Mg-doped InN grown on yttria stabilized zirconia (oral presentation), International Workshop on Nitride Semiconductors (IWN2010), September 2010, Tampa, Florida, USA.

Surface, bulk and interface electronic properties of non-polar InN (oral presentation), International Workshop on Nitride Semiconductors (IWN2010), September 2010, Tampa, Florida, USA.

Can indium nitride surfaces be chemically and electronically passivated? (oral presentation), International Workshop on Nitride Semiconductors (IWN2010), September 2010, Tampa, Florida, USA.

Electronic properties of non-polar InN and Mg-doped In (oral presentation), 2nd RAINBOW Workshop, August 2010, Madrid, Spain.

Surface, bulk and interface electronic properties of non-polar InN (oral presentation), United Kingdom Nitrides Consortium (UKNC), July 2010, University of Sheffield, UK.

Electronic and optical study of m-plane and a-plane InN grown on free-standing GaN substrates (oral presentation), European Materials Research Society (E-MRS) - Spring Meeting, June 2010, Strasbourg, France.

Electrical and optical properties of Mg-doped InN (poster presentation), United Kingdom Nitrides Consortium (UKNC), January 2010, Tyndall National Institute, University of College Cork, Ireland.

Electrical and optical properties of Mg-doped InN (poster presentation), European Materials Research Society (E-MRS) - Fall Meeting, September 2009, Warsaw, Poland.

Abstract

InN and group III nitride materials have attracted great interest due to their potential applications for optoelectronic devices, as the range of band gaps cover the ultra-violet to the near infrared. InN and all In-rich $\text{In}_x\text{Ga}_{1-x}\text{N}$ alloys exhibit a surface electron accumulation layer. This is due to the unusually low conduction band minimum (CBM) at the Brouillon zone centre (Γ -point) with respect to the charge-neutrality level. Electron accumulation has been observed at the surface of almost all *n*-type and *p*-type InN, making proof of *p*-type doping of this material very difficult. Routine characterization of *p*-type conductivity of Mg-doped samples using single-field Hall effect is prevented by the presence of a surface inversion space-charge layer, and hence the surface electron-rich region dominates the measurements. In this thesis, the results of investigations on non-polar InN surfaces, Mg-doped InN surfaces and a range of $\text{In}_x\text{Ga}_{1-x}\text{N}$ alloys across the composition entire range are presented.

Considerable improvement of the quality of *a*- and *m*-plane InN thin films has been achieved using free standing GaN substrates in conjunction with a GaN buffer layer and grown by PAMBE. Using a combination of infrared reflectivity (FTIR), x-ray photoemission spectroscopy (XPS) and electrochemical capacitance voltage (ECV) measurements, the surface space charge properties of these samples have been investigated. The surface Fermi level has been determined to be lower than previously observed on non-cleaved InN samples. Additionally a high carrier concentration has been found on the non-polar InN, close to the interface with the GaN buffer layer, associated with unintentionally incorporated oxygen impurities. The increased concentration of oxygen impurities near the InN/GaN interface, confirmed by secondary ion mass spectrometry (SIMS), is due to the relatively low growth temperature (380 - 450 °C) used to produce the non-polar InN films.

XPS has been also used in the investigations of Mg-doped InN. A significant lowering of the surface Fermi level has been observed with increasing Mg-doping for the highest Mg concentration ($> 1 \times 10^{19} \text{ cm}^{-3}$) indicating a highly desirable reduction in the degree of surface electron accumulation. While for moderate Mg concentrations the surface Fermi level is at the previously determined ‘universal’ value of ~ 1.4 eV above the valence band maximum, for $[\text{Mg}] = 1.2 \times 10^{20} \text{ cm}^{-3}$, a value of 0.83 eV is found. As a consequence, for $[\text{Mg}] > 1 \times 10^{19} \text{ cm}^{-3}$ the donor surface state density increases while the surface electron density decreases enormously, resulting in a transition from electron accumulation to almost just hole depletion layer. This reduction of electron accumulation in high Mg-doped InN can be improved by additional surface treatment, therefore results of a series of sulfur treated Mg-doped InN sample are also reported in this thesis.

Finally, the electronic properties of $\text{In}_x\text{Ga}_{1-x}\text{N}$ alloys with a composition range of $0.20 \geq x \geq 1.00$ have been investigated, using XPS and FTIR. The transition from electron accumulation to electron depletion has been observed at a composition of $x \approx 0.20$, while for $x \geq 0.20$ an increasing electron accumulation with decreasing Ga fraction has been observed.

Abbreviations and common symbols

ADM	Amphoteric defect model
AFM	Atomic force microscopy
ARPES	Angle-resolved photoemission spectroscopy
CB	Conduction band
CBM	Conduction band minimum
CNL	Charge neutrality level
DFT	Density-functional theory
DOS	Density of states
ECV	Electrochemical capacitance-voltage
FTIR	Fourier-transform infrared
FWHM	Full width at half maximum
IMFP	Inelastic mean free path
IR	Infrared
LDA	Local density approximation
MCT	mercury cadmium telluride
MOCVD	Metal-organic chemical vapor deposition
MTFA	Modified Thomas-Fermi approximation
NCESS	National Centre for Electron Spectroscopy and Surface Analysis
PAMBE	Plasma-assisted molecular beam epitaxy
PL	Photoluminescence
QPC	Quasiparticle-corrected
SIMS	Secondary ion mass spectrometry
STS	Scanning tunneling spectroscopy
TMM	Transfer matrix method
UHV	Ultra-high vacuum
UV	Ultraviolet
VB	Valence band

VBM	Valence band maximum
ViGS	Virtual gap states
XPS	X-ray photoemission spectroscopy
<i>fcc</i>	Face centered cubic
<i>wz</i>	Wurtzite
<i>zb</i>	Zinc-blende
a	Lattice constant
B	Magnetic field
C	Capacitance
c	Lattice constant
<i>c</i>	Speed of light ($2.988 \times 10^8 \text{ m/s}$)
Δ_{cr}	Crystal field splitting
ΔR	Reduction of surface electron accumulation
Δ_{so}	Spin-orbit splitting
δ	Kronecker delta function
E	Electric field
<i>E</i>	Energy
<i>E_B</i>	Binding energy
<i>E_F</i>	Fermi level
<i>E_f</i>	Final state energy
<i>E_g</i>	Band gap
<i>E_i</i>	Initial state energy
<i>E_k</i>	Kinetic energy
<i>E_{mid}</i>	Mid-gap energy
<i>e</i>	Electronic charge ($1.602 \times 10^{-19} \text{ C}$)
eV	Electron volts ($1.602 \times 10^{-19} \text{ J}$)
ε_0	Permittivity of vacuum ($8.854 \times 10^{-12} \text{ Fm}^{-1}$)
$\varepsilon(0)$	Static dielectric constant
$\varepsilon(\infty)$	High-frequency dielectric constant
<i>f_{FD}</i>	Fermi-Dirac distribution function

G	Reciprocal lattice vector
<i>g</i>	Density of states
Γ	Centre of Brillouin zone
γ_{LO}	Longitudinal optical phonon damping parameter
γ_{TO}	Transverse optical phonon damping parameter
<i>H</i>	Hamiltonian
<i>h</i>	Planck's constant (6.626×10^{-34} Js)
\hbar	$h/2\pi$ (1.55×10^{-34} Js)
k	Wavevector
λ	inelastic mean free path
m_e	Free electron mass (9.109×10^{-31} kg)
m^*	Effective mass
N_A^-	Ionized acceptor density
N_D^+	Ionized donor density
<i>n</i>	Carrier density (electrons)
n_{2D}	Electron sheet density
n_{SS}	Surface state density
ω_P	Plasma frequency
ω_{LO}	Longitudinal optical phonon frequency
ω_{TO}	Transverse optical phonon frequency
ψ	Wavefunction
ϕ	Work function
<i>P</i>	Kane's matric element
<i>p</i>	Carrier density (holes)
p	Momentum operator ($-i\hbar\nabla$)
R, r	Position vectors
T	Primitive translation vector
τ	Plasmon lifetime
θ	Take off/Emission angle
<i>V</i>	Potential

V_{bb} Band bending

ν frequency

μ Mobility

List of Figures

1.1	Band gaps of the $\text{In}_x\text{Ga}_{1-x}\text{N}$ and $\text{In}_x\text{Al}_{1-x}\text{N}$ alloy systems, showing the close match to the solar spectrum.	2
1.2	Schematic illustration of InN wurtzite and zinc-blende crystal structure.	3
1.3	Ball and stick model illustrating the In-polar and N-polar directions of wurtzite InN.	4
1.4	Valence band photoemission spectra of In-polar InN, N-polar InN and mixed-polarity InN.	5
1.5	Schematic illustration of (a) <i>a</i> -plane ($11\bar{2}0$) and (b) <i>m</i> -plane ($1\bar{1}00$) InN.	5
1.6	Schematic illustration of the <i>a</i> -plane, <i>m</i> -plane and <i>c</i> -plane in wurtzite InN.	6
1.7	Schematic illustration of the Burstein-Moss effect in InN.	7
1.8	QPC-DFT band structure calculations for wurtzite InN and corresponding Brillouin zone.	8
1.9	QPC-DFT band structure calculations for zinc-blende InN and corresponding Brillouin zone.	8
1.10	The band gap of $\text{In}_x\text{Ga}_{1-x}\text{N}$ (red), $\text{In}_x\text{Al}_{1-x}\text{N}$ (blue) and $\text{Al}_x\text{Ga}_{1-x}\text{N}$ (green) plotted as a function of lattice constant <i>a</i>	9
1.11	Photoluminescence and absorption spectra for InN and $\text{In}_x\text{Ga}_{1-x}\text{N}$ alloys with different composition.	10
1.12	Schematic band structure of a linear lattice within the nearly free electron model.	11
1.13	The conduction band minimum (CBM) and the valence band maximum (VBM) with respect to the charge neutrality level for AlN, GaN, InN, InAs and GaAs, and showing the respective valence band offsets.	12
1.14	ARPES photocurrent intensity map of the parallel dispersion in the surface plane of two subbands in InN(0001) at 60 K.	14

1.15 Calculated formation energies for Si_{In} , O_{N} , V_{N} and Mg_{In} as a function of the Fermi level with respect to the VBM for zinc-blende InN under In-rich conditions.	16
2.1 A comparison of the conduction band dispersion relations calculated using different approximations for InN.	24
2.2 A comparison of the conduction band dispersion relations calculated from different approximations for InN.	26
2.3 A schematic representation of the band bending and associated charge profiles for inversion, depletion, accumulation space charge layers at the surface.	29
3.1 Schematic representation of X-ray photoemission spectroscopy with the core-level and valence photoelectron emission processes.	32
3.2 XPS wide energy scan from an InN(0001) surface.	34
3.3 Illustration of a KLM Auger process.	36
3.4 Schematic of the FTIR spectrometer showing the Michelson interferometer and an example of reflectivity measurements.	39
3.5 Schematic multilayer structure composed of N layers and N+1 interfaces.	42
3.6 Schematic block diagram of method used when simulating IR spectra. .	44
3.7 Schematic view of Hall effect measurements.	46
3.8 Schematic showing the van der Pauw geometry for Hall sampling. .	47
3.9 Schematic measurement setup of ECV.	49
3.10 Schematic representation of the sputtering process during SIMS measurements.	52
3.11 Front view of the ATOMICA 4500 system.	53
4.1 Experimental infrared reflectivity spectra for non-polar InN plotted with the simulated spectra.	59
4.2 Valence band X-ray photoemission of the non-polar <i>a</i> - and <i>m</i> -plane InN and <i>c</i> -plane InN grown under In-rich conditions.	60

4.3	In 3d, N 1s, and O 1s core-level spectra recorded using an emission angle of 90° from an untreated and a cleaned <i>a</i> -plane InN film.	61
4.4	XPS In:N intensity ratios calculated for the surface of <i>a</i> -plane InN for different surface indium coverages.	62
4.5	The position of the conduction band minimum (CBM) and valence band maximum (VBM) with respect to the Fermi level, E_F , and carrier concentration as a function of depth from the surface for <i>m</i> -plane In-rich InN, <i>a</i> -plane In-rich and N-rich InN and <i>c</i> -plane In-rich InN.	63
4.6	Electrolyte capacitance-voltage measurements and simulations on non-polar InN films.	64
4.7	SIMS data for <i>m</i> -plane InN, indicating the presence of oxygen impurity in the bulk.	65
4.8	Schematic representation of the three-region model.	66
5.1	Schematic representation of the decrease in downward band bending, corresponding reduction in unoccupied surface state density as the Fermi level moves closer to the CNL at the surface, and stabilization of the bulk and surface Fermi levels at the CNL with increasing doping in InN.	69
5.2	XPS wide energy scan from heavily doped Mg-doped InN.	70
5.3	Mg SIMS profiles of four InN:Mg films.	71
5.4	Valence band photoemission spectra of Mg-doped InN for different Mg concentrations.	72
5.5	The surface Fermi level position and In:N XPS ratio as a functions of Mg concentration.	73
5.6	The conduction band minimum, valence band maximum and charge neutrality level with respect to the Fermi level and a carrier concentration profile, as a function of depth from the surface.	74
5.7	Surface electron sheet density and donor surface state density as a function of Mg concentration.	75

5.8	Density of states for the polar InN (0001) and surface state density evaluated by numerically solving Poisson's equation within MTFA.	77
5.9	Comparison of the electron mobility measured by the Hall effect for Mg-doped InN.	78
5.10	Electrolyte capacitance-voltage measurements on Mg-doped InN films. .	79
5.11	Surface Fermi level position of <i>n</i> -type and <i>p</i> -type InN(0001) as a function of carrier concentration.	80
6.1	Valence band photoemission spectra of untreated and S-treated <i>c</i> -plane InN, and the carrier concentration as a function of depth.	83
6.2	XPS wide energy scan from heavily doped Mg-doped InN.	84
6.3	Valence band photoemission spectra of untreated and S-treated Mg-doped InN for different Mg concentrations.	86
6.4	Position of the surface Fermi level with respect to the VBM as a function of Mg concentration for untreated (filled circles) and (NH ₄) ₂ S _x -treated (open circles) Mg-doped InN samples.	87
6.5	XPS spectrum of the Cl 2p peak for HCl etched Mg-doped InN sample. .	88
6.6	Core level XPS spectra of the In 3d _{5/2} level for untreated and (NH ₄) ₂ S _x treatment Mg-doped InN with different Mg concentrations.	89
6.7	Core level XPS spectra of the N 1s level for untreated and (NH ₄) ₂ S _x treatment Mg-doped InN with different Mg concentrations.	89
6.8	Core level XPS spectrum of S 2p for (NH ₄) ₂ S _x treated Mg-doped. .	91
6.9	CBM, VBM and CNL positions with respect to the Fermi level and the corresponding carrier concentration profile, as a function of depth before and after S treatment of Mg-doped InN.	92
6.10	Surface state density evaluated by numerically solving Poisson's equation within MTFA and bulk DOS for the (0001) InN calculated by F. Bechstedt's group	93
7.1	XPS wide energy scan from In _x Ga _{1-x} N.	97

7.2 In 3d, Ga 2p _{3/2} , N 1s, and O 1s core-level spectra recorded using an emission angle of 90° from an untreated and a cleaned In _{0.62} Ga _{0.38} N film.	99
7.3 Valence band photoemission spectra with respect to the Fermi level (E_F) of In _x Ga _{1-x} N alloys across the composition range.	100
7.4 The experimental infrared reflectivity spectra for GaN and InN/GaN shown along with the simulated spectra.	102
7.5 The experimental infrared reflectivity spectra for InN, In _{0.82} Ga _{0.18} N, In _{0.75} Ga _{0.25} N and In _{0.62} Ga _{0.38} N shown along with the simulated spectra.	103
7.6 The experimental infrared reflectivity spectra for In _{0.54} Ga _{0.46} N, In _{0.40} Ga _{0.60} N and In _{0.20} Ga _{0.80} N with the simulated spectra.	104
7.7 Carrier concentration and band bending as a function of depth for InN, and In _x Ga _{1-x} N alloys.	105
7.8 Mott-Schottky plot of capacitance-voltage data obtained from In _x Ga _{1-x} N films	106
7.9 Variation of band gap and barrier height Φ_B at In _x Ga _{1-x} N surfaces with varying In concentration (x).	108
7.10 The CBM, VBM, and mid-gap position (E_{mid}) as a function of In _x Ga _{1-x} N composition shown with respect to the charge neutrality level (CNL).	109
8.1 Surface Fermi level position of <i>n</i> -type (squares) and <i>p</i> -type (circles) InN as a function of carrier concentration.	112
8.2 Surface state density evaluated by numerically solving Poisson's equation within MTFA and bulk DOS for the InN(0001) (calculated by F. Bechstedt's group)	113
A.1 A schematic representation of <i>s</i> - and <i>p</i> -orbitals.	116
A.2 A schematic representation of $\mathbf{k} \cdot \mathbf{p}$ band structure around $\mathbf{k}=0$ for the semiconductor with a direct band gap without spin-orbit coupling.	118
A.3 A schematic representation of $\mathbf{k} \cdot \mathbf{p}$ band structure around $\mathbf{k}=0$ for the semiconductor with a direct band gap with spin-orbit coupling.	119

Chapter 1

Introduction

1.1 Why group-III nitride semiconductors?

Indium nitride (InN) is a narrow band gap III-V semiconductor and along with its related alloys (particularly $\text{In}_x\text{Ga}_{1-x}\text{N}$ and $\text{In}_x\text{Al}_{1-x}\text{N}$) represents a very important class of materials for the future development and mass production of electronic and opto-electronic devices. Excellent predicted transport properties such as a high electron mobility [1, 2], and large electron velocity [3] without doubt make InN and its alloys attractive materials for the production of high electron mobility transistors operating at high frequencies up to the several THz range. Additionally, InN together with $\text{In}_x\text{Ga}_{1-x}\text{N}$ (and $\text{In}_x\text{Al}_{1-x}\text{N}$) show significant promise for use in inorganic solar cell fabrication, due to the expansion of the possible operational spectral range from the ultraviolet to the near infrared (Figure 1.1) offered by the band gap range from InN (~ 0.65 eV) through GaN (~ 3.44 eV) to AlN (~ 6.25 eV) [4–6]. Investigations performed in the last decade suggest that two or more $\text{In}_x\text{Ga}_{1-x}\text{N}$ tandem structures with different In:Ga ratios may well produce a significant increases in the energy conversion efficiency of the basic solar cell design to over 50% [7–10]. Moreover, III-nitride materials and their production are less toxic and more abundant than the currently used materials such as GaInP/GaInAs [11–13].

Presently, only GaN and Ga-rich $\text{In}_x\text{Ga}_{1-x}\text{N}$ thin films are used in blue and ultraviolet nitride-based light-emitting diodes (LEDs) and laser structures that are, for example, used for in Blu-ray disc systems [18,19]. In 2009, the first stable $\text{In}_x\text{Ga}_{1-x}\text{N}$ green laser diode was produced by researchers at Nichia Corporation [20,21], making a huge step forward for the production of full colour laser displays. Furthermore, advanced GaN/ $\text{Al}_x\text{Ga}_{1-x}\text{N}$ high power microwave transistors are now commercially available [22] and are being applied to low noise amplifiers and RF power control [23].

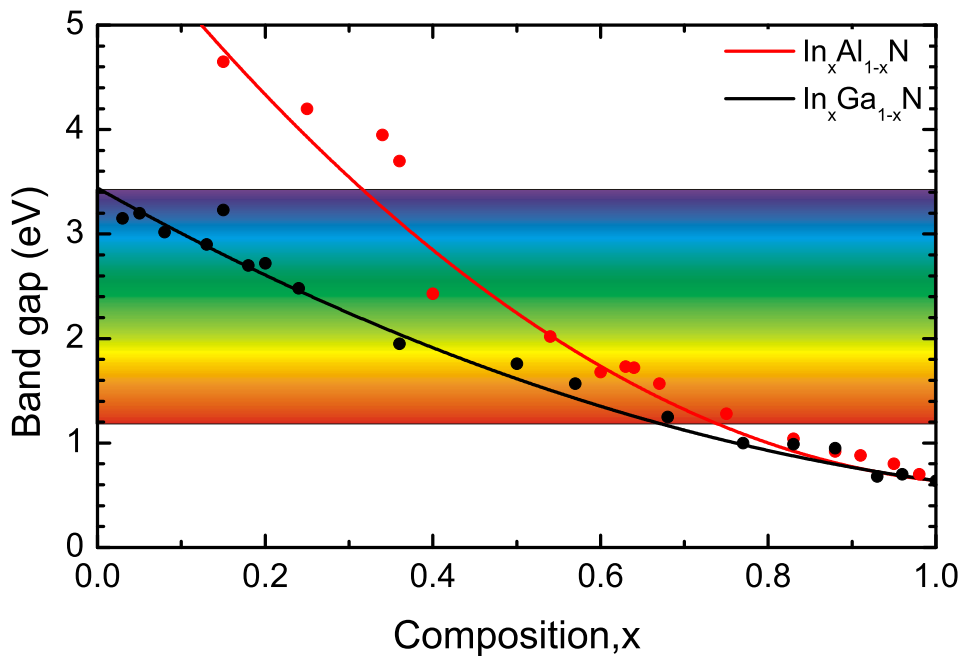


Figure 1.1: Band gaps of the $\text{In}_x\text{Ga}_{1-x}\text{N}$ and $\text{In}_x\text{Al}_{1-x}\text{N}$ alloy systems, showing their good matching to the solar spectrum. The dots represent the experimental values, taken from [14–17]. The solid lines are bowing curves with best-fit bowing parameters.

In spite of the above mentioned positive aspects, the development of device applications based on InN and In-rich alloys has proved to be much more problematic. The large lattice mismatch between the epilayer and any substrate material results in a high density of dislocations in the material and consequently in significantly enhanced carrier scattering [24, 25]. As-grown materials very often exhibit a very high concentration of residual donors, typically $10^{18} – 10^{21} \text{ cm}^{-3}$. Moreover, an electron accumulation layer exists at the surface of both *n*-type and *p*-type InN and In-rich $\text{In}_x\text{Ga}_{1-x}\text{N}$ alloys [26–28], indicating serious difficulties in the production of a *p-n* junction. However, this electron accumulation could potentially be exploited for gas sensor applications and for the next generation of THz radiation generators and sensors [29–32].

1.2 Crystal structure

Group III-nitride semiconductors can crystalize in two different stable crystalline polymorphs either as wurtzite or zinc-blende (cubic) structures. In both of these crystal structures each In atom is tetrahedrally bounded to four N atoms (and vice

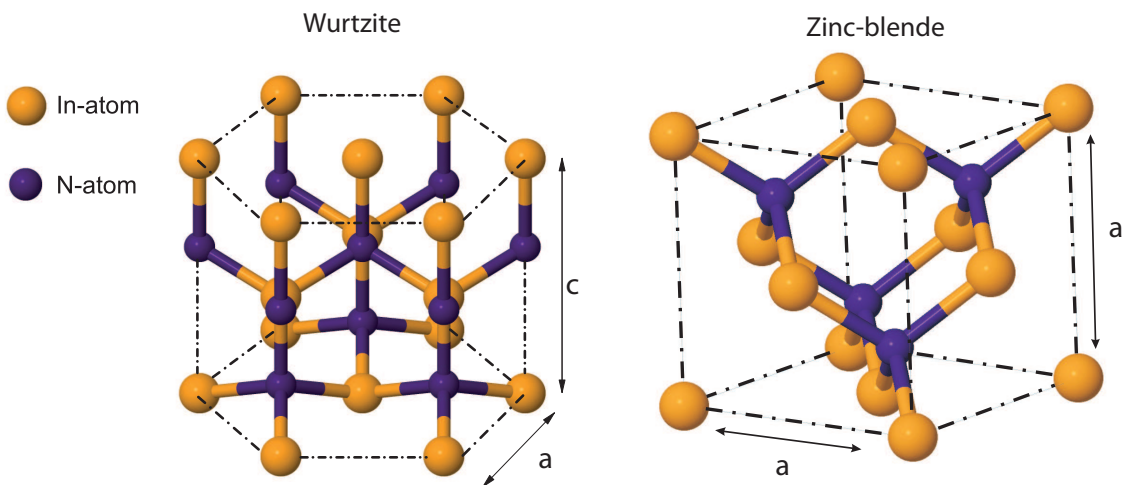


Figure 1.2: Schematic illustration of InN wurtzite and zinc-blende crystal structure. The small (blue) and large (yellow) spheres indicate N and In, respectively.

Table 1.1: Basic details about crystal structures of InN

Category	Crystal structure	
	Wurtzite	Zinc-blende
Group of symmetry	$C^46\nu - P6_{3mc}$	$T_d - F_{\bar{4}3m}$
lattice parameters [36]	$a = 3.54\text{\AA}$ $c = 5.70\text{\AA}$	$a = 4.98\text{\AA}$

versa). The wurtzite and zinc-blende structures of InN are shown in Figure 1.2, as an example for InN. Details relating to the group symmetry and lattice parameters of InN structures are presented in Table 1.1. Wurtzite InN (*wz*-InN) and zinc-blende InN (*zb*-InN) have slightly different electronic and optical properties, however, a very narrow fundamental band gap and the universality of electron accumulation at the surface is common for both polymorphs [33–35].

For a wurtzite structure the $[0001]$ and $[000\bar{1}]$ directions are distinguishable, while for zinc-blende structure the $[001]$ and $[00\bar{1}]$ directions are equivalent. In *wz*-InN the directions along *c*-axis determine the type of crystal polarity. The In-polarity is defined by the crystal orientation $[0001]$ where only single bonds from the In atoms are oriented toward the surface. The opposite orientation $[000\bar{1}]$ (away from the surface), where three bonds from the In atoms are directed toward the N atoms, determines the N-polarity [37]. An important point to note is that in both cases (irrespective of surface polarity) the surfaces of InN are always terminated by

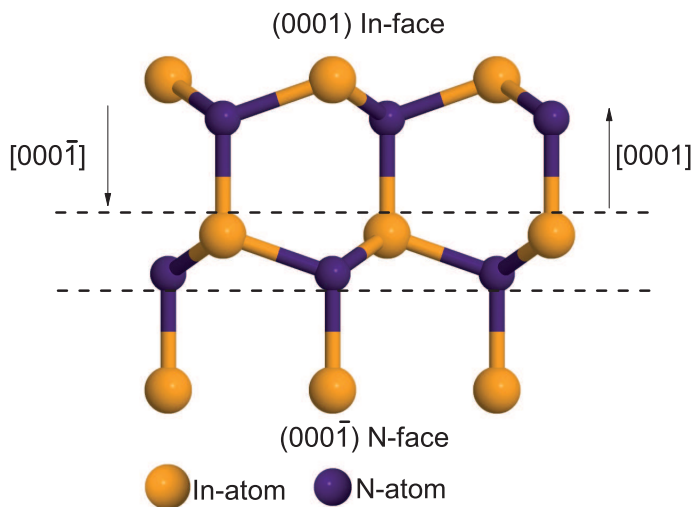


Figure 1.3: Ball and stick model illustrating the In-polar $[0001]$ and N-polar $[000\bar{1}]$ directions of wurtzite InN. The small and large spheres indicate N and In, respectively. The arrows show the directions perpendicular to the proper faces.

In atoms. Hence the polarity along the c -axis is defined by the direction of In-N bonds. The In- and N-polarity of *wz*-InN are schematically illustrated in Figure 1.3, however this figure is not meant to represent a surface formation caused by three dangling bonds in In-adlayer. The polarity of InN can be determined by valence band spectrum observed in X-ray photoemission spectroscopy (XPS). Veal *et al.* [38] reported that for In-polar InN the valence band peak at ~ 3 eV is more intense than the one at ~ 6.5 eV, while the N-polar films exhibit more intense the valence band peak at ~ 6.5 eV than at the ~ 3 eV peak. In the case of mixed polarity InN films, the valence band peak intensities lie between those of the In- and N-polarity samples (Figure 1.4). These results have shown that the valence band spectrum reflects the polarity dependence of the surface termination.

Besides the polar directions $[0001]$ and $[000\bar{1}]$ in wurtzite structure it is possible to distinguish the other ones, where the surface is terminated together by In and N atoms, defining non-polar or semi-polar faces. The $[11\bar{2}0]$ and $[1\bar{1}00]$ directions are perpendicular the non-polar faces, these are the a -plane ($(11\bar{2}0)$) and m -plane ($(1\bar{1}00)$) respectively. The non-polar faces are schematically shown in Figures 1.5 and 1.6.

The zinc-blende InN lattice has high symmetry due to its face centered cubic

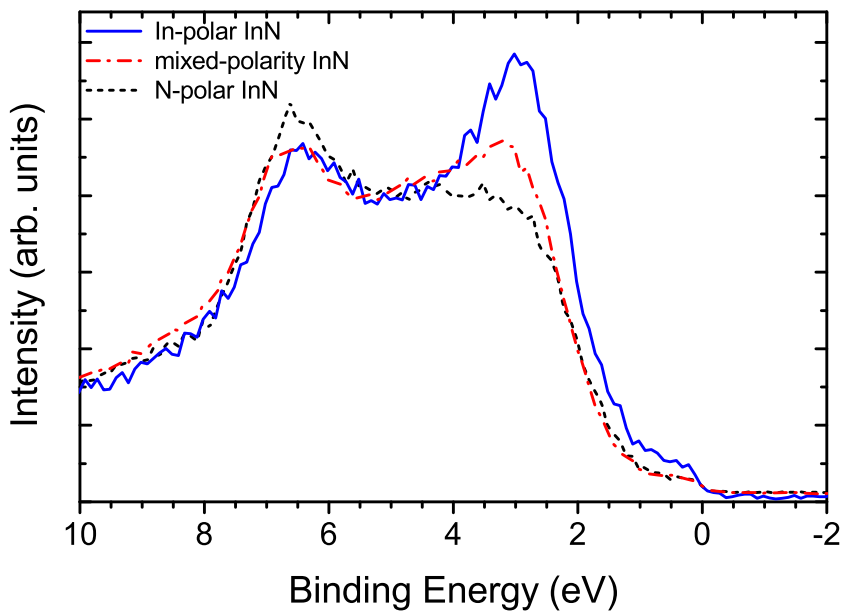


Figure 1.4: Valence band photoemission spectra of In-polar InN, N-polar InN and mixed-polarity InN, taken from [38].

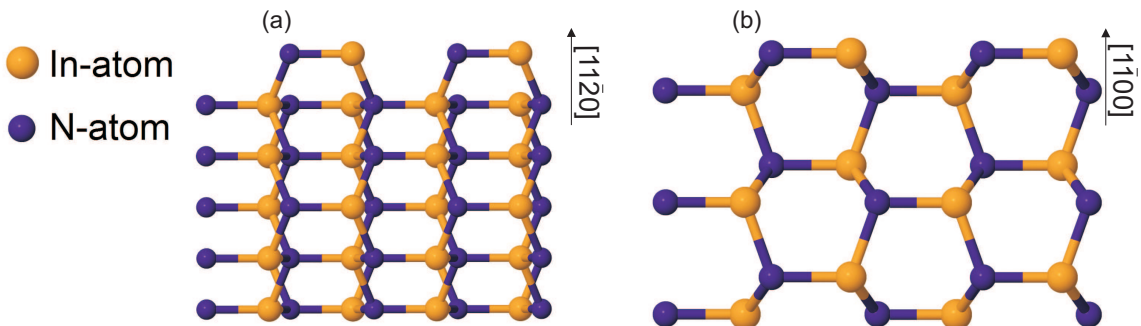


Figure 1.5: Schematic illustration of (a) a-plane ($11\bar{2}0$) and (b) m-plane ($1\bar{1}00$) InN. The small and large spheres indicate N and In, respectively. The arrows show the directions perpendicular to the proper planes

(fcc) structure with two atoms (In and N) basis and has a well defined centre of symmetry. This is reflected in its electronic and optical properties such as a lack of piezoelectricity, and an insensitivity to the polarization of light. As a result, cubic crystals such as *zb*-InN do not normally show any optical anisotropy. However, wurtzite InN crystals have completely different symmetry than the cubic one. The wurtzite unit cell has a hexagonal base, the normal to which defines a unique c-axis. This lattice arrangement introduces an anisotropy between directions parallel and perpendicular to the c-axis, therefore only the c-axis does not exhibit optical anisotropy, because incident light can only be polarized with $\mathbf{E} \perp c$. However, for

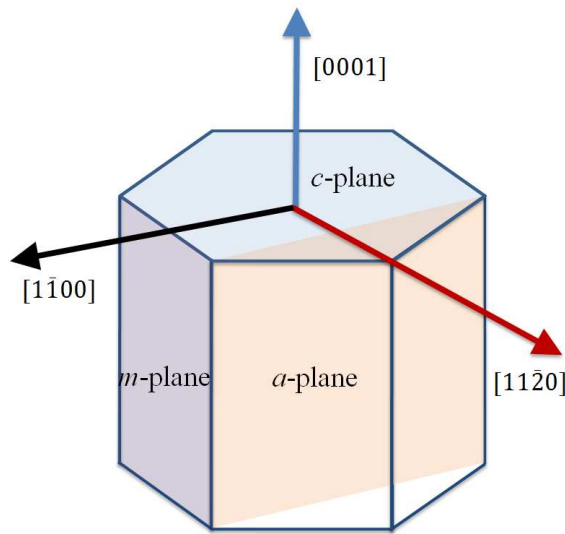


Figure 1.6: Schematic illustration of a -plane, m -plane and c -plane in wurtzite InN. The arrows show the directions perpendicular to the proper planes.

other directions, for example for non-polar InN, the light can be polarized with $\mathbf{E} \perp c$ as well as $\mathbf{E} \parallel c$, indicating optical anisotropy [39–41]. Additionally, due to a presence of the unique c -axis wurtzite InN can exhibit piezoelectric effect [42–44].

1.3 Band gap and energy band structure

One of the most important parameters for a semiconductor is the magnitude of their energy band gap. Early optical investigations of InN indicated that the fundamental band gap of this material was in the range 1.7–3.1 eV [45–49]. However, at that time the material was typically sputter-grown leading to inhomogeneous and polycrystalline films with very high defect and electron densities ($1 \times 10^{19} – 6 \times 10^{20} \text{ cm}^{-3}$) and this led to the wrong determination of the band gap. The high electron density indicates that the Fermi level, E_F , is displaced deep into the conduction band. For degenerate semiconductors, optical absorption is forbidden for transitions below the Fermi level and hence the optical absorption measurements overestimate the fundamental band gap, leading to a phenomenon known as the Burstein-Moss effect (Figure 1.7) [50]. In 1986 Tansley and Foley reported the fundamental band gap of InN to be 1.89 eV with, a low carrier concentration of $1.6 \times 10^{16} \text{ cm}^{-3}$, but these results have never been reproduced [49]. More recently, the growth techniques

for InN are much improved, especially by plasma-assisted molecular beam epitaxy (PAMBE), resulting in high quality InN films. In addition a much better understanding of the Burstein-Moss effect has led to a much lower value of InN band gap of ~ 0.7 eV [4, 14, 51–53]. In this thesis, a room temperature band gap of 0.64 eV is employed, obtained from Varshni parameters derived by Wu *et al.* [53].

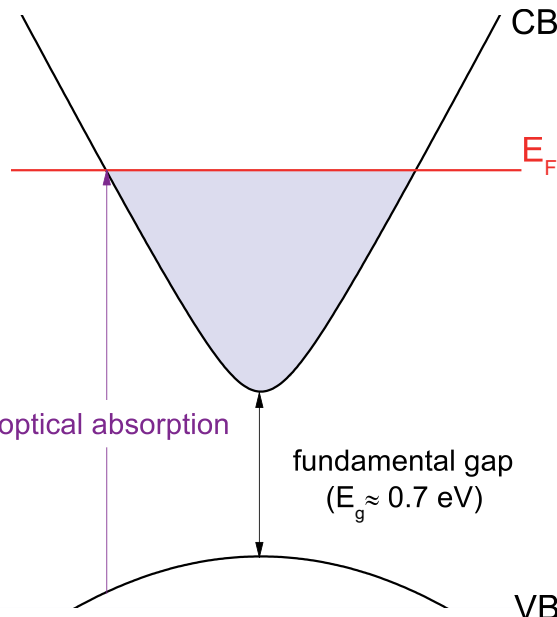


Figure 1.7: Schematic illustration of the Burstein-Moss effect in InN. A non-parabolic conduction band (CB) dispersion has been calculated using the Kane model (see Chapter 2). Note the Fermi level is pinned above the conduction band minimum.

The narrow band gap in InN is due to the electron configuration of In ($1s^2 2s^2 2p^6 3s^2 3p^6 4d^{10} 5s^2 5p^1$) and N ($1s^2 2s^2 2p^3$) and the interactions between the orbitals. This electron configuration results in sp^3 hybridization, providing the tetrahedrally bonded configuration of In and N atoms in both wurtzite and cubic crystals. The narrow InN band gap is mainly caused by p - d repulsion, between N 2p-valence states and shallow In 4d core states, which pushes the valence band maximum to higher energies [54]. Additionally, the large difference in both ionic size and the higher electronegativity of nitrogen lowers the energy of the N 2s orbital and as a result reduces the separation between In 4d and N 2p orbitals, increasing the p - d repulsion effect. This p - d repulsion effect also occurs in GaN, where the band gap is ~ 3.44 eV [55]. However, this repulsion is much smaller than for InN due to the large Ga 3d and N 2p orbital separation.

The calculated band structures within a quasiparticle-corrected density-functional theory (QPC-DFT) of *wz*-InN and *zb*-InN [56,57] with corresponding Brillouin zones are shown in Figures 1.8 and 1.9 respectively. The valence electrons in InN form four doubly spin degenerate valence bands, where three bands have *p*-orbital character and one has *s*-orbital character. The spin-orbit and crystal field interactions in non-isotropic *wz*-InN split the *p*-orbital character bands at the Γ -point into two lower and one upper bands. The conduction band at the Γ -point is highly non-parabolic, therefore the two-band $\mathbf{k} \cdot \mathbf{p}$ approximation outlined in Section 2.1.2

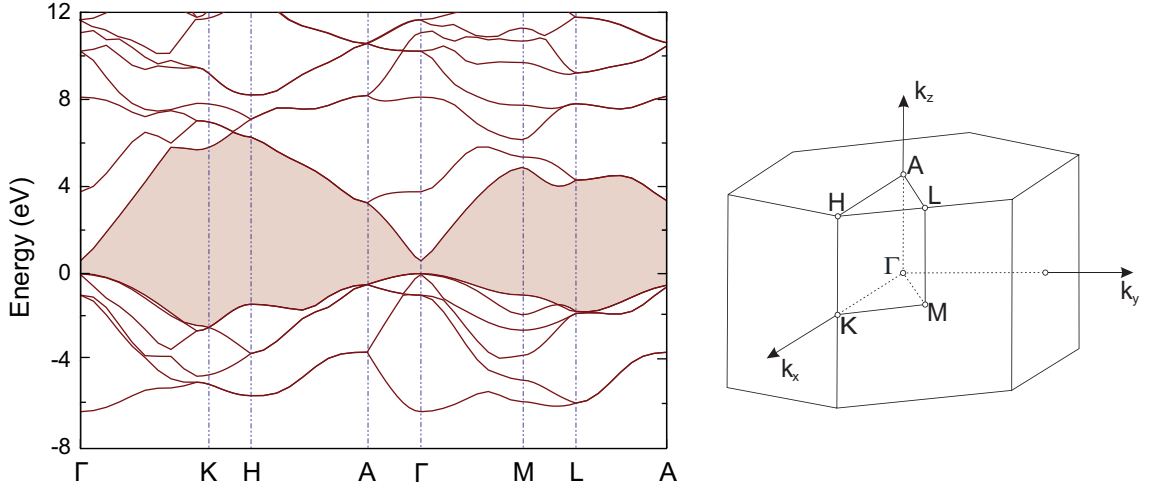


Figure 1.8: QPC-DFT band structure calculations for wurtzite InN and corresponding Brillouin zone [56, 57]. The fundamental energy gap across the Brillouin zone is represented by the shaded area.

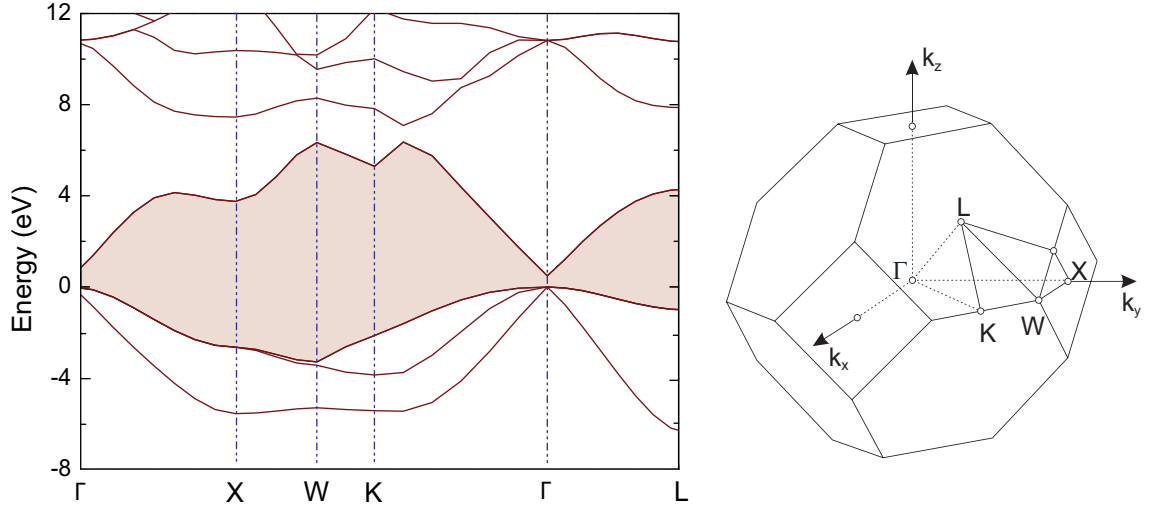


Figure 1.9: QPC-DFT band structure calculations for zinc-blende InN and corresponding Brillouin zone [56, 57]. The fundamental energy gap across the Brillouin zone is represented by the shaded area.

is used in the calculations presented in this thesis. The electronic band structure for *zb*-InN is also a little simpler than that for the *wz*-InN due to the lack of crystal field splitting.

The band gap of $\text{In}_x\text{Ga}_{1-x}\text{N}$ alloys is strictly dependent on the composition x of the material(see Figure 1.1), and the value always lies between the band gap values of InN and GaN and changes non-linearly with the composition. This is usually expressed by the conventional equation

$$E_g^{\text{In}_x\text{Ga}_{1-x}\text{N}} = (1 - x)E_g^{\text{GaN}} + xE_g^{\text{InN}} - bx(1 - x), \quad (1.1)$$

where b is the bowing parameter of 1.7 eV [58]. Whether the single bowing parameter can describe the band gap over the entire composition range is still controversial [14, 59, 60]. However, one should note that the band gap of $\text{In}_x\text{Ga}_{1-x}\text{N}$ alloys also depends on its lattice constant, which suggests that alloying atom size plays a very important role in determining the band gaps. Figure 1.10 shows the band gap of $\text{In}_x\text{Ga}_{1-x}\text{N}$, $\text{In}_x\text{Al}_{1-x}\text{N}$ and $\text{Al}_x\text{Ga}_{1-x}\text{N}$ as a function of lattice constant a .

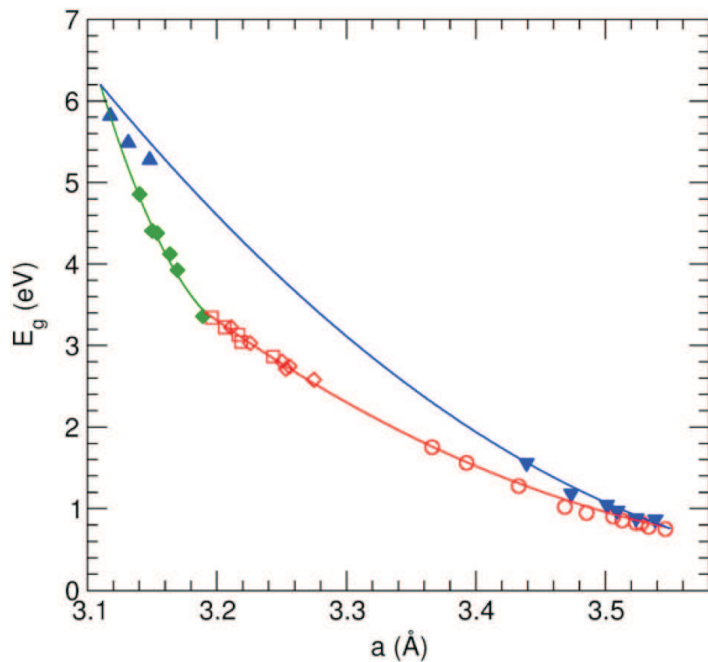


Figure 1.10: The band gap of $\text{In}_x\text{Ga}_{1-x}\text{N}$, $\text{In}_x\text{Al}_{1-x}\text{N}$ and $\text{Al}_x\text{Ga}_{1-x}\text{N}$ plotted as a function of lattice constant a adapted from [6]. Lines are fits to the standard bowing parameter equation.

The absorption and photoluminescence spectra of InN and $\text{In}_x\text{Ga}_{1-x}\text{N}$ alloys

over a wide range of compositions are presented in Figure 1.11, showing a blue shift from the InN band gap with increasing Ga content and demonstrating that the $In_xGa_{1-x}N$ alloy system covers a wide spectral region from the near infrared to the ultraviolet [6]. The absorption edge and the PL emission peaks are in excellent correspondence, indicating that the direct gap of $In_xGa_{1-x}N$ was being measured.

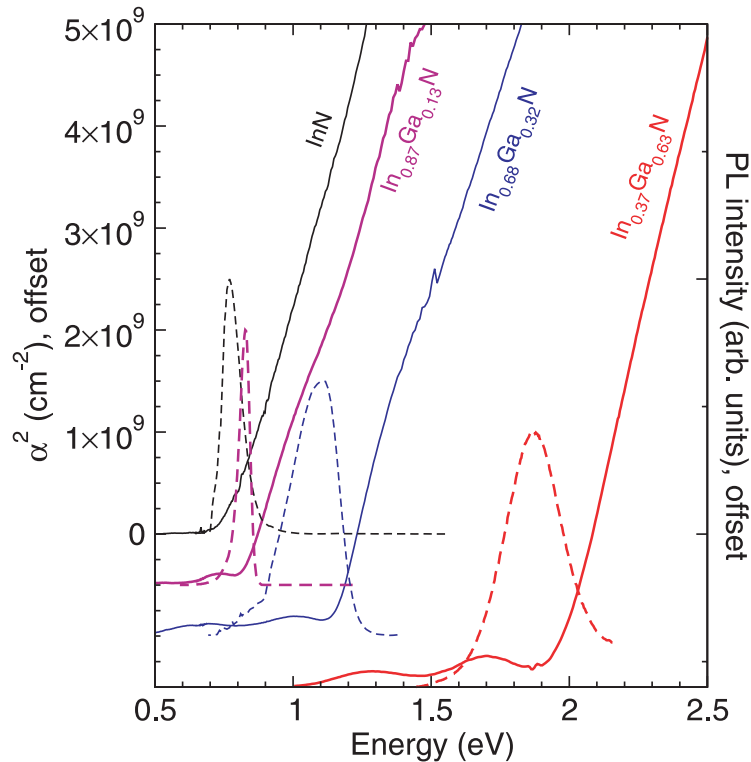


Figure 1.11: Photoluminescence (dashed line) and absorption (solid lines) spectra for InN and $In_xGa_{1-x}N$ alloys with different composition. The peak of the PL emission corresponds with the optical absorption edge. The figure is taken from [6].

1.4 Surface states and the charge neutrality level

The surface of a solid determines the boundary between the periodic potential inside the crystal and non-periodic potential outside the crystal. The break of the 3D periodic structure of the bulk together with any surface reconstruction and adsorption processes, lead to changes in the energetic structure near the surface. These changes result in the formation of energetic states, namely surface states. Historically, the first time the concept of the existence of surface states was proposed by Tamm [61] in 1932. He solved the problem of a perturbation in the periodic potential in a one

dimensional atomic chain, induced by the existence of the surface.

Within the nearly free electron model, the Schrödinger equation can give real solutions for real wavevectors, describing energy states for an infinite crystal. Moreover, the solutions predict the existence of a band gap. With the presence of the surface, real solutions for complex wavevectors are also possible and the corresponding wavefunctions physically describe the energy states at the surface which exponentially decay into the vacuum and into the bulk of the solid crystal. Additionally, within this model surface states can also be located within the band gap, and are sometimes named virtual gap states (ViGS) [62,63]. The complex band structure of a one dimensional lattice within the nearly free electron model is shown in Figure 1.12.

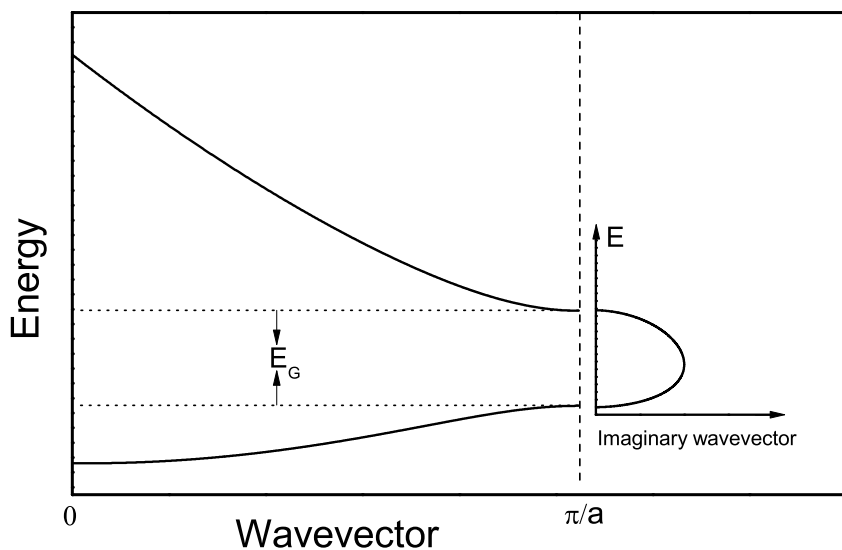


Figure 1.12: Schematic band structure of a linear lattice within the nearly free electron model.

Surface states can have either donor-like or acceptor-like character. They are separated by the energy level, called the charge neutrality level (CNL) [64,65] or the branch point energy [65] at which the probability of a state or defect being a donor or acceptor is the same. The surface states located above the CNL are predominantly acceptor-like and predominantly donor-like below this energy. The CNL for InN is located high in the conduction band about ~ 1.8 eV above the valence band maximum (VBM) [66]. In InN the surface Fermi level is located just below the CNL, indicating that some donor-like surface states are unoccupied. For GaN, the

CNL is located below conduction band minimum at ~ 2.4 eV above the VBM but still in the band gap. In this case the surface Fermi level is located above the CNL indicating that some acceptor-like surface states are occupied. The position of the CNL for InN, GaN and other semiconductor materials is presented in Figure 1.13. As the band gap of $\text{In}_x\text{Ga}_{1-x}\text{N}$ changes with the composition x (see Equation 1.1), the situation where all surface donor states are occupied and all surface acceptor states are unoccupied is expected. The investigations of surface electronic properties of $\text{In}_x\text{Ga}_{1-x}\text{N}$ are presented in Chapter 7.

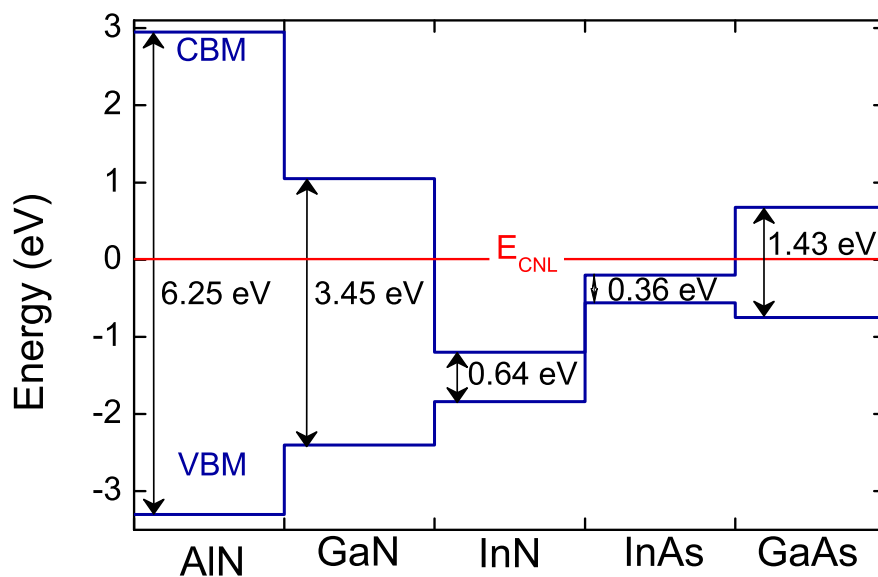


Figure 1.13: The conduction band minimum (CBM) and the valence band maximum (VBM) with respect to the charge neutrality level for AlN, GaN, InN, InAs and GaAs, and valence band offsets [55, 66–69]. The CNL for InN and InAs is located in the conduction band.

Surface Space Charge

If a semiconductor is not placed in an external electric field then it must be electrically neutral. The presence of unoccupied surface donor-like (occupied surface acceptor-like) states generates positively (negatively) charged surface. Therefore, the total charge due to surface states, Q_{ss} , must be compensated by an equal but opposite charge within the region near the surface, named the space charge region, Q_{sc} ,

$$Q_{ss} = -Q_{sc}. \quad (1.2)$$

In the case of an *n*-type semiconductor, where the surface Fermi level is located below (above) the CNL, the surface states are positively (negatively) charged, and this results in an electron accumulation (electron depletion) layer near the surface and this is achieved by downward (upward) bending of the bands. If the surface states are sufficiently negatively charged, then the surface Fermi level is pinned high above the CNL. Consequently, the upward bands bending is so severe that the surface Fermi level can be located below the middle of the direct band gap. This results in an accumulation of holes near the surface, separated from the *n*-type bulk region by a depletion region. This is known as an inversion layer. When the surface Fermi level is located exactly at the CNL, then the surface states are not charged and the bands are not required to bend to maintain charge neutrality. These considerations are also true for *p*-type material but in the opposite way. A schematic representation of the band bending and associated charge profiles for inversion, depletion, flat bands and accumulation space-charge layers at the surface of *n*- and *p*-type semiconductor is presented in Figure 2.3 in the Chapter 2.2.

Usually *n*-type III-V semiconductors exhibit an electron depletion layer near the surface, with the exception of InN and InAs, where a surface electron accumulation layer is observed [70–77]. This electron accumulation in both the materials can be explained by the extremely low conduction band minimum at the Γ point. Consequently the CNL is located in the conduction band; very high above the CBM in the case of InN, and the surface Fermi level is usually pinned below the CNL, resulting in an electron accumulation layer. Because the CNL for InN is located much higher in the conduction band than for InAs [66, 73], the degree of surface electron accumulation for InN is much greater.

If the downward band bending at the surface is narrow and sufficiently deep, then it can be also treated as a quantum potential well, found between the conduction band edge and the surface potential, and where the accumulated electrons are quantized. This has been confirmed by scanning tunneling spectroscopy (STS) measurements on InN(0001) [75, 78], as well as by angle-resolved photoemission spectroscopy (ARPES) [74, 79]. An ARPES photocurrent map of InN showing the

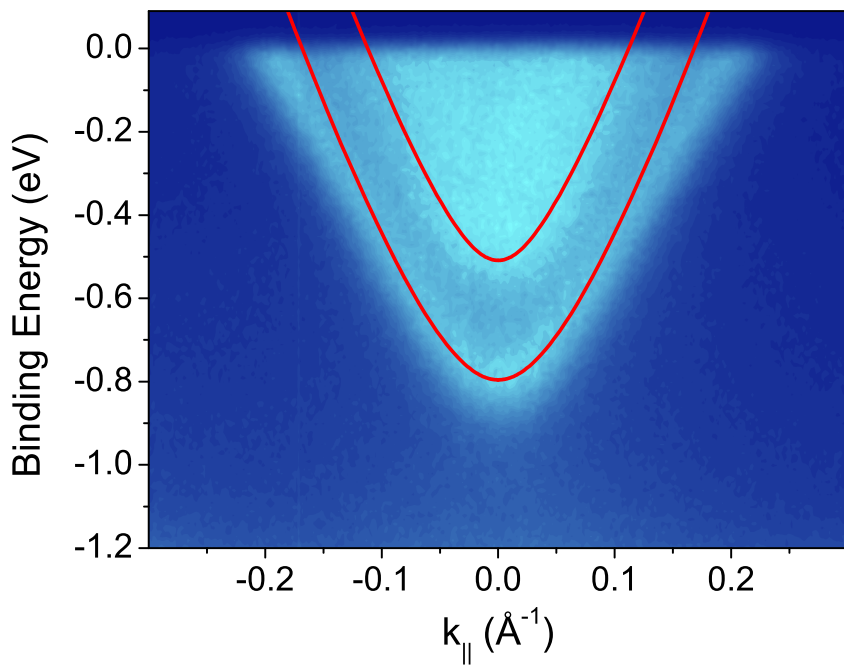


Figure 1.14: ARPES photocurrent intensity map of the parallel dispersion in the surface plane of two subbands in InN(0001) at 60 K (data adapted from [74]). The Fermi level is at 0 eV on this scale. The simulated subbands (red lines) have been calculated by solving Poisson’s equation within a modified Thomas-Fermi approximation and numerically solving the Schrödinger equation [79].

quantized states is presented in Figure 1.14.

Segev and Van de Walle [80–82] have suggested that the acceptor-like surface states in InN are associated with the presence of dangling bonds from InN at the clean surface, whereas the donor surface states are due to the presence of In adlayers at the surface. Therefore the absence of surface electron accumulation should be observed for a perfectly clean surface without any In-adlayers. This has been experimentally demonstrated using synchrotron radiation photoemission by Wu *et al.* on *in-situ* cleaved *a*-plane InN [83] grown by plasma assisted molecular beam epitaxy (PAMBE) on a Si(111) substrate with a GaN/AlN buffer layer.

1.5 Doping of InN and $\text{In}_x\text{Ga}_{1-x}\text{N}$

As-grown InN and $\text{In}_x\text{Ga}_{1-x}\text{N}$ semiconductors are always *n*-type. Modulation of their electrical properties might be obtained by intentionally introducing suitable elements inside the bulk of a material. However, control of conductivity type in semiconductors is an important issue for fabrication of a *p-n* junction, the most fun-

damental device structure.

1.5.1 Unintentional and intentional *n*-type doping of InN and $\text{In}_x\text{Ga}_{1-x}\text{N}$

The surface Fermi level in InN and $\text{In}_x\text{Ga}_{1-x}\text{N}$ is located either in the conduction band or close to the conduction band edge, suggesting that donors are the dominant defects in both the materials. Impurity atoms, such as H and O, unintentionally incorporated during a growth into the bulk of InN and $\text{In}_x\text{Ga}_{1-x}\text{N}$ significantly contribute to the native *n*-type conductivity in these materials [84]. Additionally, native defects are primarily donor-like, as explained by the amphoteric defect model (ADM) [85–87]. This is in agreement with experimental results showing that the undoped InN and $\text{In}_x\text{Ga}_{1-x}\text{N}$ alloys are always *n*-type [27, 77, 88, 89].

Intentional *n*-type doping of InN and $\text{In}_x\text{Ga}_{1-x}\text{N}$ alloys can be achieved by introduction of oxygen and silicon into the bulk [66]. In InN, Si is expected to occupy the In site (Si_{In}), while oxygen is expected to occupy the N site (O_{N}) [90]. Both these elements are shallow donors and have much lower formation energy than the nitrogen vacancy (V_{N}). These calculated formation energies for *zb*-InN are presented in Figure 1.15. DFT calculations have shown that formation energies of defects and impurities for the *wz*-InN are similar to those in the *zb*-InN, apart of interstitial configurations, for which the atomic environments are different [90, 91].

The other excellent candidate as an *n*-type dopant for InN and $\text{In}_x\text{Ga}_{1-x}\text{N}$ alloys could be germanium (Ge), since it is known to be a shallow donor in GaN [92, 93]. However, there are no reports regarding InN:Ge. Recently, Colussi *et al.* [94] reported that Ge should occupy In site (Ge_{In}) in InN nanowires.

1.5.2 *p*-type doping of InN and $\text{In}_x\text{Ga}_{1-x}\text{N}$

In terms of *p*-type conductivity, Mg has been proven to be an effective *p*-type dopant in GaN [95–99], therefore Mg is expected to be the most suitable candidate for *p*-type InN and $\text{In}_x\text{Ga}_{1-x}\text{N}$. Additionally, the atomic radius of Mg (~ 159.9 pm) is slightly smaller than atomic radius of In (~ 162.6 pm). Another promising element for doping InN would be Mn [100], however, the reported studies of Mn-doped InN

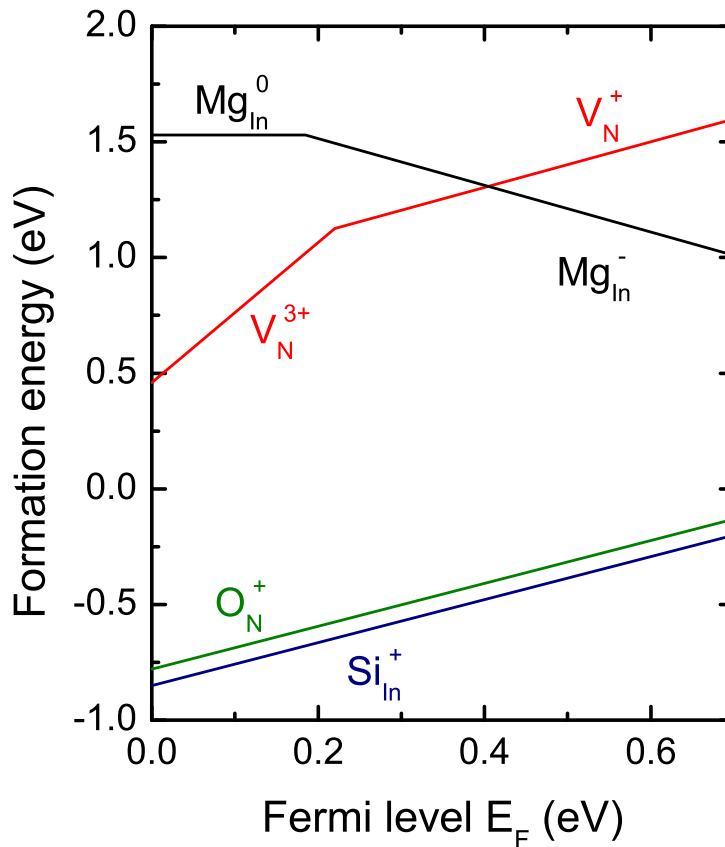


Figure 1.15: Calculated formation energies for Si_{In} , O_N , V_N and Mg_{In} as a function of the Fermi level with respect to the VBM for zinc-blende InN under In-rich conditions [90].

have been focused mainly on the magnetic properties rather than on the electrical and optical properties [101, 102].

Similarly to n -type, the surface Fermi level for p -type InN is usually pinned below the CNL in the conduction band [26, 103] but the electron accumulation in p -type InN is usually much more severe than for n -type InN, because more donor surface states are unoccupied. Due to the large electron accumulation, direct measurements, such as single-field Hall effect always reveal n -type conductivity. However, alternative techniques such multiple-field Hall effect measurements [103] and thermopower measurements [104] have given a clear indication of the existence of mobile holes in Mg-doped InN material.

An inversion layers can also be found at In-rich $In_xGa_{1-x}N$ surfaces, whereas Ga-rich $In_xGa_{1-x}N$ surfaces tend to exhibit a hole depletion region near the surface. A transition from a surface inversion layer for In-rich alloys to a surface hole

depletion layer for Ga-rich alloys has previously been observed by King *et al.* [28].

1.6 Control of surface electron accumulation

Because of the extreme degree of electron accumulation at the surface of InN and In-rich $\text{In}_x\text{Ga}_{1-x}\text{N}$, it is not a desirable feature for fabrication of some electronic devices. Hence it is necessarily to find an effective method to control the amount of surface electrons, without any interference on the bulk electronic properties. This can be achieved by the deposition of a suitable material onto the surface or by chemical treatment of the surface. A choice of material is very important, because the effects of controlling the surface accumulation should remain stable over a long period.

With regard to a reduction of the electron accumulation at InN and In-rich $\text{In}_x\text{Ga}_{1-x}\text{N}$ surfaces, a material with a high electronegativity could be used, due to charge transfer from the InN surface to the highly electronegative material. According to the Pauling scale, chlorine (Cl) is a highly electronegative element and its presence at the surface lowers the position of the surface Fermi level, reducing the electron accumulation [105]. However, In-Cl bonds are not thermally stable, and after annealing up to 300°C the chlorine atoms desorb from the surface. The other promising material is sulfur, which has previously been used to lower the position of the surface Fermi level in InN [106, 107] and passivate the surface to make it less chemically active [108]. Sulfur at the surface breaks the bonds between the indium atoms in the metal adlayers, and forms In-S bonds that enable the charge transfer. Sulfur has also been used successfully to passivate the surface in other III-V semiconductors like in InP [109], GaAs [110] or InAs [111–113], however, an increase of electron accumulation has been observed in the case of InAs, where the sulfur atoms substitute on the group V sites and act as a source of donors.

With regard to any increase in the surface electron accumulation, the deposition of an element with a small electronegativity would be required, providing the charge transfer from the element to the InN surface. The elements from the first group (alkali metals) of the periodic table have the lowest electronegativity.

Previous results show that the deposition of caesium onto InAs increases the surface Fermi level by ~ 0.6 eV [114]. Additionally, recent ARPES results from our group at the University of Warwick have shown that deposition of rubidium (Rb) onto the surface of CdO increases the electron accumulation at the surface of this material [115].

1.7 Thesis organisation

This thesis focuses on the surface and interface electronic properties of undoped and Mg-doped InN and $In_xGa_{1-x}N$ thin films. The basic theoretical details and approach (band structure, semiconductor space-charge calculations) used to interpret the experimental results are all outlined in Chapter 2. The experimental and computational methods employed during this research are then described in Chapter 3. Chapter 4 describes the investigations of the surface, bulk and interface electronic properties of non-polar InN, and in Chapter 5 the results and analysis of highly Mg-doped InN samples are described. Chapter 6 contains the results and analysis of sulfur passivation of high Mg-doped InN surface electron accumulation. The electronic properties of undoped $In_xGa_{1-x}N$ are presented in Chapter 7. Finally, future work and the main conclusions of this work are summarised in Chapter 8.

Chapter 2

Theoretical Background

This chapter consists of the necessary theoretical background relating to the band structure models of semiconductors with narrow band gaps. A knowledge of the relation between the electronic band structure and carrier densities, electron effective mass and Fermi levels positions allows the interpretation of the results presented in this thesis. The III-V semiconductors described here all exhibit non-parabolic conduction band dispersion, therefore the simple parabolic approximation is invalid for such materials. The non-parabolic approximations applied in this thesis are described in Section 2.1. Additionally, the solutions of Poisson's equation, describing the behaviour of band bending near the surface of a material, forms a very important component of this work and the theoretical details used are described in Section 2.2 of this chapter.

2.1 Band structure approximations

The theory of band structure is a quantum-mechanical description of the behaviour of electrons in crystalline solids. The free motion of electrons in a crystal is perturbed by the presence of a potential, arising from other electrons and the positive ions cores. The behaviour of electrons in such a solid is fully determined by the Schrödinger equation (2.1),

$$H|\psi\rangle = E|\psi\rangle \quad (2.1)$$

where E is energy of electron, ψ is a wavefunction and H is the Hamiltonian operator that describes interactions between electrons and ions, given by:

$$H = \sum_i \frac{\mathbf{p}_i^2}{2m_e} + \sum_l \frac{\mathbf{p}_l^2}{2M_l} + \sum_{i,l} V(\mathbf{r}_i - \mathbf{R}_l) + \sum_{l,m} U(\mathbf{R}_l - \mathbf{R}_m) + \sum_{i,j} \frac{e^2}{4\pi\epsilon_0} \frac{1}{|\mathbf{r}_i - \mathbf{r}_j|} \quad (2.2)$$

where i, j label the electrons, l, m label the ions, m_e and M are the electron and ion mass respectively, $V(\mathbf{r}_i - \mathbf{R}_l)$ and $U(\mathbf{R}_l - \mathbf{R}_m)$ are the valence electron-ion and interionic potential respectively. The momentum operator \mathbf{p} is given by

$$\mathbf{p} = -i\hbar\nabla. \quad (2.3)$$

The form of the Schrödinger equation (2.1) with the Hamiltonian given by (2.2) is very difficult to solve and so the following simplifications are used to reduce the Hamiltonian as in (2.2) to form equation (2.4)

- *adiabatic approximation (Born-Oppenheimer approximation)* - assumes that ion masses are much bigger than electron masses ($M \gg m_e$) so the distribution of electrons is immediately established at low variations of motion of the ions [116];
- *one electron approximation* - assumes that the interactions between the electrons are averaged [116];
- *mean-field approximation* - assumes that all electrons are in identical surroundings with the ions in their equilibrium positions [116].

$$H = \frac{\mathbf{p}^2}{2m_e} + V_0(\mathbf{r}) \quad (2.4)$$

where $V_0(\mathbf{r})$ is the periodic potential in the lattice.

Bloch's theory states that the solutions of equation (2.1) can be written as the product of complex plane wave and some periodic function

$$\psi_{\nu,\mathbf{k}}(\mathbf{r}) = u_{\nu,\mathbf{k}}(\mathbf{r}) \exp(i\mathbf{k} \cdot \mathbf{r}) \quad (2.5)$$

where ν labels the band, \mathbf{k} is the wavevector of the electron in the first Brillouin zone and $u_{\nu,\mathbf{k}}(\mathbf{r})$ is the periodic function with the full translational symmetry of the lattice. Hence

$$u_{\nu,\mathbf{k}}(\mathbf{r} + \mathbf{T}) = u_{\nu,\mathbf{k}}(\mathbf{r}) \quad (2.6)$$

where \mathbf{T} is a primitive translation vector.

2.1.1 Parabolic approximation

The parabolic approximation is useful when considering the energy dispersion around the centre of the Brillouin zone (the Γ -point) where the maximum of the valence band (VBM) and the minimum of conduction band (CBM) are located for many semiconductors. The dispersion relations for electrons or holes can be written as

$$E_{e,h}(\mathbf{k}) = E_{e,h}(0) \pm \frac{\hbar^2 \mathbf{k}^2}{2m^*} \quad (2.7)$$

where m^* is the effective electron or hole mass and $E_{e,h}(0)$ defines the zero of the energy scale [116]. For semiconductors with a large band gap this approximation is well satisfied. However, for materials with a narrow band gap, such as InN, the interactions between the valence and conduction bands cannot be neglected, therefore equation (2.7) cannot be used for the calculations.

2.1.2 $\mathbf{k}\cdot\mathbf{p}$ perturbation theory

A more useful and accurate method of band structure calculation is the $\mathbf{k}\cdot\mathbf{p}$ approach proposed by Kane [117]. Substituting the momentum operator given by (2.3) and wave function given by (2.5) into the Schrödinger equation (2.1) with the Hamiltonian given by (2.4) we obtain

$$\left[H_0 + \frac{\hbar}{m_e} \mathbf{k} \cdot \mathbf{p} + V_{so} + V_{cr} \right] u_{\nu\mathbf{k}}(\mathbf{r}) = \tilde{E}_{\nu\mathbf{k}}(\mathbf{r}) u_{\nu\mathbf{k}}(\mathbf{r}) \quad (2.8)$$

where $H_0 = \frac{\mathbf{p}^2}{2m_e} + V_0(\mathbf{r})$, $\tilde{E}_{\nu\mathbf{k}} = E_\nu(\mathbf{k}) - \frac{\hbar^2 \mathbf{k}^2}{2m_e}$ and V_{so} and V_{cr} denotes the spin-orbit and crystal-field potentials respectively. At the origin ($\mathbf{k} = (0, 0, 0)$) where the Γ -point is presented, equation (2.8) reduces to

$$[H_0 + V_{so} + V_{cr}] u_{\nu\mathbf{0}}(\mathbf{r}) = E_{\nu\mathbf{0}}(\mathbf{r}) u_{\nu\mathbf{0}}(\mathbf{r}). \quad (2.9)$$

The solutions of this equation form an orthonormal set. Therefore, the wavefunctions at any value of \mathbf{k} around the Γ -point and the energy eigenvalues can be expressed by treating the $\mathbf{k} \cdot \mathbf{p}$ interaction between the valence and conduction bands as perturbations. More details are presented in Appendix A.

In the region of the Γ -point, the conduction band is reasonably well approximated as isotropic but non-parabolic. The dispersion relation for the conduction electrons can be described by

$$E(E + \alpha E) = \frac{\hbar^2 k^2}{2m^*} \quad (2.10)$$

where $\alpha = 1/E_g$ is the non-parabolicity parameter in the so-called ‘ α ’ model [118, 119]. For large E_g , the α parameter becomes close to zero and the expressions for a parabolic conduction band are recovered.

For the zinc-blende structures the interaction between the three highest lying valence bands and the (doubly degenerate) conduction band is described by the Hamiltonian [117] given by

$$H = \begin{pmatrix} \tilde{H} & 0 \\ 0 & \tilde{H} \end{pmatrix} \quad (2.11)$$

where

$$\tilde{H} = \begin{pmatrix} E_s & 0 & kP & 0 \\ 0 & E_p - \Delta_{so}/3 & \sqrt{2}\Delta_{so}/3 & 0 \\ kP & \sqrt{2}\Delta_{so}/3 & E_p & 0 \\ 0 & 0 & 0 & E_p + \Delta_{so}/3 \end{pmatrix}. \quad (2.12)$$

Here E_s and E_p are the conduction and valence band energies respectively, Δ_{so} is the spin-orbit splitting of the valence band and P is Kane’s matrix element [79], which is given by

$$P^2 = \frac{3\hbar^2 \left(\frac{1}{m^*} - \frac{1}{m_e} \right)}{2 \left(\frac{2}{E_g} + \frac{1}{(E_g + \Delta_{so})} \right)}. \quad (2.13)$$

For InN the spin-orbit splitting (Δ_{so}) is only 5 meV and can be neglected because $\Delta_{so} \ll E_g$ [120, 121] therefore the matrix (2.12) reduces to the form

$$H = \begin{pmatrix} E_s & kP \\ kP & E_p \end{pmatrix}. \quad (2.14)$$

The conduction band is described by

$$E_c(\mathbf{k}) = E' + E_k \quad (2.15)$$

where

$$E_k = \frac{\hbar^2 \mathbf{k}^2}{2m_e} \quad (2.16)$$

and E' is the eigenvalue of the Hamiltonian, given by the solution of secular equation

(2.17)

$$E'(E' + E_g) - k^2 P^2 = 0 \quad (2.17)$$

where $E_s = 0$ and $E_p = -E_g$ has been chosen to define the zero of energy at the conduction band minimum (CBM). The solution of the secular equation (2.17) provides to the two-band $\mathbf{k} \cdot \mathbf{p}$ analytic form for the conduction band dispersion

$$E_c(k) = \frac{1}{2} \left[-E_g + \sqrt{E_g^2 + 4k^2 P^2} \right] + E_k \quad (2.18)$$

where Kane's matrix element is simplified to

$$P^2 = \frac{\hbar^2}{2m_e} \left(\frac{m_e}{m^*} - 1 \right) E_g. \quad (2.19)$$

The electron density in a semiconductor depends on the band gap, the position of the Fermi level and the free carrier effective mass. Within the quantum mechanical Fermi-Dirac statistics, describing the probability that a set of electronic states are occupied, the electron concentration is given by

$$n = \int_0^\infty g_c(E) f_{FD}(E) dE \quad (2.20)$$

where the Fermi-Dirac distribution function is given by

$$f_{FD}(E) = \frac{1}{1 + \exp[\beta(E - \mu)]} \quad (2.21)$$

where $\beta = 1/k_B T$ and μ is the chemical potential. The density of conduction band states is defined as

$$\begin{aligned} g_c(k) &= \frac{k^2}{\pi^2} \left[\frac{dE_c(k)}{dk} \right]^{-1} \\ &= \frac{k/\pi^2}{2P^2[E_g^2 + 4k^2 P^2]^{-1/2} + (\hbar^2/m_e)} \end{aligned} \quad (2.22)$$

and the energy dependent electron effective mass

$$\begin{aligned} m^*(E) &= \hbar^2 k \left[\frac{dE_c(k)}{dk} \right]^{-1} \\ &= \frac{\hbar^2/k}{2P^2[E_g^2 + 4k^2 P^2]^{-1/2} + (\hbar^2/m_e)}. \end{aligned} \quad (2.23)$$

A comparison of the conduction band dispersion relations calculated from the parabolic, α and two-band $\mathbf{k} \cdot \mathbf{p}$ approximations near Γ -point for InN is shown in Figure 2.1.

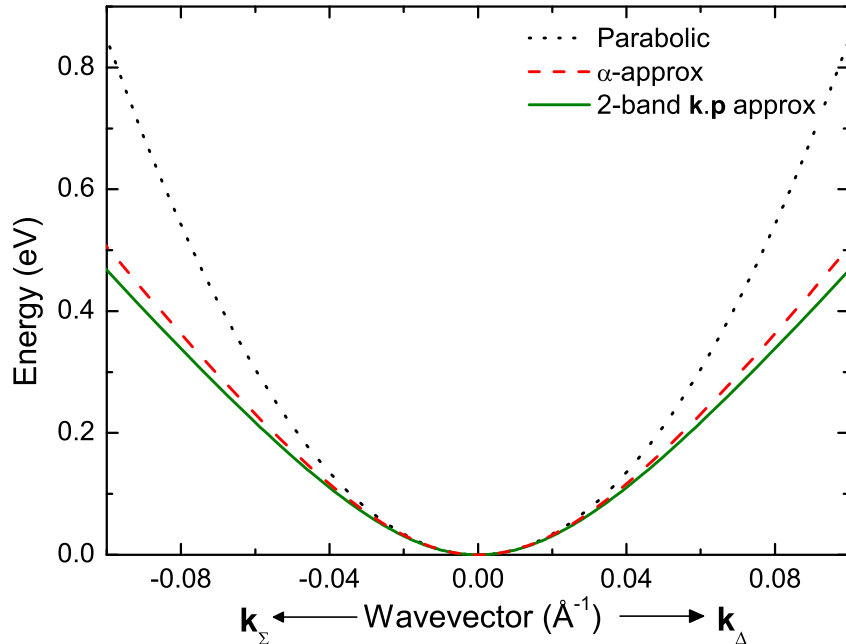


Figure 2.1: A comparison of the conduction band dispersion relations calculated using different approximations for zinc-blende InN.

For a wurtzite structure, the $\mathbf{k} \cdot \mathbf{p}$ Hamiltonian (2.11) should not be used for calculations, because it does not reflect the symmetry of the crystal. A more useful approach is an 8×8 Hamiltonian (2.24) developed by Suzuki and Uenoyama [122] that describes the 3 highest-lying valence bands and interaction with the conduction band.

$$H = \begin{pmatrix} H_{cc} & H_{cv} \\ H_{cv}^\dagger & H_{vv} \end{pmatrix} \quad (2.24)$$

where H_{cc} and H_{vv} are 2×2 and 6×6 matrices for the conduction and valence band, respectively. H_{cv} is the 2×6 Hamiltonian describing the interaction between conduction and valence bands and \dagger denotes the Hermitian conjugate. The matrix elements of equation (2.24) are given by

$$H_{cc} = \begin{pmatrix} E_c & 0 \\ 0 & E_c \end{pmatrix} \quad (2.25)$$

$$H_{cv} = \begin{pmatrix} Q & 0 & R & 0 & Q^* & 0 \\ 0 & Q & 0 & R & 0 & Q^* \end{pmatrix} \quad (2.26)$$

$$H_{vv} = \begin{pmatrix} F & 0 & -H^* & 0 & K^* & 0 \\ 0 & G & \Delta & -H^* & 0 & K^* \\ -H & \Delta & \lambda & 0 & I^* & 0 \\ 0 & -H & 0 & \lambda & \Delta & I^* \\ K & 0 & I & \Delta & G & 0 \\ 0 & K & 0 & I & 0 & F \end{pmatrix} \quad (2.27)$$

where $*$ denotes the complex conjugate and

$$E_c = E_s + \frac{\hbar^2 k_z^2}{2m_e^{\parallel}} + \frac{\hbar^2 k_{\perp}^2}{2m_e^{\perp}} \quad (2.28a)$$

$$Q = \frac{1}{\sqrt{2}} P_{\perp} k_{+} \quad (2.28b)$$

$$R = P_{\parallel} k_z \quad (2.28c)$$

$$F = \Delta_{cr} + \frac{\Delta_{so}}{3} + \lambda + \theta \quad (2.28d)$$

$$G = \Delta_{cr} - \frac{\Delta_{so}}{3} + \lambda + \theta \quad (2.28e)$$

$$H = i\tilde{A}_6 k_z k_{+} - \tilde{A}_7 k_{+} \quad (2.28f)$$

$$I = i\tilde{A}_6 k_z k_{+} + \tilde{A}_7 k_{+} \quad (2.28g)$$

$$K = \tilde{A}_5 k_{+}^2 \quad (2.28h)$$

$$\Delta = \sqrt{2} \frac{\Delta_{so}}{3} \quad (2.28i)$$

$$\lambda = E_p + \tilde{A}_1 k_z^2 + \tilde{A}_2 k_{\perp}^2 \quad (2.28j)$$

$$\theta = \tilde{A}_3 k_z^2 + \tilde{A}_4 k_{\perp}^2 \quad (2.28k)$$

$$k_{\pm} = k_x \pm ik_y \quad (2.28l)$$

$$k_{\perp}^2 = k_x^2 + k_y^2 \quad (2.28m)$$

E_s is the average conduction band edge

$$E_s = E_p + E_g + \Delta_{cr} + \frac{\Delta_{so}}{3} \quad (2.29)$$

where E_p is the average valence band edge, Δ_{cr} is the crystal field splitting, Δ_{so} is

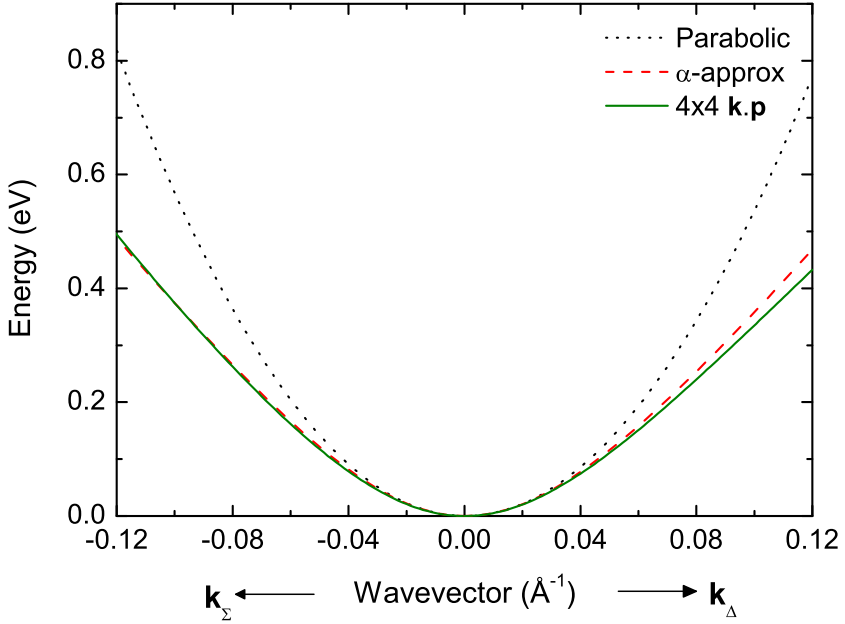


Figure 2.2: A comparison of the conduction band dispersion relations calculated from different approximations for wurtzite InN.

the spin-orbit splitting. Parameters \tilde{A}_i describe the valence bands [123]

$$\tilde{A}_1 = A_1 + \frac{2m_e}{\hbar^2} \frac{P_\perp^2}{E_g} \quad (2.30a)$$

$$\tilde{A}_2 = A_2 \quad (2.30b)$$

$$\tilde{A}_3 = A_3 - \frac{2m_e}{\hbar^2} \frac{P_\perp^2}{E_g} \quad (2.30c)$$

$$\tilde{A}_4 = A_4 + \frac{m_e}{\hbar^2} \frac{P_\parallel^2}{E_g} \quad (2.30d)$$

$$\tilde{A}_5 = A_5 + \frac{m_e}{\hbar^2} \frac{P_\parallel^2}{E_g} \quad (2.30e)$$

$$\tilde{A}_6 = A_6 + \frac{\sqrt{2}m_e}{\hbar^2} \frac{P_\parallel P_\perp}{E_g} \quad (2.30f)$$

$$\tilde{A}_7 = A_7. \quad (2.30g)$$

For wurtzite InN the 8×8 Hamiltonian (2.24) reduces to 4×4 Hamiltonian (2.31) as the spin-orbit splitting is very small and can be neglected.

$$H = \begin{pmatrix} E_c & Q & R & Q^* \\ Q^* & F & -H^* & K^* \\ R^* & -H & \lambda & H^* \\ Q & K & H & F \end{pmatrix} \quad (2.31)$$

A comparison of the conduction band dispersion relations calculated from the parabolic, α and $4 \times 4 \mathbf{k} \cdot \mathbf{p}$ approximations near Γ -point for InN is shown in Figure 2.2.

2.2 Space charge calculations

2.2.1 Poisson's equation

If a point charge is put into a locally neutral electron plasma, the electrons in the neighbourhood will rearrange to compensate for that additional charge; i.e. it will be screened, such that far away from the charge the electric field vanishes. The higher the electron density, the shorter the range over which the electrons rearrange in order to establish an effective shielding. The spatial regions of redistributed screening charge are called ‘space charge regions’ [124].

The one-electron potential $V(z)$, describing the band bending in space-charge regions, must satisfy Poisson’s equation [63].

$$\frac{d^2V}{dz^2} = \frac{e}{\varepsilon(0)\varepsilon_0}[N_A^- - N_D^+ - p(z) + n(z)] \quad (2.32)$$

where $\varepsilon(0)$ denotes the static dielectric constant, N_A^- (N_D^+) is the bulk ionized acceptor (donor) density - $p(z)$ ($n(z)$) is the hole (electron) density and z is the depth from the surface into the bulk of semiconductor. The potential $V(z)$ must also satisfy the boundary conditions

$$V(z) \rightarrow 0 \text{ as } z \rightarrow \infty \quad (2.33)$$

indicating that there is no band bending in the bulk of the semiconductor and

$$\left. \frac{dV}{dz} \right|_{z=0} = \frac{e}{\varepsilon(0)\varepsilon_0} n_{SS} \quad (2.34)$$

where n_{SS} is the surface state density.

If $V(z) < 0$, then the bands bend upward and the related space charge has a positive sign, while for $V(z) > 0$ the bands bend downward [63].

2.2.2 Modified Thomas-Fermi approximation

Within the modified Thomas-Fermi approximation (MTFA) [125], the potential is calculated by solving the Poisson equation taking into account the boundary conditions (2.33) and (2.34) with the carrier densities corresponding to the conduction and valence bands given by

$$n(z) = \int_0^{\infty} g_c(E) f'_{FD}(E) f(z) dE \quad (2.35)$$

$$p(z) = \int_{E_V}^{-\infty} g_v(E) f'_{FD}(E) f(z) dE \quad (2.36)$$

where $f(z)$ is the MTFA factor to account for the potential barrier at the surface [126], and $f'_{FD}(E)$ is the Fermi-Dirac function including the potential dependence

$$f(z) = 1 - \text{sinc} \left[\frac{2z}{L} \left(\frac{E}{k_B T} \right)^{\frac{1}{2}} \left(1 + \frac{E}{E_g} \right)^{\frac{1}{2}} \right] \quad (2.37)$$

$$f'_{FD}(E) = \frac{1}{1 + \exp[\beta(E - \mu + V(z))]} \quad (2.38)$$

where $\text{sinc}(x) = \frac{\sin(x)}{x}$. L , for non-degenerate semiconductors, is a characteristic length which describes the range of the influence of the interface in dependence on the effective mass perpendicular to the interface $L = \hbar/(2m_0^* k_B T)^{1/2}$. For degenerate semiconductors, $L = 1/k_F$ is Fermi length, where k_F is the Fermi wavevector [126]. The correction factor $f(z)$ describes the interference of incident and reflected wavefunctions caused by the potential barrier at the surface and thus leads the carrier concentration to tend smoothly to zero at the surface.

A numerical solution of equation 2.32, using a trial potential $V(z)$ and interval bisection method allows the band bending potential and the carrier concentration profiles to be found as function of depth. Examples are shown in the Figure 2.3.

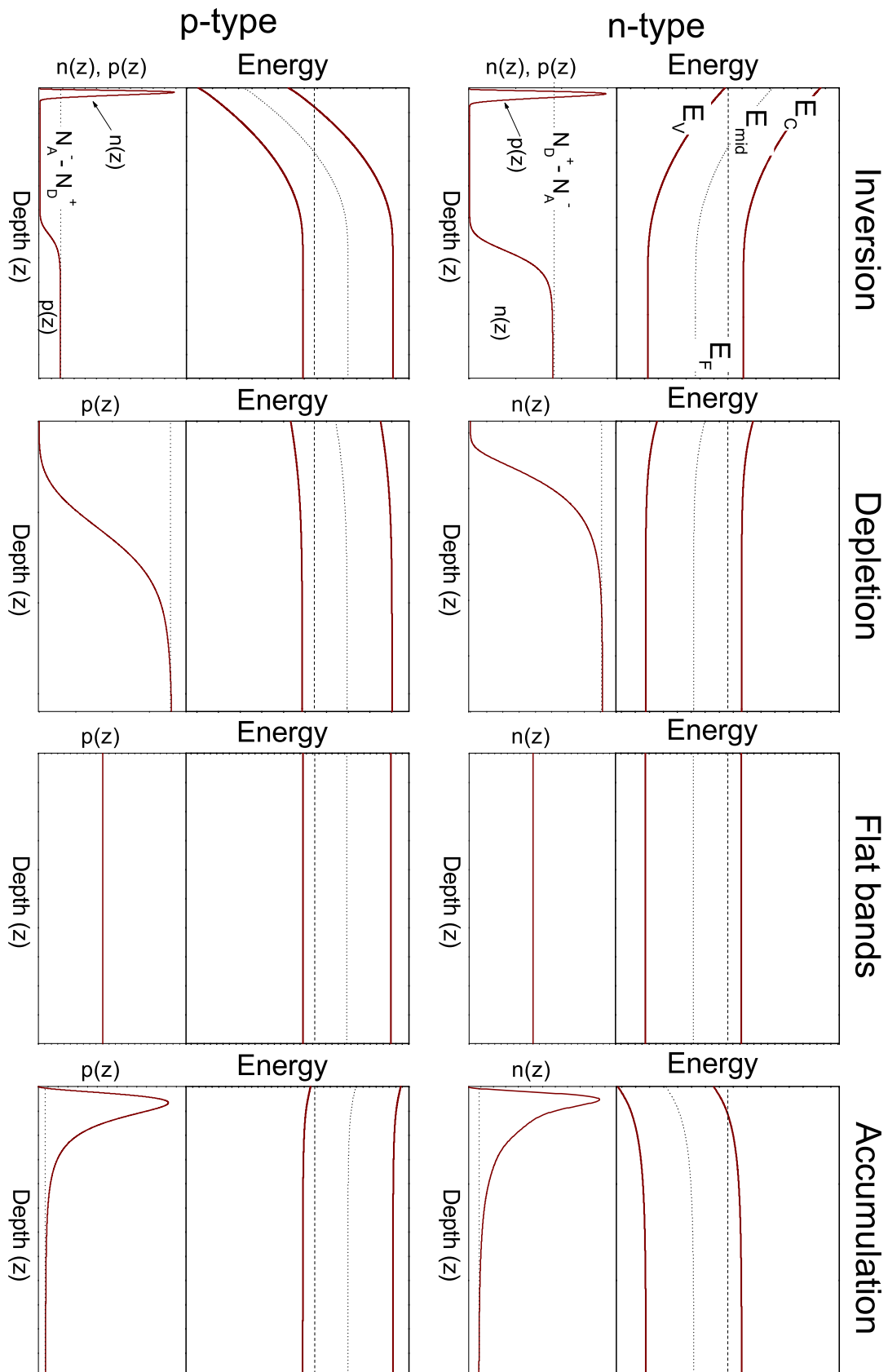


Figure 2.3: A schematic representation of the band bending and associated charge profiles for inversion, depletion, accumulation space charge layers at the surface.

2.3 Summary

The theoretical details presented in this section are applicable for the materials considered in this work and they will be widely used throughout this thesis. The electronic structure approximations used to perform the Fermi-Dirac statistics calculations to determine the density of electrons and holes in the considered materials have been outlined. Because InN and In-rich $\text{In}_x\text{Ga}_{1-x}\text{N}$ alloys exhibit an electron accumulation layer near the surface, therefore the space charge calculations will be performed by solving the Poisson's equation within MTFA approximation, described in this chapter.

Chapter 3

Experimental and computational methods

The following chapter contains an introduction to the physical background of experimental techniques used; including X-ray photoemission spectroscopy (XPS), infrared reflectance spectroscopy (FTIR), secondary ion mass spectrometry (SIMS), electrochemical capacitance-voltage measurements (ECV) and the single-field Hall effect measurements. In addition, the computational methods of analysing reflectivity spectra and electrolyte capacitance-voltage Mott-Schottky plots are also described.

3.1 X-ray photoemission spectroscopy

X-ray photoemission spectroscopy (XPS) measures the distribution of emitted photoelectrons following photo-ionisation to study the composition and electronic state of the surface region of a material. XPS employs the photoelectric effect, discovered by Hertz in 1887 and explained by Einstein in 1905. A sample is exposed to monoenergetic X-ray photons of energy $h\nu$ which can be absorbed by a solid, leading to ionisation and the emission of core-level and/or valence electrons. The simplified emission process is shown in Figure 3.1. The emitted photoelectrons have a characteristic kinetic energy E_k , determined by the Einstein equation

$$E_k = h\nu - E_B - \phi_{\text{anal}} \quad (3.1)$$

where E_B is the binding energy of the electron and ϕ_{anal} is the work function of the analyser [127]. The binding energy is the difference between the initial and final energies, which includes the component of relaxation and which is lower than the energy of the orbital from which the photoelectron was emitted. Photoemission is a complex process that can be explained by a three step model [128]. In the first step, interaction with a photon excites the electron from its initial state (Ψ_i) into a final state (Ψ_f). This process is described by the Fermi's Golden Rule where the

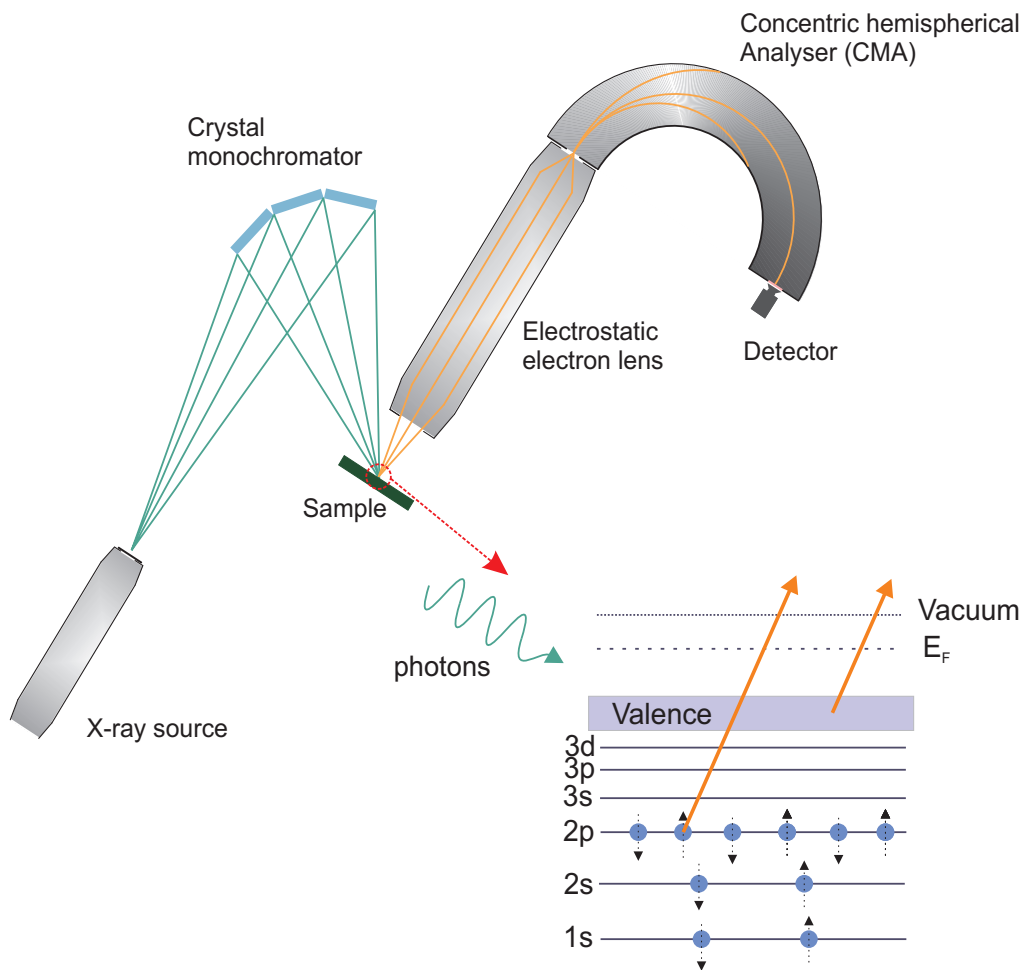


Figure 3.1: Schematic representation of X-ray photoemission spectroscopy and core-level and valence photoelectron emission processes. The sample is exposed to monochromated X-ray photons of energy $h\nu$, leading to the emission of core level and valence electrons. The energy distribution of these electrons are measured by the detector.

transition probability (Ω) is expressed as

$$\Omega = | \langle \Psi_f | H_{int} | \Psi_i \rangle |^2 \delta(E_f - E_i - h\nu) \quad (3.2)$$

where H_{int} is the Hamiltonian for the electron-photon interaction. The electron transition from the initial state to the final state must obey both energy and momentum conservation. For an energy E and a wave vector \mathbf{k} the internal current is given by

$$I_{int}(E, h\nu, \mathbf{k}) = \sum_{f,i} | \langle \Psi_f | H_{int} | \Psi_i \rangle |^2 f(E_i) \delta(E_f(\mathbf{k}) - E_i(\mathbf{k}) - h\nu) \delta(E - E_f(\mathbf{k})) \delta(\mathbf{k}_i + \mathbf{G} - \mathbf{k}_f) \quad (3.3)$$

where $f(E_i)$ is the Fermi distribution function.

In the second step a photoelectron has to travel some distance inside the solid before it escapes into the vacuum. During this time it can be elastically or inelastically scattered, predominantly by other electrons, but also by ionised impurities or phonons. Elastic collisions do not change the kinetic energy, while inelastic collisions lead to a decrease in kinetic energy. Inelastically scattered electrons either contribute to the background of photoemission spectra or do not escape from the solid. The last step is the transmission of the photoelectron into the vacuum. To escape the material, the kinetic energy E_k has to be large enough to overcome the surface barrier. Electrons whose E_k is too small get reflected back inside and remain inside the solid.

The total intensity of photoelectrons emitted from a depth L below the surface without loss of energy can be described by the Beer-Lambert law

$$I(E) = I_0(E)e^{-L/\lambda \sin \theta} \quad (3.4)$$

where the parameter λ is the inelastic mean free path (IMFP) of electrons, θ is the photoemission angle, and $I_0(E)$ is the initial intensity of emitted photoelectrons of energy E . The IMFP for a particular material can be estimated by TPP-2M predictive equations of Tanuma *et al.* [129].

Conversion of photoelectron kinetic energy into binding energy using equation 3.1 requires a knowledge of the analyser work function. Alternatively, the binding energy of a core level in a metallic reference sample can be used. Throughout this work the position of Fermi edge of an argon ion bombarded silver (Ag) or gold (Au) sample has been used for the binding energy scale calibration.

Every element has a characteristic XPS spectrum, therefore the chemical composition of a sample can be determined. Furthermore, the intensity of the photoelectron peaks is related to the concentration of the element within the sampled region. The binding energy of a core-level electron also depends on the chemical environment of the atom. For instance, an oxidation state or different bonding configuration leads to binding energy shift, which is usually named a chemical shift.

3.1.1 Background

The typical structure of an XPS spectrum of InN is shown in Figure 3.2. The spectrum contains a number of relatively narrow photoelectron peaks, which correspond to core-level states. The step-like background is formed by inelastically scattered electrons. For non-monochromatic radiation, photoemission increases the background and the spectra would be complicated by the presence of satellite peaks. The analysis of the peak shape and the stoichiometry, from an experimental spectrum, requires a subtraction of the background. Several models of background shape can be used. A linear-type background can be used for fast spectra analysis, while for accurate analysis of semiconductor XPS spectra a Shirley background should be applied [130].

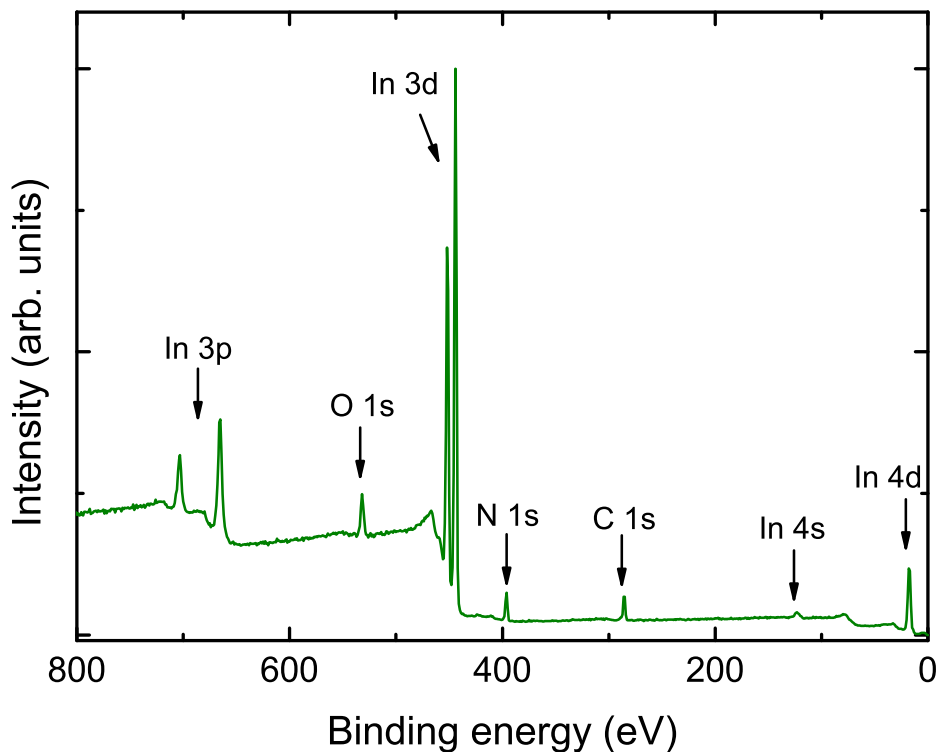


Figure 3.2: XPS wide energy scan from InN ($h\nu=1486.6$ eV). The spectrum shows a number of photoelectron peaks, which correspond to core-level emission. The step-like background is formed by inelastically scattered electrons. The Fermi level is defined as zero on the binding energy scale.

3.1.2 Core-level peaks

As mentioned above, the XPS spectrum shown in Figure 3.2 consists of a set of core-level peaks. In accordance with notation universally used in photoemission spectroscopy, each peak should be labelled in the following format

$$\mathbf{X} \ n\ell_j$$

where \mathbf{X} denotes the element, $n = 1, 2, 3\dots$ is the principal quantum number, $\ell = (s = 0, p = 1, d = 2, f = 3\dots)$ denotes the orbital angular momentum quantum number and j is the total orbital angular momentum quantum number, including information about the spin moment of the electron, and defined as $j = \ell \pm 1/2$. The s -levels are always characterized by a single peak, as the only source of angular momentum is the spin moment, whereas core-levels that have $\ell \neq 0$ exhibit a doublet structure due to spin-orbit coupling. The spin-orbit coupling causes a shift of the energy level by an amount given by

$$\Delta E_{so} \propto \xi(n\ell)[j(j+1) - \ell(\ell+1) - s(s+1)] \quad (3.5)$$

where $\xi(n\ell)$ is the spin-orbit coupling constant [131]. Hence, the doublets of In $3p_{3/2}$ and In $3p_{1/2}$ or In $3d_{5/2}$ and In $3d_{3/2}$ are observed with the lower j level occur at higher binding energy.

The width ΔE of an XPS peak can be defined as the full width at half-maximum (FWHM) after background subtraction. The natural width of a core level ($\Delta E(n)$), spectral width of photon source radiation ($\Delta E(p)$), the analyser resolution ($\Delta E(a)$) and the phonon broadening ($\Delta E(\omega)$) contribute to the FWHM and therefore

$$\Delta E = \sqrt{\Delta E(n)^2 + \Delta E(p)^2 + \Delta E(a)^2 + \Delta E(\omega)^2} \quad (3.6)$$

Additionally, each peak can be broadened by differential charging or by sample inhomogeneity. The life-time broadening is described by a Lorentzian profile, whereas the analyser broadening is very well described by a Gaussian profile.

The shape of a core-level XPS peak depends on the peak type and on the metallic or insulating nature of the measured sample. Additionally, the excitations

of conduction band plasmons at the surface have a remarkable influence on the peak shape. In reality, each peak potentially contains several overlapping components due to the coexistence of different chemical states for the same element. The peak shape for a semiconductor material can be well described by the mixed Gaussian and Lorentzian profile, called a Voigt lineshape.

3.1.3 Auger process

Apart from the standard emission of a photoelectron from the sample during X-ray illumination it is possible to eject a second electron as a consequence of relaxation processes. This is known as the Auger effect and it is schematically represented in Figure 3.3. After photoemission of an electron from the shell K, the vacancy created can be filled by an electron from one of the upper levels (L level in Figure 3.3). As a result, the released energy of $E = E_K - E_L$ can be emitted in a radiative process or can be used to eject a second electron (Auger electron) from a higher level (M level in Figure 3.3) in a radiationless transition. The direction of ejection of the Auger electron is random and independent of the incident excitation energy. The range of the Auger electrons increases with the atomic number Z of the atom.

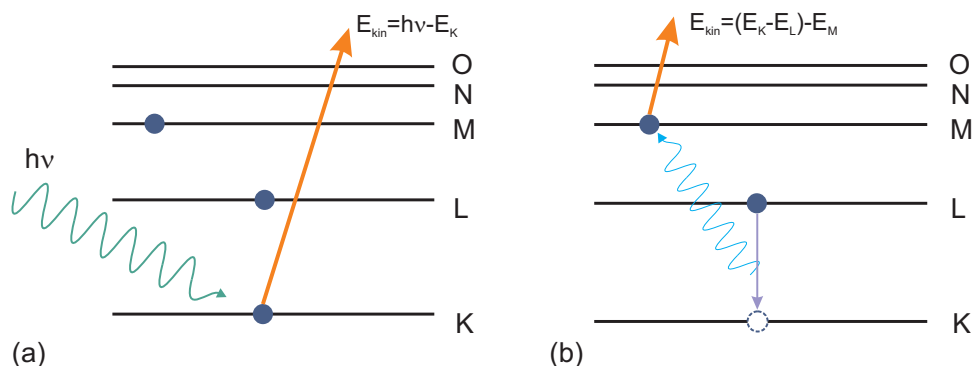


Figure 3.3: Illustration of KLM Auger process. (a) Emission of the photoelectron from the K shell with the kinetic energy $E_{kin} = h\nu - E_K$ and (b) the Auger transition in which the electron from L level fills the vacancy in K level releasing which can be used to eject an Auger electron from level M with kinetic energy $E_{kin} = (E_K - E_L) - E_M$.

3.1.4 Scienta ESCA-300 Spectrometer

The XPS data presented in Chapters 4 and 5 were collected at room temperature using a Scienta ESCA300 spectrometer at the National Centre for Electron

Spectroscopy and Surface analysis (NCESS), Daresbury Laboratory, UK. The system consists of a 300 mm diameter rotating anode Al-K_α X-ray source, a seven α – quartz crystals monochromator, a 300 mm mean radius hemispherical analyser and a multi-channel CCD detector. Additional details of the spectrometer can be found in Ref. [132]

The X-rays (Al-K_α, $h\nu = 1486.6$ eV) are produced by the rotating anode (~ 10000 rpm) and are directed into a monochromator chamber, where they are reflected by the seven α – quartz crystals. This removes the formation of deceleration radiation and satellite X-ray lines. A total linewidth of the X-ray source as a combination of the width of the electron beam on the anode and the diffraction width of the monochromator is ~ 0.26 eV [133].

The sample is mounted on a four axis manipulator, and is exposed to the monochromated X-rays. Emitted electrons are collected by the 300 mm mean radius electron energy analyser. Typically, the analyser was operated at a pass energy of 150 eV and with 0.8 mm slits. For these conditions the total resolution of the instrument is 0.40 ± 0.05 eV and it has been calculated from the convolution of linewidth of the X-ray source and analyser broadening. However, it is possible to operate the analyser with a pass energy of 20 to 1000 eV with different slit widths (from 0.2 mm to 4 mm), but the total resolution of the instrument will be different. The binding energy scale was calibrated by the Fermi edge position of an ion-bombarded silver (Ag) reference sample.

Samples were mounted on stubs, either with tantalum foil contacts or carbon tape and loaded into the system through a load lock which is pumped by a turbomolecular pump to a base pressure of $\sim 1 \times 10^{-6}$ mbar. Using a wobble stick the sample was introduced into a preparation chamber, where it could be annealed or sputtered. The pressure in the preparation chamber was 1×10^{-9} mbar and it is obtained by oil diffusion pump with a liquid nitrogen cool trap. The transfer of a sample from the preparation chamber onto the manipulator in the spectrometer chamber was performed by wobble sticks and a rack and pinion railway transfer system. The pressure in this part of the system was typically $\sim 5 \times 10^{-10}$ mbar.

3.1.5 Omicron SPHERA 125 Spectrometer

The XPS data, presented in Chapters 6 and 7 were obtained at the University of Warwick using a new Omicron SPHERA 125 spectrometer. The samples were again probed using a monochromated Al-K α X-rays with a linewidth of 0.25 eV. The emitted photoelectrons are collected by a 125 mm mean radius electrostatic hemispherical deflection analyser, composed of two concentric hemispheres. The spectrometer consists of a large slit (5 mm) and two sets of 7 slits (3 mm and 1 mm), one for each of the 7 channeltrons. The effective instrumental resolution obtained from the Gaussian convolution of the analyser broadening with a linewidth of 0.25 eV leads to 0.33 eV at a pass energy of 5 eV, or 0.47 eV at pass energy of 10 eV.

The samples were mounted onto sample plates with carbon tape or tantalum wire straps spot-welded to the sample plate and introduced to the load lock which was pumped by a turbomolecular pump to a base pressure of $\sim 1 \times 10^{-8}$ mbar. Then, it was transferred into a preparation chamber with a linear transfer arm, where the sample usually was annealed. The preparation chamber was pumped by a turbomolecular pump to a base pressure of $\sim 2 \times 10^{-10}$ mbar. After the preparation, the sample is transferred into analyser chamber and mounted on a four axis manipulator, allowing to perform measurements at the different take off angles of the photoelectrons. The base pressure of the analysis chamber was $\sim 3 \times 10^{-11}$ mbar and it was obtained by both TSP and ion pumps.

Summarising, both the XPS systems have a similar instrumental resolution, however, the system at the University of Warwick has a lower X-ray flux than the NCESS system provides. Hence, much longer scans are required to obtain good quality spectra. Additionally, the vacuum conditions are better in the system at Warwick, preventing adsorption of contaminations at the surface of a material.

3.2 Infrared reflectance spectroscopy

Infrared reflectance spectroscopy is a non-destructive technique that utilises infrared (IR) light to analyse the optical properties of a sample. In this technique the inten-

sity of light that is reflected from a sample is measured for a range of wavelengths. Measurements presented in this thesis have been performed using a Fourier transform IR (FTIR) spectrometer with a Michelson interferometer, shown schematically in Figure 3.4. The collimated light from an IR source impinges on a beam-splitter which reflects 50% of the light and transmits the remaining part. The reflected light hits a fixed mirror where it is reflected again, while the transmitted part of the beam is reflected by a moveable mirror. The light returning from the two mirrors is recombined at the beamsplitter. After reflecting off the sample, the light reaches a detector, providing an interferogram.

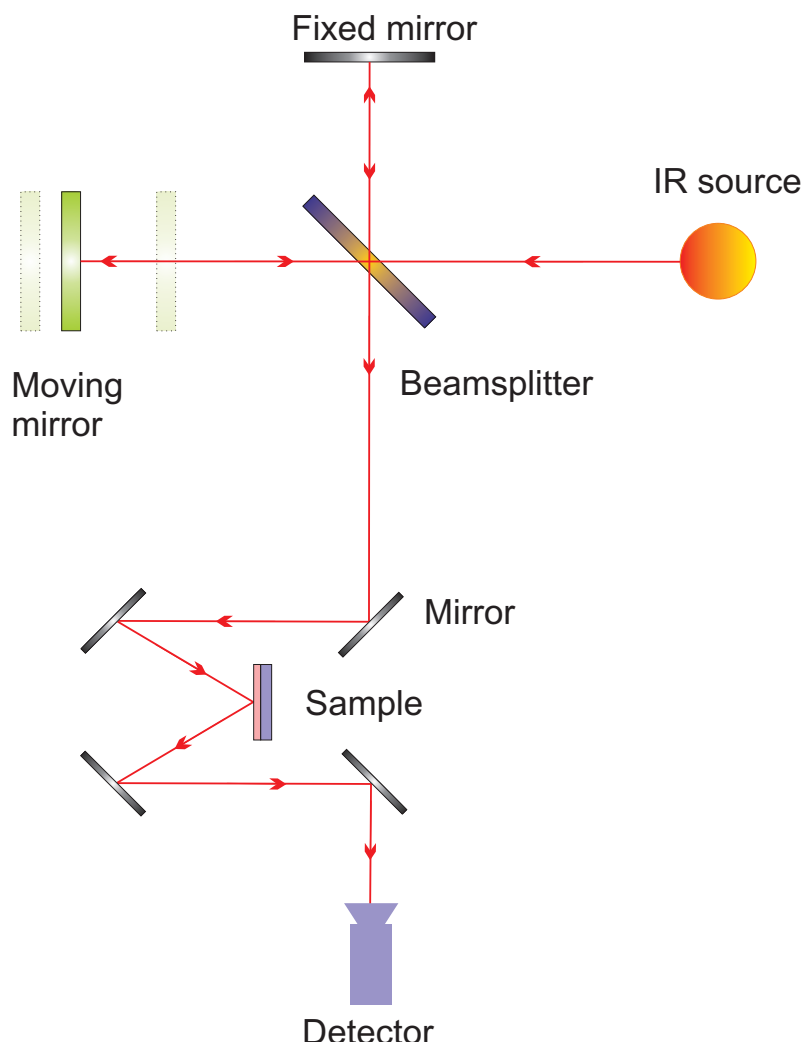


Figure 3.4: Schematic of FTIR spectrometer showing the Michelson interferometer and reflectivity measurements. The light beam coming from the source is split by a semi-transparent mirror into two beams, which are reflected back by two mirrors. The returning beams interfere at the beam-splitter and the resulting light is directed onto the sample. The reflected light is then directed to the detector.

Comparing the recorded spectra to simulated data can provide particularly information about phonons and free carriers in the material. The incident IR light induces collective oscillations of the free electron gas (plasmon) in the sample with a frequency (known as the plasma frequency) ω_p , where

$$\omega_p^2 = \frac{ne^2}{\epsilon_0 \epsilon(\infty) \langle m^*(E) \rangle} \quad (3.7)$$

where $\langle m^*(E) \rangle$ denotes the conduction band density of states averaged electron effective mass, described by

$$\langle m^*(E) \rangle = \frac{\int_0^\infty m^*(E)g(E)f_{FD}(E)dE}{\int_0^\infty g(E)f_{FD}(E)dE} \quad (3.8)$$

The $g(E)$ and $f_{FD}(E)$ in Equation 3.8 denote the density of states and the Fermi-Dirac factor, respectively.

3.2.1 Two-oscillator dielectric function

The reflectivity of a semi-infinite material at normal incidence is given by [134];

$$R = \left| \frac{(n + ik) - 1}{(n + ik) + 1} \right|^2 = \frac{(n - 1)^2 + k^2}{(n + 1)^2 + k^2} \quad (3.9)$$

where $n + ik$ is the complex refractive index. In the two-oscillator model, the refractive index is equal to the square root of the dielectric function

$$n + ik = \sqrt{\epsilon} = \tilde{n} \quad (3.10)$$

and

$$\epsilon = \epsilon(\infty) + \frac{[\epsilon(0) - \epsilon(\infty)]\omega_{TO}^2}{\omega_{TO}^2 - \omega^2 - i\omega\gamma} - \frac{\epsilon(\infty)\omega_p^2}{\omega(\omega + i/\tau)} \quad (3.11)$$

where $\epsilon(\infty)$ and $\epsilon(0)$ are the high-frequency and static dielectric constants of the material, respectively, ω_{TO} (γ) is the frequency (damping) of the transverse optical phonon and ω_p (τ) is the frequency (lifetime) of the plasmon. The reflectivity can therefore be written in terms of the dielectric function as

$$R = \left| \frac{\tilde{n} - 1}{\tilde{n} + 1} \right|^2 \quad (3.12)$$

3.2.2 Factorised dielectric model

A factorised dielectric model, proposed by Berreman and Unterwald [135] considers anharmonic coupling of phonons in multiple phonon mode crystals with polar character. The dielectric function within this model can be written as

$$\varepsilon = \varepsilon(\infty) \prod_{i=1}^l \frac{\omega_{LO_i}^2 - \omega^2 - i\omega\gamma_{LO_i}}{\omega_{TO_i}^2 - \omega^2 - i\omega\gamma_{TO_i}} \quad (3.13)$$

where $\varepsilon(\infty)$ denotes the high frequency dielectric constant and γ_{TO} and γ_{LO} are the transverse and longitudinal optical phonon damping coefficient, respectively. The transverse and longitudinal optical phonon frequencies are denoted as ω_{TO} and ω_{LO} , respectively.

The product model is more general as it includes coupling effects between LO and TO phonon modes which are unnecessarily neglected in the conventional model (sum model) that does not allow independent broadening for TO and LO phonons. In the sum model, the assumption that two polar relaxors respond independently to the electric field is rather unphysical [136, 137]. The product model is commonly used to calculate the dielectric function for multiphonon crystals [136]. In this thesis, the factorised model was used to simulate the dielectric function of sapphire. The parameters used in the IR reflectivity simulations are presented in Appendix B.

3.2.3 IR reflectivity simulation - transfer matrix formalism

The general transfer matrix method (TMM), proposed by Katsidis and Siapkas [138], has been used to simulate reflectivity spectra. The multilayer structure with electric field amplitudes is shown schematically in Figure 3.5. In this formalism, the subscripts of the field amplitudes indicate the medium. The right- and left-going waves are denoted by + and -, respectively, and additionally the wave on the right side of an interface is marked by prime (') sign. The amplitudes of electric field on left side, E_{j-1}^{\pm} , and right side, $E_j'^{\pm}$, of the j th interface can be related as

$$\begin{pmatrix} E_{j-1}^+ \\ E_{j-1}^- \end{pmatrix} = \mathbf{D}_{j-1}^{-1} \mathbf{D}_j \begin{pmatrix} E_j'^+ \\ E_j'^- \end{pmatrix} \quad (3.14)$$

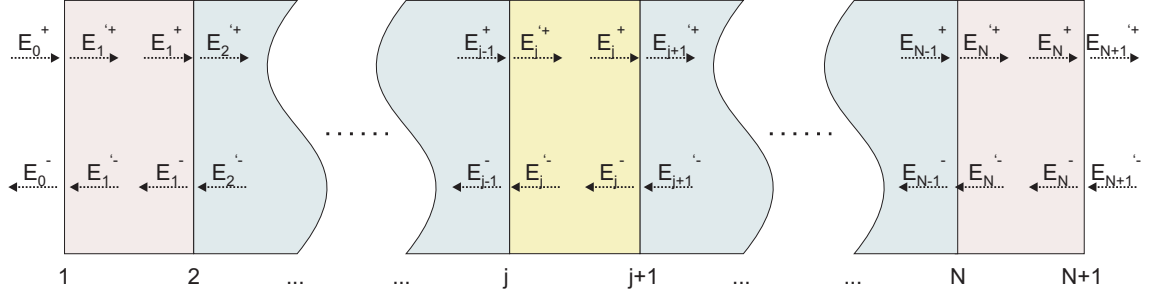


Figure 3.5: Schematic multilayer structure composed of N layers and $N+1$ interfaces. The right- and left-going waves are denoted by + and -, respectively, and additionally the wave on the right side of an interface is marked by prime (') sign.

where $\mathbf{D}_{m-1}^{-1}\mathbf{D}_m$ is a dynamical 2×2 matrix. Its elements are complex Fresnel coefficients for transmission and reflection at the j th interface

$$r_{j-1,j} = \frac{E_{j-1}^-}{E_{j-1}^+} \Big|_{E_j'^{-}=0} = \frac{D_{21}}{D_{11}} \quad (3.15a)$$

$$t_{j-1,j} = \frac{E_j'^+}{E_{j-1}^+} \Big|_{E_j'^{-}=0} = \frac{1}{D_{11}} \quad (3.15b)$$

$$r_{j,j-1} = \frac{E_j'^-}{E_j'^+} \Big|_{E_{j-1}^+=0} = -\frac{D_{12}}{D_{11}} \quad (3.15c)$$

$$t_{j,j-1} = \frac{E_{j-1}^-}{E_j'^+} \Big|_{E_{j-1}^+=0} = \frac{\det(\mathbf{D}_{j-1}^{-1}\mathbf{D}_j)}{D_{11}} \quad (3.15d)$$

Each plane wave can be decomposed to *p*-polarised (transverse magnetic) and *s*-polarised (transverse electric) component, therefore the complex Fresnel coefficients should be treated separately for each polarisation, and they are given by [139];

$$r_{j-1,j}^s = \frac{\tilde{n}_{j-1} \cos \theta_{j-1} - \tilde{n}_j \cos \theta_j}{\tilde{n}_{j-1} \cos \theta_{j-1} + \tilde{n}_j \cos \theta_j} \quad (3.16a)$$

$$r_{j-1,j}^p = \frac{\tilde{n}_j \cos \theta_{j-1} - \tilde{n}_{j-1} \cos \theta_j}{\tilde{n}_{j-1} \cos \theta_j + \tilde{n}_j \cos \theta_{j-1}} \quad (3.16b)$$

$$t_{j-1,j}^s = \frac{2\tilde{n}_{j-1} \cos \theta_{j-1}}{\tilde{n}_{j-1} \cos \theta_{j-1} + \tilde{n}_j \cos \theta_j} \quad (3.16c)$$

$$t_{j-1,j}^p = \frac{2\tilde{n}_{j-1} \cos \theta_{j-1}}{\tilde{n}_{j-1} \cos \theta_j + \tilde{n}_j \cos \theta_{j-1}} \quad (3.16d)$$

Amplitudes of the electric fields in a medium j are related by the propagator matrix

\mathbf{P}_j

$$\begin{pmatrix} E_j'^+ \\ E_j'^- \end{pmatrix} = \mathbf{P}_j \begin{pmatrix} E_j^+ \\ E_j^- \end{pmatrix} \quad (3.17)$$

where

$$\mathbf{P}_j = \begin{bmatrix} \exp(-i\delta_j) & 0 \\ 0 & \exp(i\delta_j) \end{bmatrix} \quad (3.18)$$

and δ_j is the phase change of light in medium j of thickness d_j

$$\delta_j = \frac{2\pi}{\lambda} \tilde{n}_j d_j \cos \theta_j \quad (3.19)$$

Substituting equation 3.17 into equation 3.14, the 2×2 total transfer matrix \mathbf{T} for the N layer system with $N + 1$ interfaces can be described as

$$\begin{aligned} \begin{pmatrix} E_0^+ \\ E_0^- \end{pmatrix} &= \mathbf{D}_0^{-1} \left[\prod_{j=1}^N \mathbf{D}_j \mathbf{P}_j \mathbf{D}_j^{-1} \right] \mathbf{D}_{N+1} \begin{pmatrix} E'_{N+1}^+ \\ E'_{N+1}^- \end{pmatrix} \\ &= \begin{bmatrix} T_{11} & T_{12} \\ T_{21} & T_{22} \end{bmatrix} \begin{pmatrix} E'_{N+1}^+ \\ E'_{N+1}^- \end{pmatrix} = \mathbf{T} \begin{pmatrix} E'_{N+1}^+ \\ E'_{N+1}^- \end{pmatrix} \end{aligned} \quad (3.20)$$

and hence, similarly to equation 3.15a, the total reflection coefficient is determined as

$$r = \frac{T_{21}}{T_{11}} \quad (3.21)$$

For unpolarised light, the total reflectivity is calculated as the incoherent average of polarised reflection coefficients r^s and r^p

$$R = \frac{1}{2}(R^s + R^p) = \frac{1}{2}(|r^s|^2 + |r^p|^2) \quad (3.22)$$

If the multilayer system contains a rough j th interface then it is more relevant to introduce partially coherent interface into TMM [140], than the coherent interface described above. It can be obtained by modification of the Fresnel coefficient of the interest j th interface, by terms that represent the phase differences

$$r_{j-1,j} = r_{j-1,j}^{(0)} \exp[-2(2\pi Z n_{j-1}/\lambda)^2] \quad (3.23a)$$

$$r_{j,j-1} = r_{j,j-1}^{(0)} \exp[-2(2\pi Z n_j/\lambda)^2] \quad (3.23b)$$

$$t_{j-1,j} = t_{j-1,j}^{(0)} \exp[-1/2(2\pi Z/\lambda)^2(n_j - n_{j-1})^2] \quad (3.23c)$$

$$t_{j,j-1} = t_{j,j-1}^{(0)} \exp[-1/2(2\pi Z/\lambda)^2(n_{j-1} - n_j)^2] \quad (3.23d)$$

where the superscripts (0) denote Fresnel coefficients of smooth interfaces, and Z is the rms height.

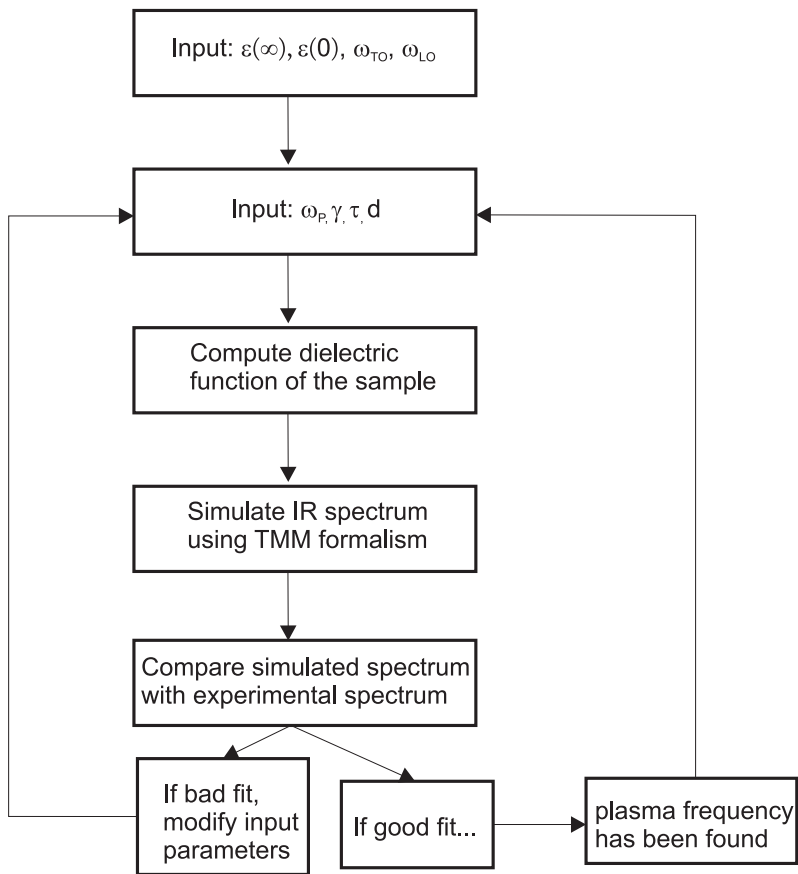


Figure 3.6: Schematic block diagram of method used when simulating IR spectra. Parameters such as the high-frequency ($\varepsilon(\infty)$) and static dielectric constants ($\varepsilon(0)$) of the material, transverse (ω_{TO}) and longitudinal (ω_{LO}) phonons, phonons damping (γ), plasma frequency (ω_P) and lifetime (τ) of the plasmon were used to simulate IR spectra.

All simulated IR spectra presented in this thesis were computed using a program written by the author based on the general transfer-matrix method described above. A schematic diagram of this program is presented in Figure 3.6.

3.2.4 Bruker Vertex 70v Fourier Transform IR Spectrometer

The infrared reflectivity measurements reported in these thesis were performed using a Bruker Vertex 70v Fourier transform IR spectrometer. The spectrometer is based on a Michelson interferometer, the principle of operation of which is briefly described in section 3.2. The IR reflectivity data presented in Chapters 4 and 7 are collected for a spectral range of 40 meV to 800 meV. This range is available by using a mid infrared source, potassium bromide beam-splitter and liquid nitrogen cooled mercury cadmium telluride (MCT) detector. All measurements were performed at

room temperature and at a pressure of 1.33 mbar to reduced the effects caused by water vapour or CO₂ absorptions.

3.3 Hall effect

Single field Hall effect measurements were taken when a sample was placed in a magnetic field with the current flowing normal to the magnetic field. This experiment can give information about the bulk carrier concentration and mobility, but for semiconductors with a surface accumulation layer the carrier density is typically over estimated. The geometry of Hall effect measurements is depicted in Figure 3.7. An electric current is passed through the semiconductor block via contacts at either end while a magnetic field $\mathbf{B} = (0, 0, B_z)$ is applied perpendicularly to both the surface and the electric current. The Lorentz force generates the transverse electric field $\mathbf{E} = (E_x, E_y, 0)$ perpendicular to the direction of current flow [141], satisfying the relations

$$\frac{ev_{hy}}{\mu_h} = eE_y - ev_{hx}B_z \quad (3.24a)$$

$$\frac{ev_{ey}}{\mu_e} = eE_y + ev_{ex}B_z \quad (3.24b)$$

where v_{hy} and v_{ey} are the hole and electron drift velocities along y , μ_e and μ_h are the electron and hole drift mobilities. Substituting $v_{hx} = \mu_h E_x$ and $v_{ex} = \mu_e E_x$ these become

$$\frac{v_{hy}}{\mu_h} = E_y - \mu_h E_x B_z \quad (3.25a)$$

$$\frac{v_{ey}}{\mu_e} = E_y + \mu_e E_x B_z \quad (3.25b)$$

Assuming that in the y -direction there is no net current, therefore

$$J_y = J_h + J_e = epv_{hy} + env_{ey} = 0 \quad (3.26)$$

and hence

$$pv_{hy} = -nv_{ey} \quad (3.27)$$

where n/p is the density of electrons/holes. The total current density in the x -direction is finite and is given by

$$J_x = (p\mu_h + n\mu_e)eE_x \quad (3.28)$$

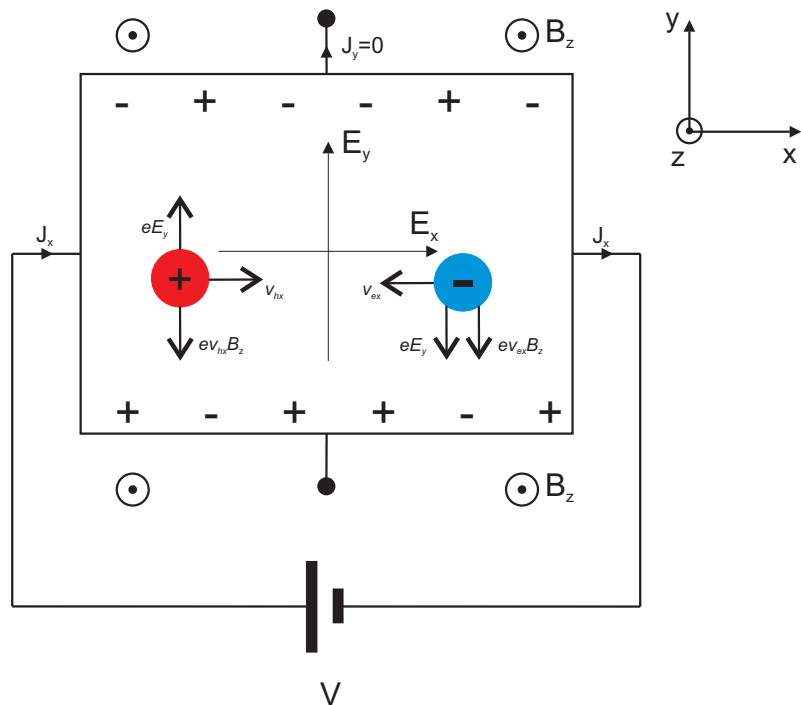


Figure 3.7: Schematic view of Hall effect measurements. An electric current is passed through the semiconductor block and a magnetic field is applied perpendicularly to both the surface and the electric current. Electrons/holes moving perpendicular to a magnetic field experience a force normal to the direction of motion and the applied field.

Considering Equations 3.25, 3.27 and 3.28 the following expression can be obtained

$$eE_y(n\mu_e + p\mu_h)^2 = B_z J_x(p\mu_h^2 - n\mu_e^2) \quad (3.29)$$

From this, the Hall coefficient, $R_H = E_y/J_x B_z$ can be determined, and in the presence of electrons and holes is given by

$$R_H = \frac{1}{|e|} \frac{(p\mu_h^2 - n\mu_e^2)}{(p\mu_h + n\mu_e)^2} \quad (3.30)$$

Furthermore, if electrons are dominant carriers in a semiconductor then equation 3.30 simplifies to

$$R_H = -\frac{1}{ne}. \quad (3.31)$$

3.3.1 Van der Pauw geometry

The van der Pauw geometry, shown schematically in Figure 3.8, has been used to determine the sheet resistance of a sample, type of doping, average density and carrier mobility. Van der Pauw demonstrated that there are two characteristics

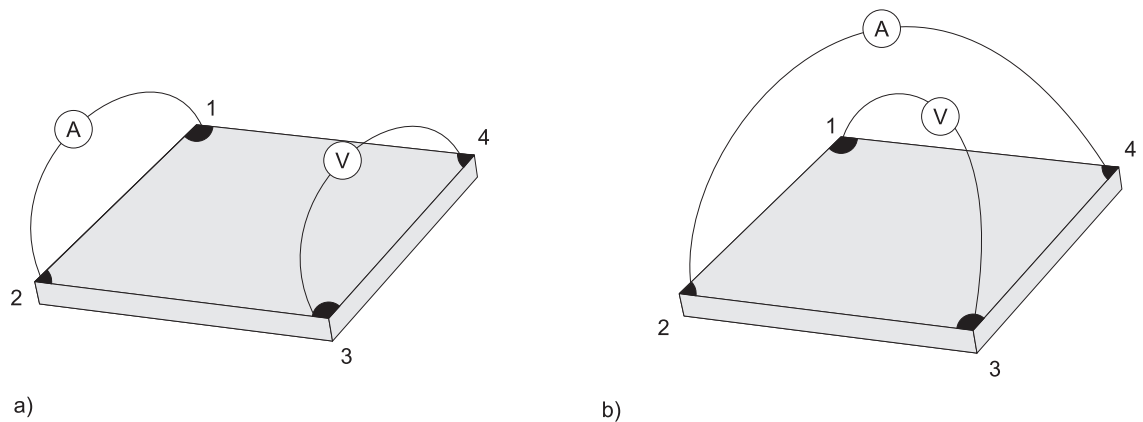


Figure 3.8: Schematic plan view of van der Pauw geometry for a) resistance measurements and b) Hall measurements.

resistances, R_A and R_B , associated with the four terminals [142]

$$R_A = \frac{V_{43}}{I_{12}} \quad R_B = \frac{V_{14}}{I_{23}} \quad (3.32)$$

where V_{34} (V_{14}) is the voltage measured across terminals 3 and 4 (1 and 4). I_{12} (I_{23}) is the current measured across terminals 1 and 2 (2 and 4). R_A and R_B relate to the sheet resistance (R_s) through the Van der Pauw equation

$$\exp(-\pi R_A/R_s) + \exp(-\pi R_B/R_s) = 1 \quad (3.33)$$

allowing the sheet resistance to be determined from simple electrical measurements.

For measuring a Hall voltage, a constant magnetic field must be applied perpendicularly to the sample surface. In the Van der Pauw's method, a current can be applied via a set of contacts on opposite corners, for example I_{24} , in the presence of either a positive or negative magnetic field. In this way the Hall voltage is measured between the other two corners, for example V_{13} . The average Hall voltage, is then given from

$$V_H = \frac{V_{13}^{B+} + V_{24}^{B+} + V_{31}^{B+} + V_{42}^{B+} - V_{13}^{B-} - V_{24}^{B-} - V_{31}^{B-} - V_{42}^{B-}}{8} \quad (3.34)$$

where $B+$ and $B-$ denotes the polarity of the magnetic field.

3.3.2 Hall effect measurements - Ecopia HMS-300 System

Hall effect results presented in this work were performed using an Ecopia HMS-300 measurement system. Samples were mounted on a plate using the van der Pauw

geometry discussed above. The measurements were performed at room temperature using a 0.55 T permanent magnet. The polarity of the magnetic field can be changed by rotating the magnet through 180°. Hall effect measurements were performed only if a linear current-voltage curve was obtained, indicating Ohmic contacts between each set of electrodes.

3.4 Electrochemical capacitance-voltage measurements

Electrolyte capacitance-voltage (ECV) profiling is a technique that enables the determination of free carrier concentration in a semiconductor and the etching of the material in a controlled electrolytic process. An electrolyte is used to make a barrier and to remove material electrolytically so both processes can be carried out in the same electrochemical cell and controlled electronically, using automatic equipment to perform the repetitive etch/measure cycle and generate a profile plot [143].

The schematic measurement setup is shown in Figure 3.9. If the surface of a semiconductor is in contact with the surface of a metal, a Schottky barrier is created as a consequence of electric charge redistribution between the metal and semiconductor. The surface carriers diffuse into the metal resulting in a depletion of carriers at the surface of the semiconductor. In ECV measurements, the Schottky-like barrier is formed by contact of the surface of the semiconductor with the electrolyte. Consequently, the semiconductor-electrolyte interface can act as capacitor of capacitance C , and the width of the depletion layer can be changed by applying an external voltage to the interface. If reverse bias is used then the depletion width is increased until breakthrough occurs, thus the capacitance is decreased. In the case when a forward bias is used, the depletion width is decreased until current starts flowing, thus capacitance is increased. The carrier concentration can be determined using the Mott-Schottky equation

$$N = \frac{-2}{e\epsilon_0\epsilon_R A^2 \frac{dC^{-2}}{dV}} \quad (3.35)$$

where ϵ_0 is vacuum permittivity, ϵ_R is dielectric constant of the semiconductor material, and A is measurement area.

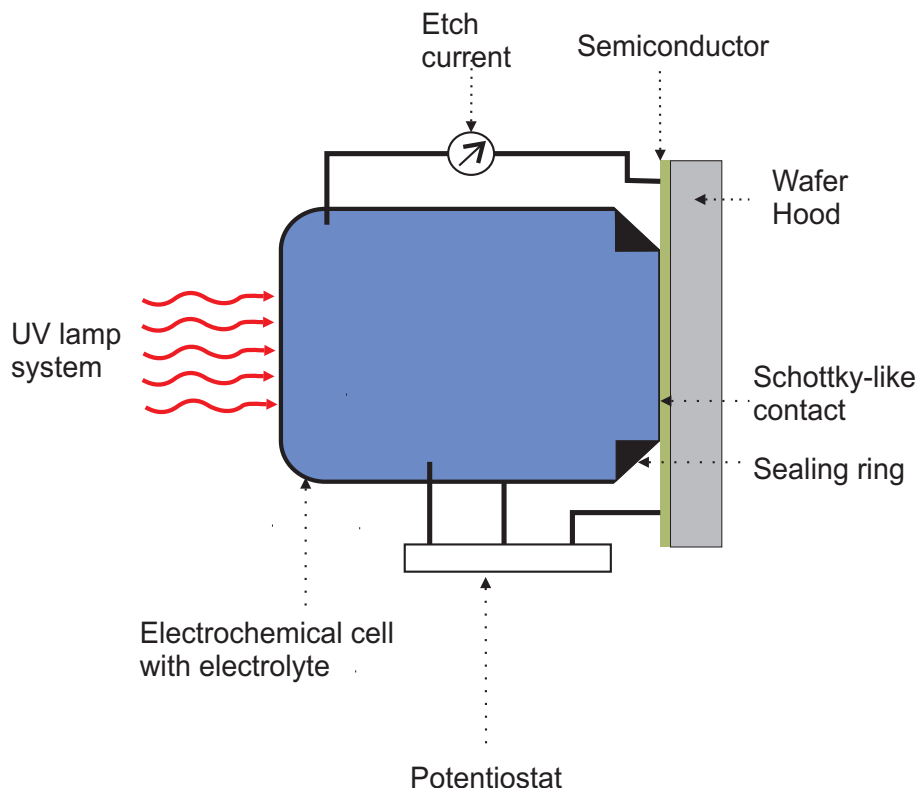


Figure 3.9: Schematic showing the measurement setup of ECV. An interface to the semiconductor surface is formed by the electrolyte, wetting a small area delimited by a sealing ring. The interface act as Schottky-like contact. UV light system is used to create electron-hole pairs at the surface of an n-type semiconductor.

The semiconductor is etched by illuminating the surface using UV light (for n-type layers) or in forward bias (for p-type layers). For an n-type semiconductor, the light is used to create electron-hole pairs at the surface. Recombination of electron-hole pairs causes the release of valence electrons forming the positively ionized atom cores which are dissolved into the electrolyte and these electrons move to the semiconductor contact. For p-type semiconductors, holes may be conducted from the semiconductor contact to the surface, by applying a forward bias. Through recombination, the valence electrons are released, and then ionized atom cores can be dissolved. This method of ECV profiling of semiconductors is an established technique that dates back to Ambridge and Faktor in 1974 [144], however, the traditional theory is invalid for semiconductors with an electron accumulation layer. During the UV illumination stage photons create electron-hole pairs at the surface, however, downward band bending acts a barrier preventing the generated holes from

reaching the surface. For semiconductors with large electron concentrations at the surface, it is reasonable to assume that the semiconductor/electrolyte junction is similar to a metal/electrolyte junction. However, the physics for such junctions is not still well understood, but the use of a double layer model is generally accepted, making use of an inner charge neutral ‘Helmholtz’ or ‘compact’ layer, of atomic width and an outer ‘Gouy-Champan’ or ‘diffuse’ layer [145].

Despite the difficulties described above, ECV measurements still can be useful to investigate the electronic properties of semiconductors with electron accumulation at the surface. The behaviour and shape of Mott-Schottky plots (C^{-2} vs V) that are experimentally produced, can be understood by comparison with simulated curves.

3.4.1 Simulating Mott-Schottky Plots

It has been shown (see section 2.2) that surface state density (n_{ss}) can be determined by integration of Equation 2.32 from $z = 0$ to $z = \infty$ with respect to depth

$$n_{ss} = \frac{\varepsilon_0 \varepsilon(0)}{e} \left. \frac{dV(z)}{dz} \right|_{z=0} \quad (3.36)$$

Therefore, from $C = \Delta Q / \Delta V$

$$\frac{\Delta(n_{sse})}{\Delta V_{bb}} \approx \frac{1}{A} \frac{\Delta Q}{\Delta V} C \quad (3.37)$$

where V_{bb} is the total band bending, which is always negative for films with an accumulation layer. Hence, the simulated surface gradients of the band bending diagrams produced by the method outlined in section 2.2 provide a means of simulating Mott-Schottky plots for given bulk and surface Fermi level values.

Relating these plots to experimental data requires knowledge of the band bending when there is no applied bias. It was assumed that all samples with an accumulation layer display $V_{bb} < 0$ when $V_{bias} = 0$. It was also assumed that the V_{bb} and V_{bias} axes scale in an identical manner.

3.4.2 ECV measurements - Dage Wafer Profiler CVP21

All ECV measurements reported here were performed using a Dage Wafer Profiler CVP21 system. The samples were placed in contact with an electrolyte (potassium

hydroxide was used here, in a 0.1 mol/litre solution). If necessary a layer of GaIn eutectic was used to ensure good electrical contact between the wafer and the two terminals supplying the current. Similarly to Hall effect measurements the I - V curve was checked to ensure that the contact exhibits Ohmic character. The rubber ring shown in Figure 3.9 forms a seal to prevent electrolyte leakage, and a 1 mm² area of the semiconductor surface is wetted. The I - V curve is checked again to ensure a Schottky-like contact. The rest potential, V_{rest} is measured by switching off the platinum current electrode, in order to measure the potential between a saturated calomel electrode (SCE) and the electrolyte interface.

A 3 terminal equivalent AC circuit [143] is used to model the electrolyte-semiconductor interface. A frequency, ω , is chosen such the dissipation

$$D = \text{Re}(Y)/\text{Im}(Y) \quad (3.38)$$

is minimised. Y was determined by

$$\frac{1}{Y} = R_s + \frac{1}{G + i\omega C} \quad (3.39)$$

where G is the parallel conductance of the interface, and R_s is the serial resistance. This method allows the capacitance per unit area, C/A , to be evaluated for a particular applied bias, V .

3.5 Secondary Ion Mass Spectrometry

Secondary ion mass spectrometry (SIMS) is the mass analysis of ionized particles which are emitted when a surface is bombarded by energetic ions [146]. The vast majority of species emitted are neutral but it is the secondary ions which are detected and analysed by a mass spectrometer. A schematic of SIMS is shown in Figure 3.10. Different materials produce different characteristic ions which can be used to identify the composition. It is extremely surface selective; most of the signal comes from the surface or close to the surface of the sample. SIMS is particularly good at providing information about thin film doping concentrations by the method of depth profiling [127], however, it is destructive.

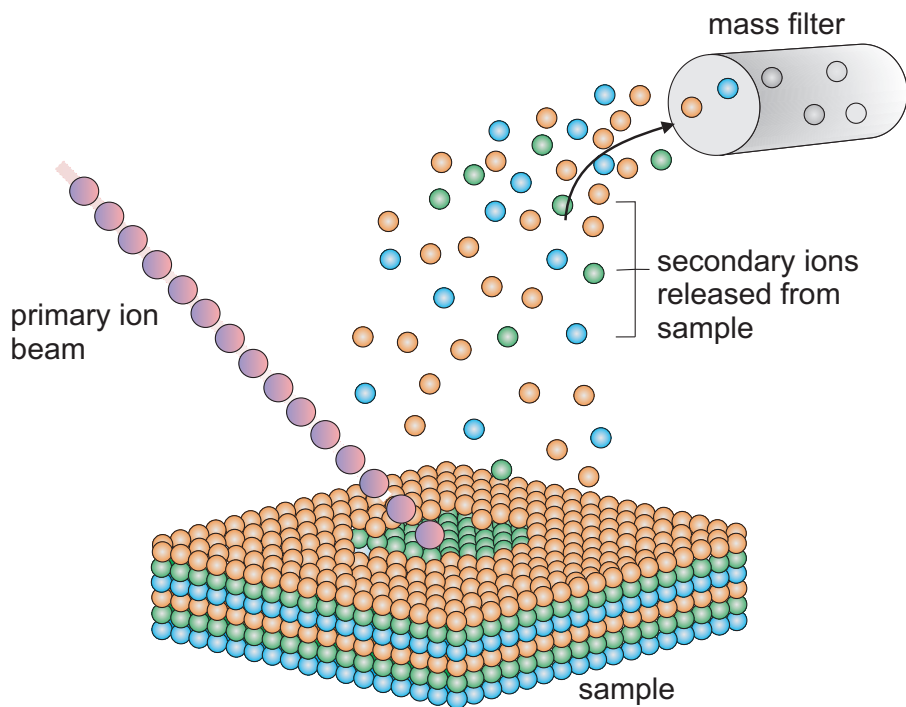


Figure 3.10: Schematic representation of the sputtering process during SIMS measurements. The primary ion beam is used to sputter the sample surface and release secondary ions. These secondary ions can then be separated and analysed using mass spectrometry.

The SIMS instrument consists of a primary ion source and a mass spectrometer, all enclosed in an ultra high vacuum chamber. Ion bombardment and emission of secondary ions can cause a positive charging of the sample and consequently suppression of the emission of negative ions and increase of the energy of emitted positive ions. To avoid this situation, a source of electrons is used to control the surface potential. The ionisation of secondary particles and their fragmentation is complicated. It consists of two main steps; sputtering and ionisation. During sputtering the secondary particles are emitted from the surface as an effect of high energy primary impacts. Within the linear cascade model developed by Sigmund [147], the incident particle initiates a cascade of collisions between atoms. Some of the collisions return atoms to the surface, causing the emission of sputtered particles. This process creates mainly neutral species, with a small amount of negative and positive ions. Sputtering leads to surface roughness.

Ionisation can be generated by several different processes, including direct emission of ions, ionisation of neutral clusters, by small ions such as hydrogen,

or ionised species can cause a fragmentation of molecules before they reach the spectrometer.

3.5.1 SIMS measurements - ATOMICA SIMS 4500 Instrument

The SIMS instrument used for this work is the ATOMICA SIMS 4500 instrument with a quadrupole mass analyzer. A schematic of the system is shown in Figure 3.11. The system contains two floating low energy ion guns FLIGs one each for O_2^+ and Cs^+ which are mounted perpendicular to each other on the main analysis chamber. Each ion gun can produce a mono-energetic ion beam in the range of 150 eV to 5 keV. The ion beams are mass filtered by a Wien filter to ensure ion beam purity. The ions produced at source are extracted and directed to the sample via the ion optics. The system also contains a fine focus electron beam gun at the analysis chamber for the purpose of sample charge neutralization that is usually required for non-conducting samples. The secondary ions extracted from the sample are mass analysed using the quadrupole mass analyzer and detected by a channeltron.

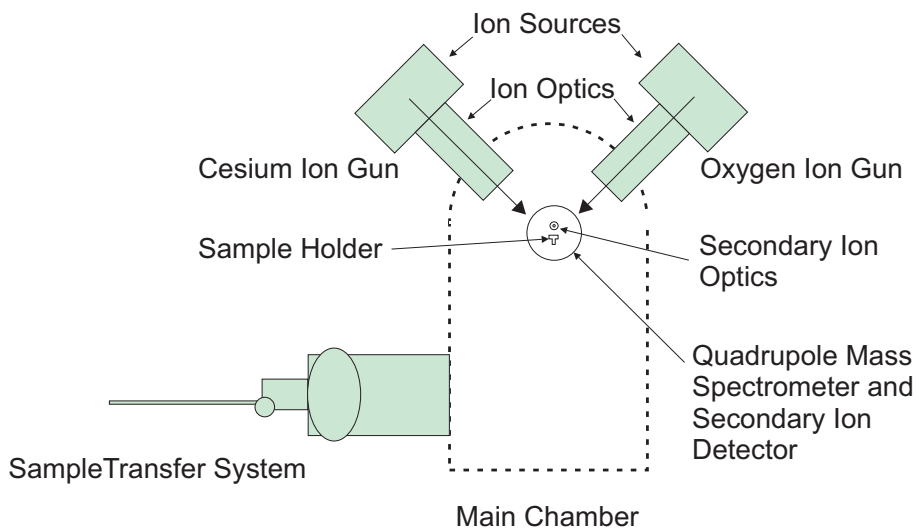


Figure 3.11: Front view of the ATOMICA 4500 system. The system contains two ion guns producing O_2^+ and Cs^+ which are mounted perpendicular to each other, a quadrupole mass analyser and secondary ion detector. The sample holder is inserted into the system using the sample transfer system.

SIMS measurements were performed in ultra high vacuum (UHV) in order to maintain reproducibility and good detection limits especially for species in the residual gas. The base pressure at the main chamber was $\sim 3 \times 10^{-10}$ mbar and it

is obtained by ion pump and titanium sublimation pump. Samples were mounted onto a holder, held down by a spring, and inserted into the system via the load lock which is pumped by turbomolecular pump. Usually the load lock reaches a vacuum of $\sim 6 \times 10^{-6}$ mbar. The main chamber is separated from the load lock by a transfer chamber where there are two stubs for mounting two sample holders. The sample holder is transferred into the main chamber only if acceptable vacuum pressure is reached in the transfer chamber.

Chapter 4

Surface, bulk and interface electronic properties of non-polar InN

4.1 Introduction

Indium nitride (InN) has been the subject of intense research in recent years, largely due to its potential application in optoelectronic devices such as high-efficiency solar cells, light emitting diodes and high-frequency transistors [148]. Despite extensive studies of the many physical properties of InN, there remain limitations for device applications mainly due to an electron accumulation layer present at the InN surface [70, 71]. However, for some applications, such as gas sensors and THz emitters, the presence of an electron accumulation layer is potentially beneficial [148]. Electron accumulation has been observed at the clean surface of wurtzite In- and N-polar *c*-plane and non-polar *a*-plane InN [76], at the non-polar *m*-plane surface of InN nanocolumns [149, 150], as well as at the surface of zinc-blende InN [76]. Based on first-principles calculations, Segev and Van de Walle [82] suggested that the absence of the electron accumulation layer at the reconstructed surface of *a*-plane (11 $\bar{2}$ 0) and *m*-plane (11 $\bar{0}$ 0) InN was due to the absence of In-adlayers. This lack of electron accumulation was demonstrated on *in-situ* cleaved *a*-plane InN by Gwo *et al.* [83], but not observed on as-grown surfaces [76, 83, 149, 151, 152].

One of the main materials development challenges is the control of the free electron density in InN. Currently, the lowest electron carrier density of $2.8 \times 10^{17} \text{ cm}^{-2}$ has been obtained for 4.4 μ thick MBE-grown *c*-plane InN layer [153], however, usually electron densities in polar and non-polar InN films are higher than the mid- 10^{18} cm^{-3} [151, 154–156]. King *et al.* [89] proposed a three-region model for the high *n*-type conductivity and revealed the importance of *n*-type conduction of InN originating from background donors, the surface and interface-related elec-

trons. ‘Bulk’ carriers must come from a uniform distribution of donor defects and/or impurities. They also considered which native defects are responsible for the unintentional *n*-type conductivity exhibited by InN. Due to the lower formation energies of impurities, such as oxygen and hydrogen, compared to native defects, these have been suggested as the dominant donors in InN [84, 157]. However, in some cases, these do not appear to be present in sufficient quantities to account for the total conductivity [50], and hence native defects and dislocations have been suggested as important sources of electrons.

This chapter reports high resolution X-ray photoemission spectroscopy (XPS) and infrared reflectivity measurements of non-polar InN samples grown under both In-rich and N-rich conditions to determine the position of the surface Fermi level and the bulk Fermi level respectively. Using these techniques the surface Fermi level has been found to be lower than previously observed on as grown *c*-plane and *a*-plane InN films. High values of the plasma frequency close to the interface with the GaN buffer layer have also been found, indicating a high electron concentration in this region.

4.2 Experimental details

Non-polar InN thin films were grown under either In- or N-rich conditions by plasma assisted molecular beam epitaxy (PAMBE) at the University of California, Santa Barbara, USA. The *a*-plane ($11\bar{2}0$) and *m*-plane ($1\bar{1}00$) InN films were grown on *a*-plane and *m*-plane free-standing GaN (Mitsubishi Chemical Co.), respectively, with a \sim 50 nm (\sim 20 nm) GaN buffer layer grown under Ga-rich conditions for *a*-plane (*m*-plane) InN [158, 159]. Sample preparation was achieved by wet etching in a 10 mol/l HCl solution for 60 s to reduce the oxide layer. High-resolution XPS measurements were performed on samples of non-polar InN using a Scienta ESCA300 spectrometer at the National Centre for Electron Spectroscopy and Surface analysis (NCESS) at Daresbury Laboratory, UK. Details of the experimental set-up and the monochromated XPS spectrometer are reported in section 3.1.4. The infrared (IR) reflection from non-polar InN samples was measured using a Bruker Vertex

70v Fourier transform infrared spectrometer (FTIR). The reflection spectra were recorded for an incident and reflected angle of 35° to the surface normal. Electrochemical capacitance-voltage (ECV) measurements were performed in 0.1 mol/l solution of potassium hydroxide using a Dage Wafer Profiler CVP21. All measurements were performed at room temperature.

4.3 Results and discussion

IR reflectivity measurements were taken from the non-polar InN films to determine their bulk conduction electron plasma frequency, from which the bulk Fermi level (E_{bF}) position was determined (see section 3.2). Experimental and simulated infrared reflectivity spectra for both *a*-plane and *m*-plane InN are presented in Figure 4.1. The oscillations observed in the experimental spectra are due to Fabry-Pérot interference, corresponding to the total InN film thickness ($d_1 + d_2$, see Figure 4.1). Each IR reflection spectrum was simulated using a two-oscillator dielectric model. To account for the effects of surface roughness, partial coherency of the reflection was applied in the modelling, however, only a small effect was observed. Atomic force microscopy (AFM) measurements were performed to determine the morphology of the surface and the roughness of all non-polar InN samples. The average roughness for *a*-plane and *m*-plane InN samples was 16 nm, and 21 nm, respectively from the $15 \times 15 \mu\text{m}^2$ scans, and these values were used in the simulations. A three layer model consisting of an InN layer, an InN interface layer and bulk GaN was applied to simulate the experimental spectra (Figure 4.1 (a)-(c)). The model does not include a GaN buffer layer since this layer does not change the simulated spectra, its optical properties being the same as for bulk GaN. The high frequency dielectric constant and static dielectric constant for InN (InN interface layer, GaN), $\epsilon(\infty)=7.80$ [160] (6.90, 5.35) and $\epsilon(0)=14.11$ (12.48, 8.90) have been used to simulate the infrared reflectivity spectra. The other parameters used in the simulations are given in Table 4.1. From the plasma frequency, the bulk carrier concentration has been calculated to be $1 - 2 \times 10^{18} \text{ cm}^{-3}$ (Equation 3.7), and the bulk Fermi level position was found to be $\sim 0.70 - 0.75 \text{ eV}$ above the valence band maximum

Table 4.1: Parameters used in the infrared reflectivity simulations, where ω_{TO} , ω_P , τ , $\Delta\omega_P$, d are the longitudinal optical phonon frequency, the plasma frequency, the free-carrier lifetime, plasmon broadening and layer thickness, respectively.

Sample	ω_{TO} (meV)	ω_P (meV)	τ (ps)	$\Delta\omega_P$ (eV)	d (nm)
InN <i>a</i> -plane N-rich	58.2	84±6	0.033±0.004	0.12	950±10
InN interface layer	58.2	300±10	0.010±0.003	0.41	80±10
GaN	70.4	—	—	—	—
InN <i>a</i> -plane In-rich	58.2	85±4	0.075±0.008	0.06	510±10
InN interface layer	58.2	290±10	0.010±0.003	0.41	70±5
GaN	70.4	—	—	—	—
InN <i>m</i> -plane In-rich	58.2	60±10	0.064±0.030	0.06	410±15
InN interface layer	58.2	290±20	0.011±0.003	0.38	60±10
GaN	70.4	—	—	—	—

(VBM) for each non-polar sample.

The VB photoemission for non-polar InN and for previously studied *c*-plane InN [161] is shown in Figure 4.2. The position of the surface Fermi level (E_{sF}) was determined by extrapolating a linear fit to the leading edge of the VB photoemission [162]. It has been found that the E_{sF} for all non-polar cleaned samples is 1.24 ± 0.10 eV. These values of E_{sF} are lower than those previously determined for *c*-plane and *a*-plane InN [76, 152]. Segev and Van de Walle suggested that the microscopic origin of donor-type surface states is In-In bonding within the In-adlayers at the InN surface [81, 82, 163]. This is consistent with core-level XPS measurements of the samples studied in this thesis, which indicate an In-rich surface in each case. The In 3d and N 1s core level XPS spectra have been used to investigate the In-coverage on the clean surface of non-polar InN and thereby determine whether In-adlayers are present on the surface. The core level spectra for In 3d_{5/2}, N 1s and O1s are presented in Figure 4.3.

The In:N XPS intensity ratio has been calculated from the core-level peak areas (divided by the atomic sensitivity factor) for each core level for the Scienta ESCA300 spectrometer. In each case, the In:N ratio is approximately the same for the more surface sensitive (30°) emission and for normal (90°) emission. Using a layer-attenuation model based on photoelectron inelastic mean free paths (IMFPs)

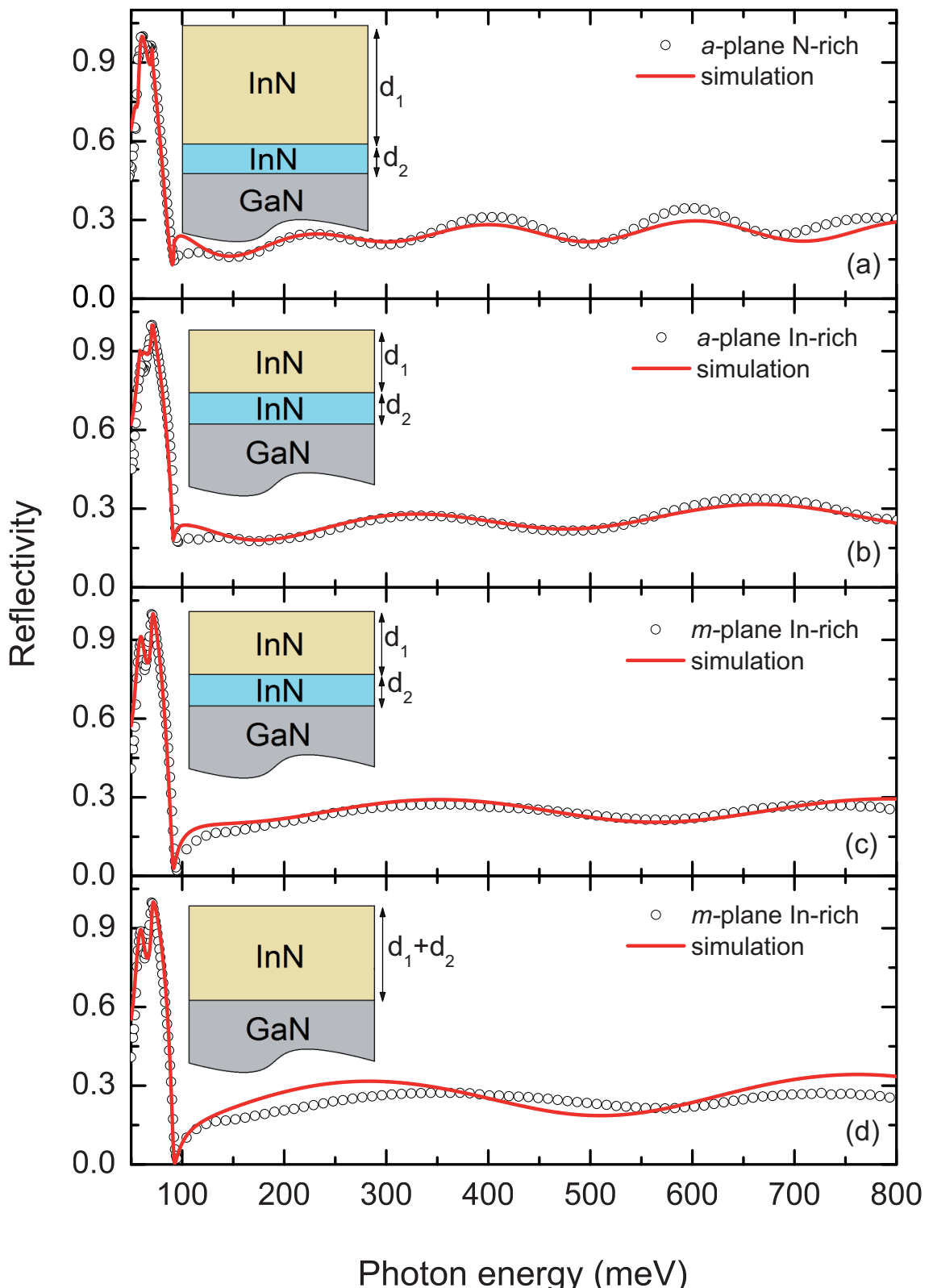


Figure 4.1: Experimental infrared reflectivity spectra for non-polar InN plotted with the simulated spectra. (a) - (c) a three layer model simulations, (d) a two layer model simulation. The insets show the layer models used in infrared reflectivity simulations. In (d), the InN parameters determined for the bulk region in (c) have been used. Further adjustment of these parameters did not result in better agreement with the measured spectrum. The layer thicknesses (d_1 and d_2) are given in Table 4.1.

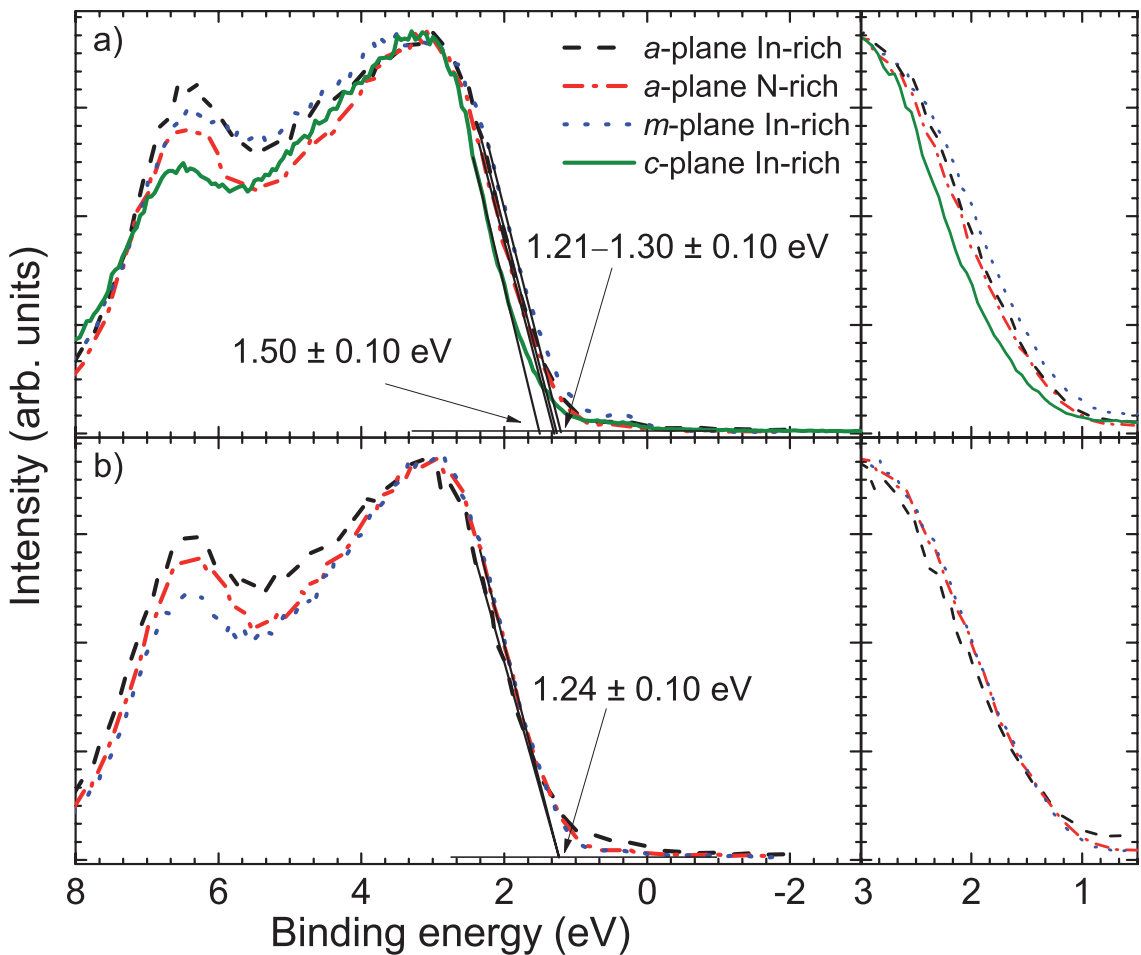


Figure 4.2: Valence band X-ray photoemission of the non-polar *a*- and *m*-plane InN and *c*-plane InN grown under In-rich conditions (solid line). (a) spectra for as-loaded samples, (b) spectra for cleaned samples.

calculated using the TPP-2M predictive formula of Tanuma *et al.* [129], the theoretical XPS In:N ratios for 30° and 90° emission angles are calculated. Comparison of the model calculations with the measured XPS In:N ratios indicate ~1 ML of In above the non-polar InN bulk-like termination in each case. The results of this analysis are presented in Figure 4.4 and the calculated values are significantly lower than found in a previous study of both *a*- and *c*-plane InN (3.0 ML and 3.4 ML, respectively) [164, 165]. It should be noted, however, that some residual oxygen contamination remained following the surface preparation (see Figure 4.3), and one sample (*a*-plane In-rich InN) exhibited some In-droplets, observed by AFM, making detailed quantitative analysis of the adlayer coverage difficult.

Given a fundamental band gap of 0.64 eV for intrinsic InN [53], the surface

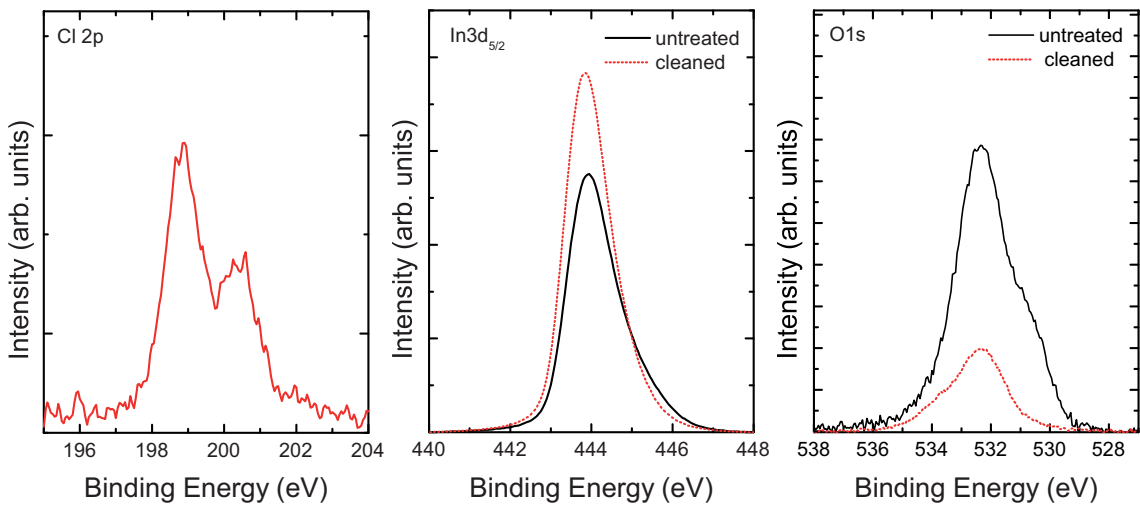


Figure 4.3: Core level spectra recorded for an emission angle 90° from an untreated (black), and HCl-treated (red) *a*-plane InN sample for Cl 2p, In 3d and O 1s.

Table 4.2: Values of the surface Fermi level E_{sF} above the VBM from XPS measurements and bulk Fermi level E_{bF} above the VBM calculated using Fermi-Dirac carrier statistics. The band bending V_{bb} is calculated from the relative surface and bulk Fermi level positions. The bulk carrier concentration is determined from the plasma frequency using a non-parabolic band structure approximation [79]. Poisson-MTFA calculations give the surface state density n_{ss} .

InN	E_{sF} (eV)	E_{bF} (eV)	V_{bb} (eV)	n_b (10^{18}cm^{-3})	n_{ss} (10^{12}cm^{-2})
<i>a</i> -plane N-rich	1.24 ± 0.10	0.75 ± 0.05	0.49	2.3	9.9
<i>a</i> -plane In-rich	1.24 ± 0.10	0.75 ± 0.05	0.49	2.3	9.9
<i>m</i> -plane In-rich	1.24 ± 0.10	0.71 ± 0.05	0.53	1.2	9.7

Fermi level is above the bottom of the conduction band, indicating a downward band bending at the surface of all the non-polar InN samples. The E_{sF} and band bending values are listed in Table 4.2. The surface state densities were determined by solving Poisson's equation within the modified Thomas-Fermi approximation (MTFA). Details of the calculation method are reported in section 2.2. Figure 4.5 shows the band bending and carrier concentration profile for non-polar InN and *c*-plane InN. From Poisson's equation, the surface sheet density can be calculated from the gradient of the band bending potential at the surface. The surface sheet density n_{ss} for non-polar InN films is $\sim 9.9 \times 10^{12} \text{ cm}^{-2}$ and for *c*-plane InN sample is $\sim 14.0 \times 10^{12} \text{ cm}^{-2}$. The electron accumulation for *m*-plane and *a*-plane InN has been found to be lower than for the *c*-plane InN film (Figure 4.5). Whether these

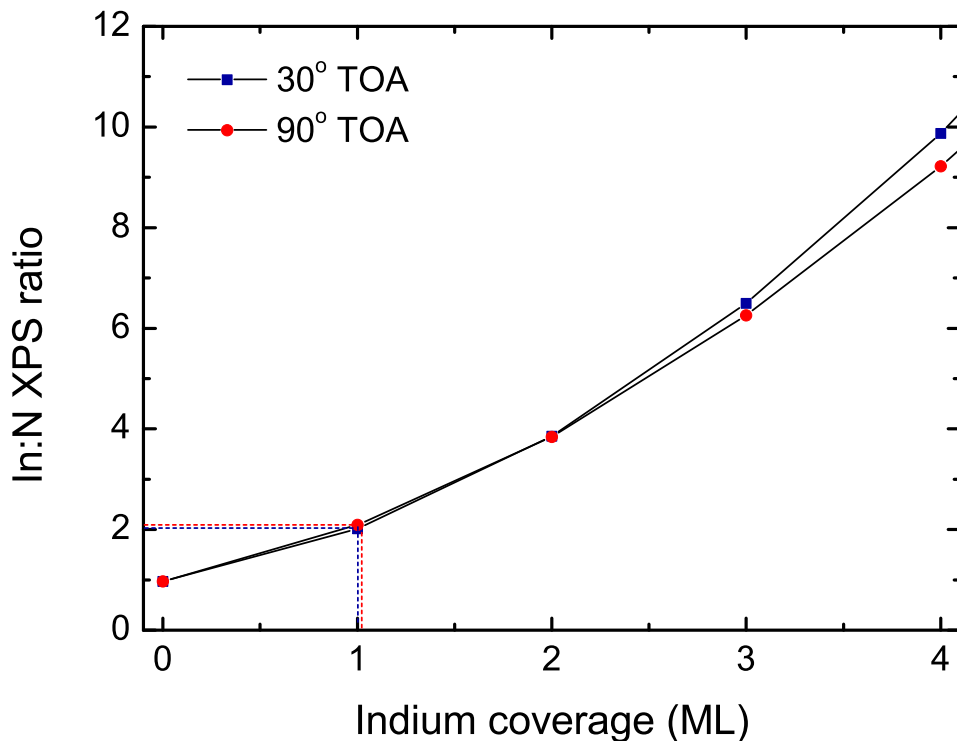


Figure 4.4: XPS In:N intensity ratios for 90° (circles) and 30° (squares) take-off angles (TOA) or emission angles (with respect to the surface plane) calculated for the surface of *a*-plane InN(11̄20) for different surface indium coverages in monolayers.

non-polar samples exhibit the lowest achievable surface Fermi level for undoped non-polar InN is not yet clear. More research involving the correlation of the surface electronic properties of InN with detailed surface structural characterization is required, particularly after different surface preparations. This would verify whether there is a causal link between the presence of In-adlayers and surface electron accumulation and determine whether the latter can be further decreased.

Results of ECV measurements are presented in Figure 4.6. The positive slope and increasing of the experimental Mott-Schottky curves corresponds to the space-charge due to electrons from the surface donors, therefore the electron accumulation model has been used to simulate the C^{-2} vs V curves. The details of the simulations are briefly described in Sections 2.2 and 3.4.1. The parameters obtained from IR reflectivity and XPS have been used in the simulations. Simulated data for all non-polar InN samples are in good agreement with the experimental data. The small discrepancy between the simulated and experimental data of the *a*-plane InN samples results from the higher surface roughness than *m*-plane InN. The roughness

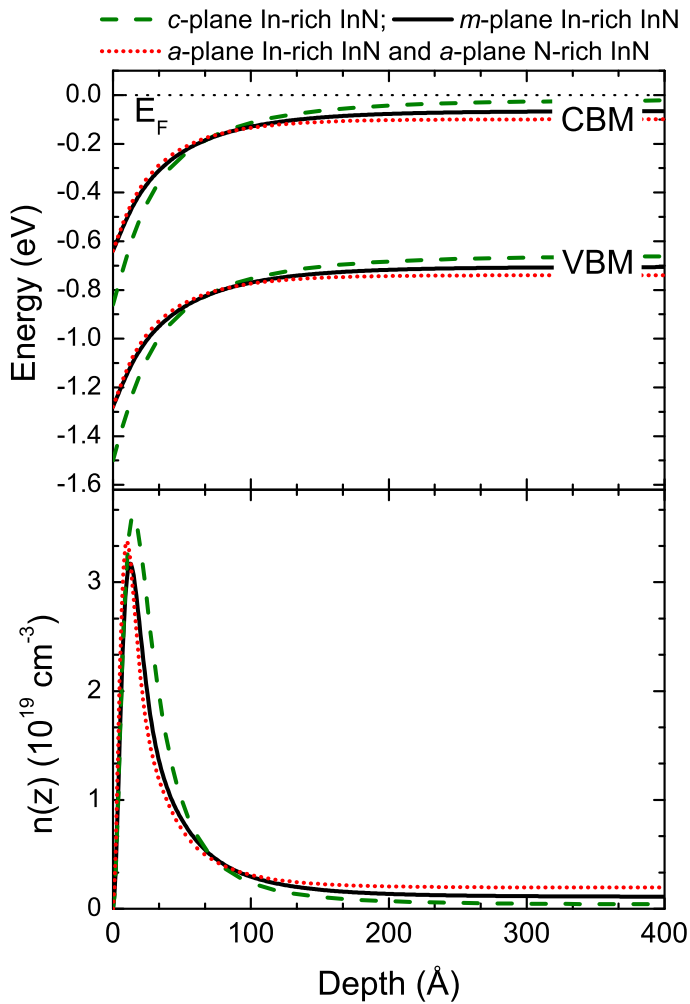


Figure 4.5: The position of the conduction band minimum (CBM) and valence band maximum (VBM) with respect to the Fermi level, E_F , and carrier concentration as a function of depth from the surface for *m*-plane In-rich InN (solid line), *a*-plane In-rich and N-rich InN (dotted line) and *c*-plane In-rich InN (dashed line).

might increase the active area during the experiment, resulting in an increase in magnitude of the capacitance. Hence, the inverted square of capacitance might be lower than for an ideally flat surface. In the simulation presented here the influence of a surface roughness has not been taken into consideration.

As mentioned above, a three layer model for the surface, bulk and interface regions has been applied in the modelling of the IR reflectivity spectra. A model containing just an InN layer and bulk GaN did not produce satisfactory simulated spectra, as shown in Figure 4.1 (d). Including a surface layer to account for the electron accumulation did not make much difference or improve the fit to the simulated

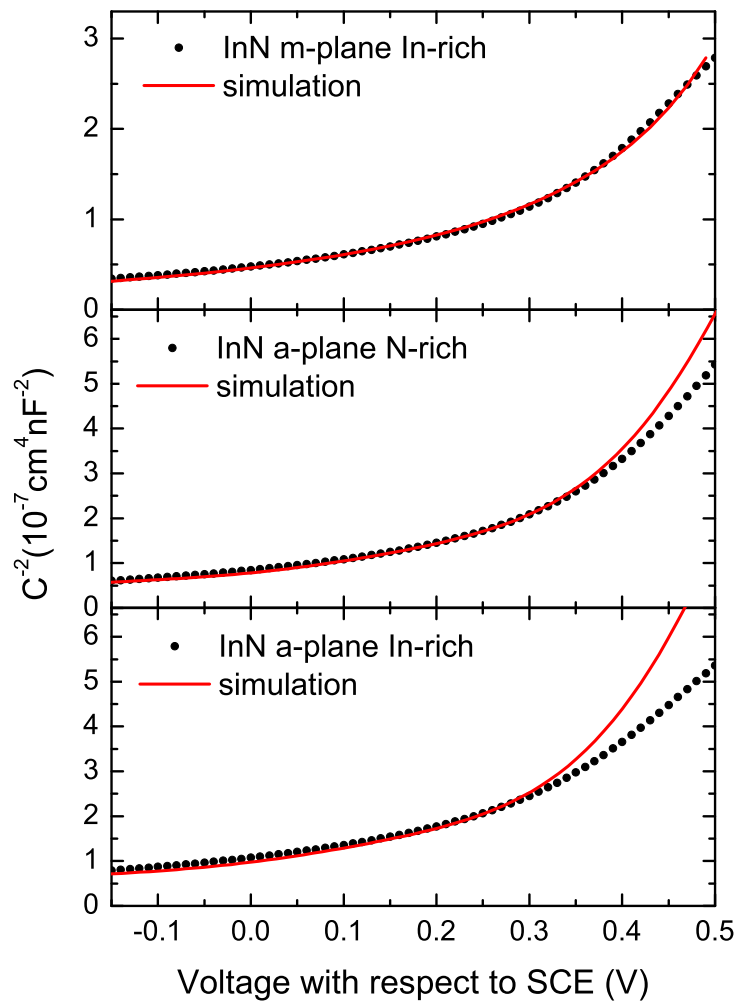


Figure 4.6: Electrolyte capacitance-voltage measurements and simulations on non-polar InN films. In the simulations the electron accumulation model has been used. The small discrepancy between the simulated and experimental data of the a-plane InN samples results from their higher surface roughness than the m-plane InN.

spectra. This is in agreement with previous investigations [166], and simulations with a graded interface [89] which also made negligible differences. The plasma frequencies have been found to be 230–320 meV, corresponding to a sheet carrier concentration of $2.4 – 3.5 \times 10^{14} \text{ cm}^{-2}$ for the interface layer and much higher than previously determined for *c*-plane InN [161]. Several groups have independently discussed the origin of increased electron concentration close to the interface in *c*-plane InN by considering the possible effects from both unintentionally incorporated impurities and threading dislocation densities on the electron transport properties of InN [84, 89, 167–170]. The lower growth temperatures used for the growth of non-polar InN ($380\text{--}450^\circ\text{C}$ [158, 159]) compared with *c*-plane InN ($450\text{--}540^\circ\text{C}$ [84, 153])

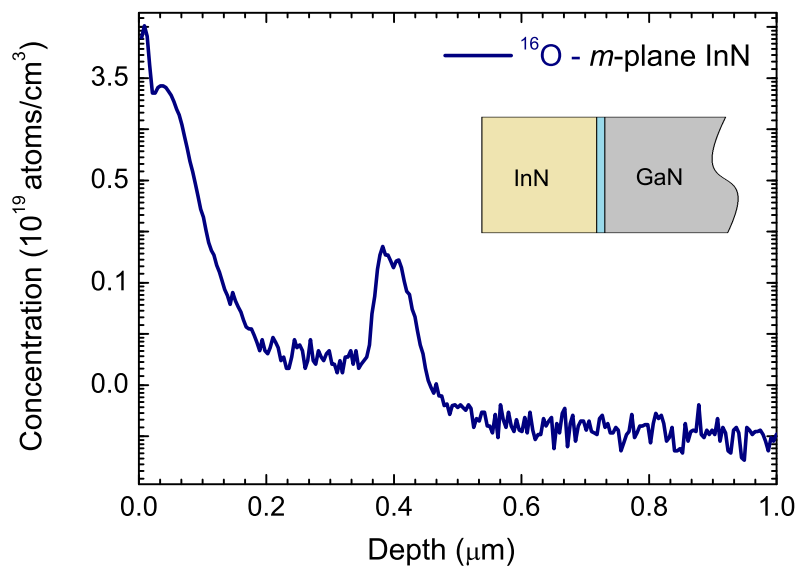


Figure 4.7: SIMS data for m -plane InN, indicating the presence of oxygen impurities in the bulk. The oxygen impurity density increases to $1 \times 10^{18} \text{ cm}^{-3}$ towards the InN/GaN interface, and then rapidly decreases to $5 \times 10^{16} \text{ cm}^{-3}$ in the bulk GaN.

are likely to increase the impurity incorporation, increasing the density of donors close to the interface and resulting in high plasma frequency values. This was confirmed by SIMS (see Figure 4.7) indicating that for m -plane InN the oxygen impurity density was approximately constant at $1 \times 10^{17} \text{ cm}^{-3}$ in the bulk InN and increased to $1 \times 10^{18} \text{ cm}^{-3}$ towards the InN/GaN interface, and then rapidly decreased to $5 \times 10^{16} \text{ cm}^{-3}$ in the bulk GaN. Moreover, Koblmüller *et al.* [158, 159] have studied the structural properties of non-polar InN and found that basal-plane stacking faults, where defects and/or impurities could be localized, contributed significantly to the interface-related carrier concentration.

4.4 Conclusions

In this chapter it has been demonstrated that the film quality of both a -plane and m -plane non-polar InN has significantly improved, as indicated by the lower value of bulk carrier concentration than reported previously for many non-polar InN films [151, 156]. A high carrier concentration has been found in the non-polar InN close to the interface with the GaN buffer layer, that may be due to donors associated with unintentionally incorporated impurities, potentially localized at basal-plane stacking faults. The surface Fermi level for all non-polar InN samples has been found

to be lower than previously observed on non-cleaved InN samples. The observation of an electron accumulation layer in the presence of a single In-adlayer is consistent with previous theoretical predictions. Additionally, the results presented in this chapter very well correspond to the three-region model proposed by King *et al.* [89]. The model shown in Figure 4.8 is characterised by three contributions - I: donors due to dislocations, whose density falls exponentially away from the interface; II: the background ‘bulk’ density resulting from defects or impurities uniformly distributed throughout the film; III: surface electron accumulation.

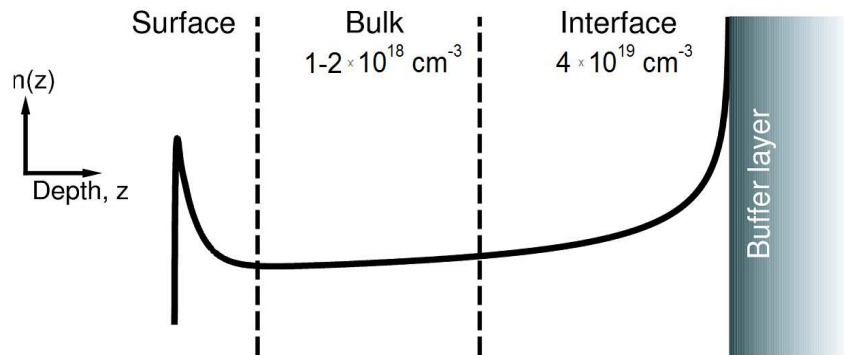


Figure 4.8: Schematic representation of the three-region model [89].

Electrochemical capacitance-voltage technique, combined with ECV modelling is complementary to IR reflectivity and XPS to investigate the electronic properties of InN surface. The surface quality plays a significant role in ECV modelling. Smaller values of surface roughness result in a smaller discrepancy between simulated and experimental data.

Chapter 5

Giant reduction of InN surface electron accumulation: Compensation of surface donors by Mg dopants

5.1 Introduction

A very important attribute of semiconductors is the possibility of changing the type of conductivity, and this is particularly useful in the fabrication of *p-n* junctions, the basic building block of all electronic devices.. The change of type of conductivity is typically achieved by the incorporation of a suitable dopant element inside the bulk of the semiconductor which can act as a donor producing *n*-type conductivity or act as an acceptor producing *p*-type conductivity.

While intrinsic InN is clearly *n*-type and Si-doping further increases the *n*-type character (King *et al.* [66]), the reproducibility and control of *p*-type doping in InN and In-rich III-N alloys, essential for the realisation of many of the potential optoelectronic device applications, remains a controversial issue. Following the first reported result of *p*-type bulk conductivity by Mg-doping [26], there has been intense study in this area [28, 103, 171–183]. A particularly problematic issue is the accumulation layer that is present at the surface of InN. This causes an inversion layer to form at the surface of a *p*-type material, where the *p*-type bulk is separated from the surface *n*-type region by a depletion layer. Therefore, measurements such as single-field Hall effect are dominated by the surface electron layer and cannot be used to determine the bulk conductivity. Nevertheless, there are experimental techniques that have confirmed *p*-type bulk conductivity in InN. For instance the variable-field Hall effect [103] and thermopower measurements [177, 184] give clear evidence of free holes in InN, but without depth resolution. Another useful tech-

nique is electrochemical capacitance-voltage profiling (ECV), however, ECV yields information only on the presence of ionised acceptors, rather than the density of free holes. Furthermore, there are reports suggesting that the reduction of the electron accumulation layer in InN by chemical treatment [106, 107] is also possible. However, there have been no reports of the removal or of any significant reduction of the electron accumulation as a result Mg-doping.

In this chapter, high-resolution X-ray photoemission spectroscopy (XPS) is used to investigate electron accumulation at the cleaned wurtzite c-plane In-polar surface of Mg-doped InN. Using this technique, a significant lowering of the surface Fermi level has been observed with increasing Mg concentration, indicating a highly desirable reduction of the electron accumulation. To examine the band bending and carrier concentration profile as a function of depth below the surface, Poissons equation is solved within a modified Thomas-Fermi approximation (MTFA).

5.1.1 Si-doped InN - previous results

Before the appropriate results are presented, it is necessary to mention *n*-type Si-doped InN. The effects of Si-doping on the position of the surface Fermi level and the bulk Fermi level in InN has been investigated by King *et al.* [66, 185]. Incorporation of Si into InN during the growth increases the carrier concentration in InN indicating that Si is electrically active and acts as a donor.

The surface Fermi level for InN is located below the charge neutrality level (CNL), hence some donor surface states are unoccupied and therefore positively charged. As a consequence of this, the surface charge must be balanced by the near-surface electron accumulation layer which is caused by downward band bending [71]. The situation for extreme downward band bending is presented schematically in Figure 5.1 (a). As the bulk Fermi level increases, the amount of downward band bending decreases. The surface Fermi level must move towards the CNL to maintain charge neutrality. As a consequence, some of the unoccupied donor surface states become occupied (Figure 5.1 (b)). Finally, the bulk and surface Fermi levels approach the CNL where charge neutrality is maintained, leading to zero space-

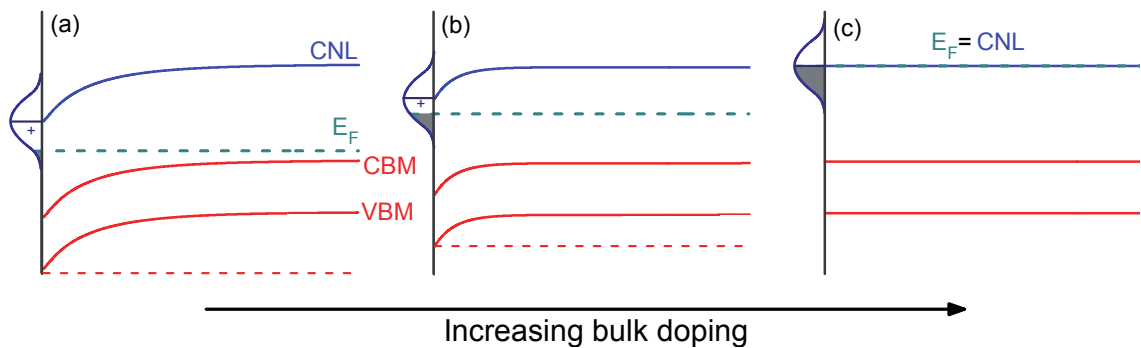


Figure 5.1: Schematic representation of the decrease in downward band bending, corresponding reduction in unoccupied surface state density as the Fermi level moves closer to the CNL at the surface, and stabilization of the bulk and surface Fermi levels at the CNL with increasing doping ((a) to (c)) in InN. This figure is taken from [185].

charge, no band bending and zero surface charge (Figure 5.1 (c)).

5.2 Experimental details

Mg-doped InN samples were grown by plasma-assisted molecular beam epitaxy (PAMBE) with a range of Mg cell temperatures at the University of Canterbury. All 1200 nm thick films were grown on *c*-plane sapphire substrate with a 3000 - 4000 nm GaN buffer layer, provided by Lumilog. The Mg concentration has been determined by SIMS using an Atomika 4500 SIMS instrument (Chapter 3.5.1) with a 500 eV O_2^+ ion beam. The Mg concentration has been calibrated from the Mg-SIMS profile of an undoped InN sample implanted with Mg_{25} to a dose of $1 \times 10^{14} \text{ cm}^{-2}$. The natural isotope abundances were used to determine the total Mg-concentration in the InN:Mg samples. High-resolution XPS measurements were performed at room temperature using a monochromated Al $K\alpha$ x-ray source and a Scienta ESCA300 spectrometer at the NCESS facility. Details of the spectrometer and its geometric arrangement are described in section 3.1.4. The Fermi level was calibrated from the Fermi edge of an ion-bombarded silver reference sample. For as-loaded samples, native oxide was observed on the surface of Mg-doped InN. The samples were then subjected to etching in a 10 mol/l HCl solution for 60 s to reduce the oxide layers, followed by rinsing in deionised water and immediately being blown dry with N_2 before loading into the vacuum chamber. Survey spectra from as loaded and cleaned Mg-doped InN identifying the elements present in the near surface region are shown

in 5.2.

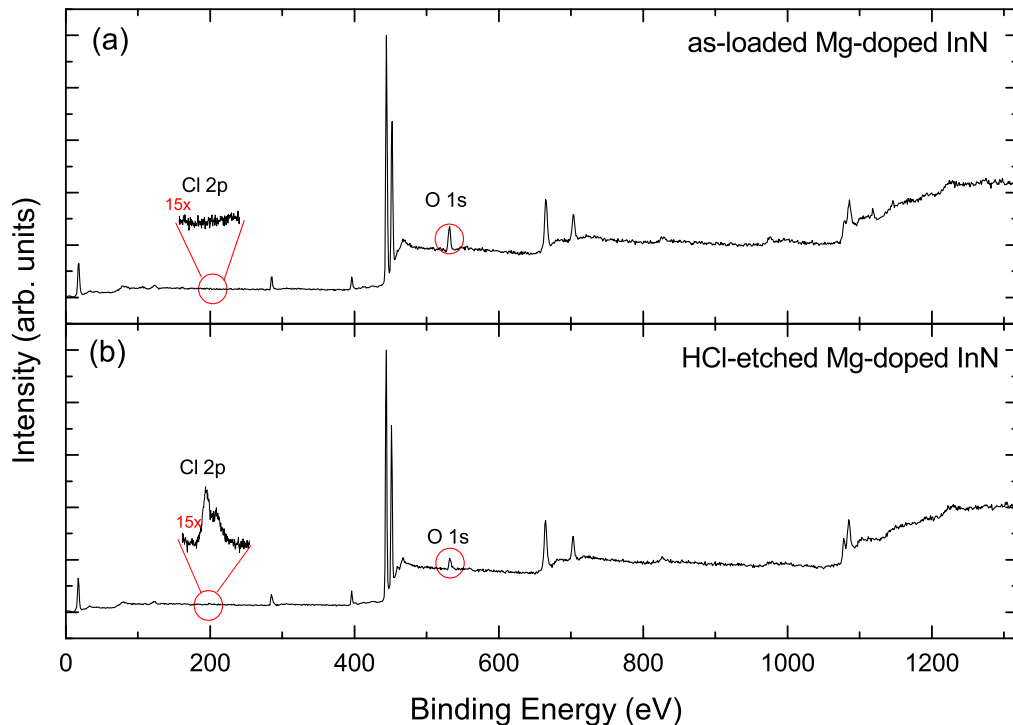


Figure 5.2: XPS wide energy scan from heavily doped Mg-doped InN ($h\nu = 1486.6$ eV) for (a) as-loaded film and (b) cleaned film.

5.3 Transition from electron accumulation layer to hole depletion layer by Mg-doping

5.3.1 Results and analysis

SIMS was initially employed to determine the Mg concentration in the InN samples and the profiles of four Mg-doped InN samples are shown in Figure 5.3. In each case, the fall-off observed in the Mg-signal coincided with a large increase in Ga-signal (i.e. profiling through the InN:Mg layer and into the GaN buffer layer). Apart from in the surface transient region at the start of the SIMS measurements, a rather uniform [Mg] signal is observed for each sample throughout the depth of the InN:Mg films. From these SIMS measurements, the Mg concentration ([Mg]) is estimated to be 1.2×10^{20} cm $^{-3}$, 5.0×10^{19} cm $^{-3}$, 1.9×10^{19} cm $^{-3}$ and 4.7×10^{18} cm $^{-3}$.

XPS measurements were performed on all the samples to determine the position of the Fermi level at the surface as a function of bulk carrier concentration.

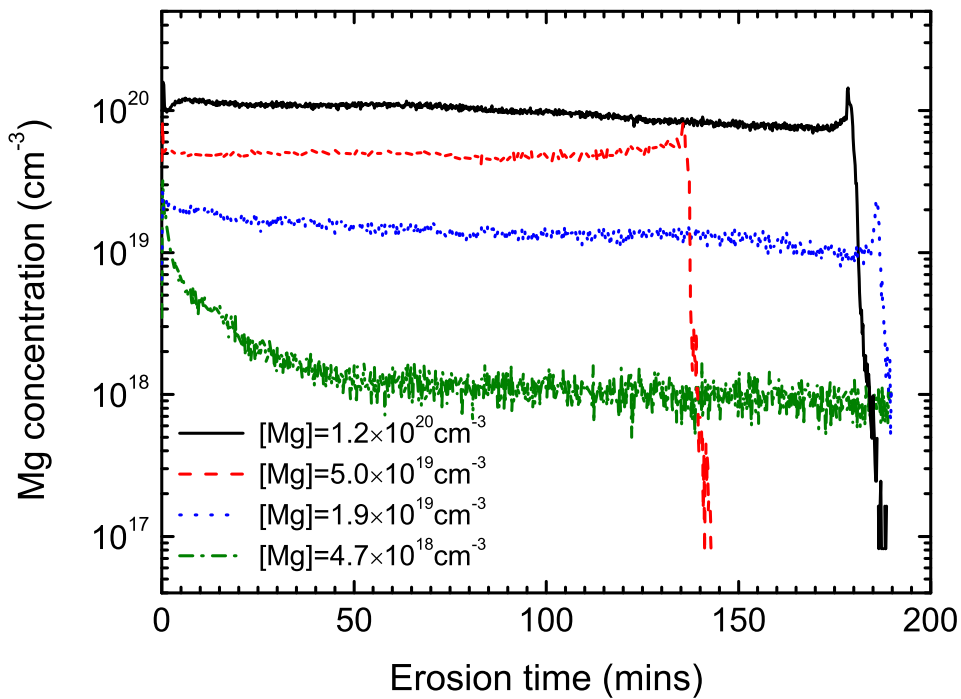


Figure 5.3: SIMS profiles of Mg for four InN:Mg films. In each case, the fall-off observed in the Mg-signal coincided with a large increase in Ga-signal (i.e. profiling through the InN:Mg layer and into the GaN buffer layer). The Mg concentrations have been calibrated from the Mg-SIMS profile of an undoped InN sample implanted with Mg₂₅ to a dose of $1 \times 10^{14} \text{ cm}^{-2}$.

The leading edges of the valence band photoemission spectra for high Mg-doped InN samples are shown in Figure 5.4(a). Again, the surface Fermi level is obtained by linear extrapolation of the valence band photoemission leading edge to the baseline in order to take account of the finite resolution of the spectrometer [162]. The values determined in this way are presented in Figure 5.4(b). For moderate Mg concentrations ($< 1 \times 10^{19} \text{ cm}^{-3}$) the Fermi level is pinned at the surface at $\sim 1.3 - 1.4$ eV above the valence band maximum (VBM), indicating a large electron accumulation near the surface. These values were previously observed for undoped InN films [38, 77, 161]. The surface Fermi level positions for high Mg concentrations ($> 1 \times 10^{19} \text{ cm}^{-3}$) monotonically decrease with increasing Mg density, indicating a reduction of the electron concentration in the accumulation layer. The lowest value of the surface Fermi level of 0.83 eV has been observed for $[\text{Mg}] = 1.2 \times 10^{20} \text{ cm}^{-3}$.

The In:N XPS intensity ratios are calculated from the core level peak areas divided by the atomic sensitivity factors for each core levels for the Scienta300

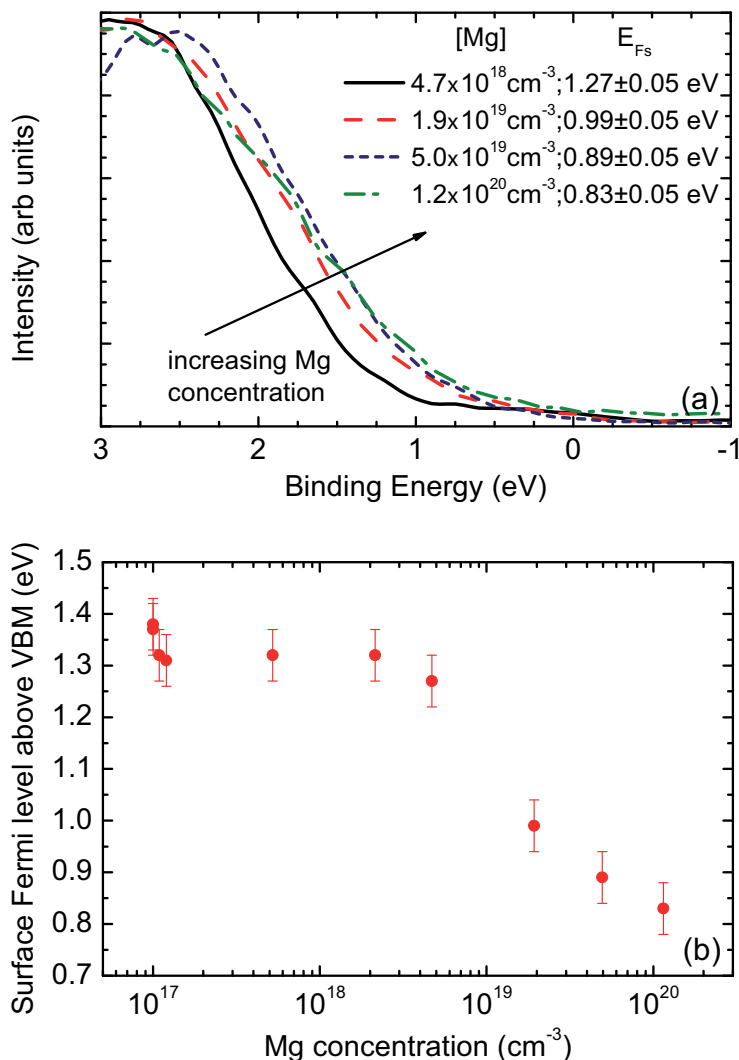


Figure 5.4: (a) Valence band photoemission spectra of Mg-doped InN for different Mg concentrations and (b) corresponding VBM to surface Fermi level separation, determined by linear extrapolation of the valence band edge to the baseline.

spectrometer. A correlation between the surface In:N ratio, the Mg concentration and the surface Fermi level can be observed and it is shown in Figure 5.5. The In:N ratio decreases as Mg concentration increases, and this lowering indicates a reduction of the In-adlayers at the surfaces. It should be noted, however, that some residual oxygen contamination remained following the surface preparation, making detailed quantitative analysis of the adlayer coverage difficult.

The band bending and carrier concentration profiles as a function of depth from the surface were evaluated by numerically solving Poisson's equation within a MTFA and this is shown in Figure 5.6. The details of these calculations are briefly

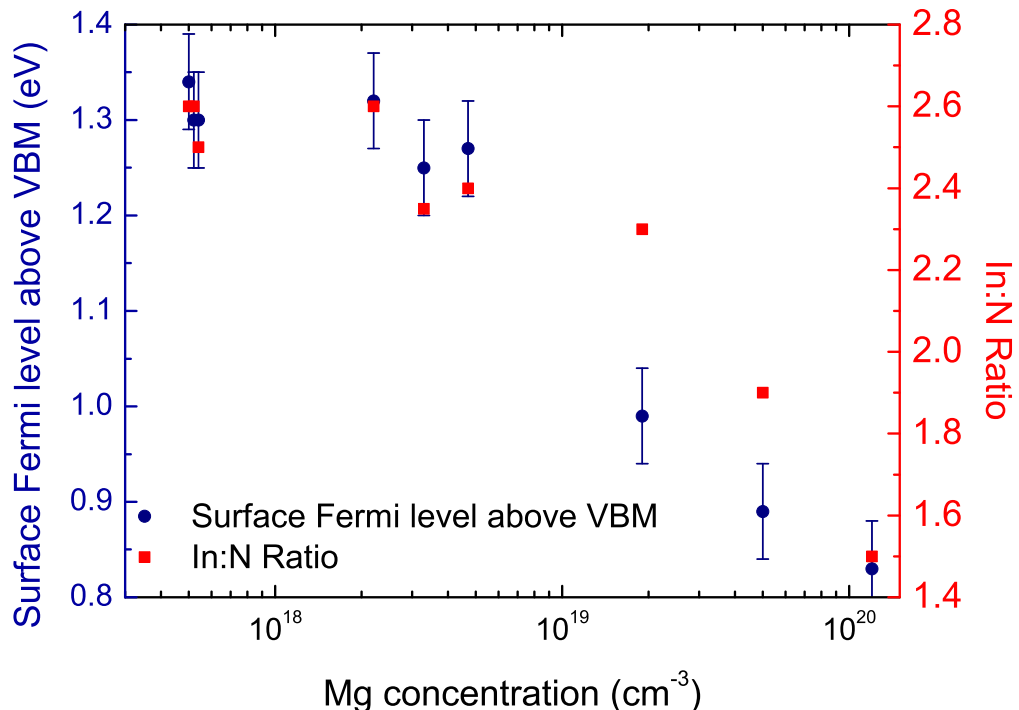


Figure 5.5: The surface Fermi level positions (circles) and In:N XPS ratios (squares) as a functions of Mg concentration. The In:N XPS intensity ratios have been determined from the core-level peak areas (divided by the atomic sensitivity factor) for each core level for the Scienta ESCA300 spectrometer.

described in section 2.2. Each profile is simulated using an inversion layer model, assuming that all the Mg atoms act as acceptors and the hole effective mass is $0.65m_e$ [182]. From Poisson's equation (Equation 2.32), the surface state density n_{SS} can be calculated from the gradient of the band bending potential at the surface, while the electron sheet density (n_{2D}), can be found from the area under the electron accumulation peak in the carrier concentration distribution. The electron sheet density drastically decreases for the samples with high Mg concentration indicating a severe reduction of the electron accumulation (see Figure 5.7). This situation can be seen as the vanishing of the electron accumulation peak in Figure 5.6 (d-f). The n_{2D} for the samples with the highest Mg concentration has been found to be $7.9 \times 10^7 \text{ cm}^{-2} - 2.5 \times 10^{10} \text{ cm}^{-2}$, much lower than for undoped InN [77]. While for moderately Mg doped InN films the n_{2D} is similar to undoped InN and the concentration has been determined to be $\sim 1.0 \times 10^{13} \text{ cm}^{-2}$. The values determined by space charge calculations are presented in Table 5.1.

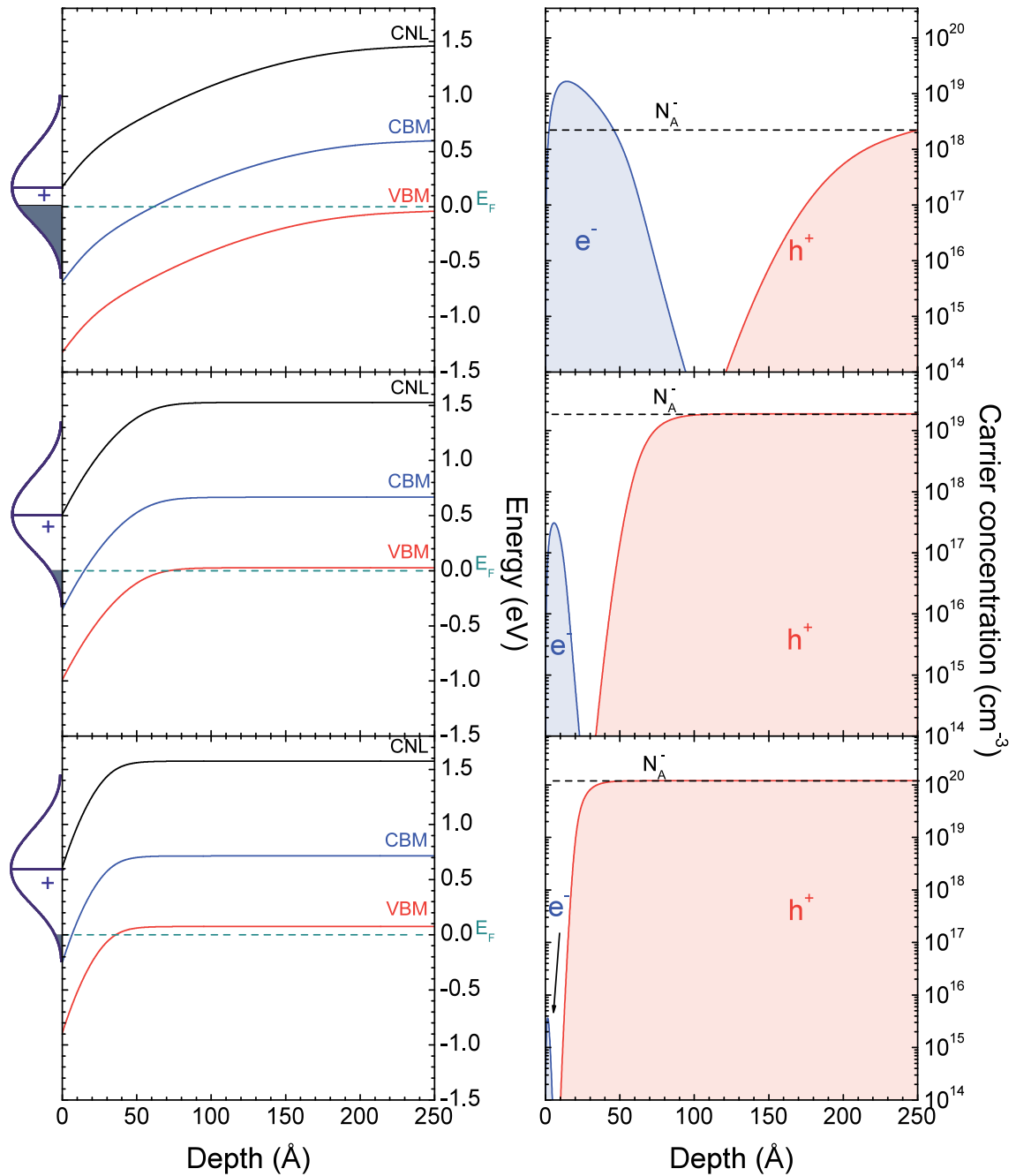


Figure 5.6: The conduction band minimum, valence band maximum and charge neutrality level with respect to the Fermi level (a-c) and the carrier concentration profile, as a function of depth from the surface, for a Mg concentration of (a)(d) $4.7 \times 10^{18} \text{ cm}^{-3}$, (b) (e) $1.9 \times 10^{19} \text{ cm}^{-3}$ and (c) (f) $1.2 \times 10^{20} \text{ cm}^{-3}$. The CNL is located high above the CBM. The shaded portion in each case represents filled donor states. Each profile was simulated using a inversion layer model, assuming that all Mg atoms act as acceptors and a hole effective mass of $0.65m_e$.

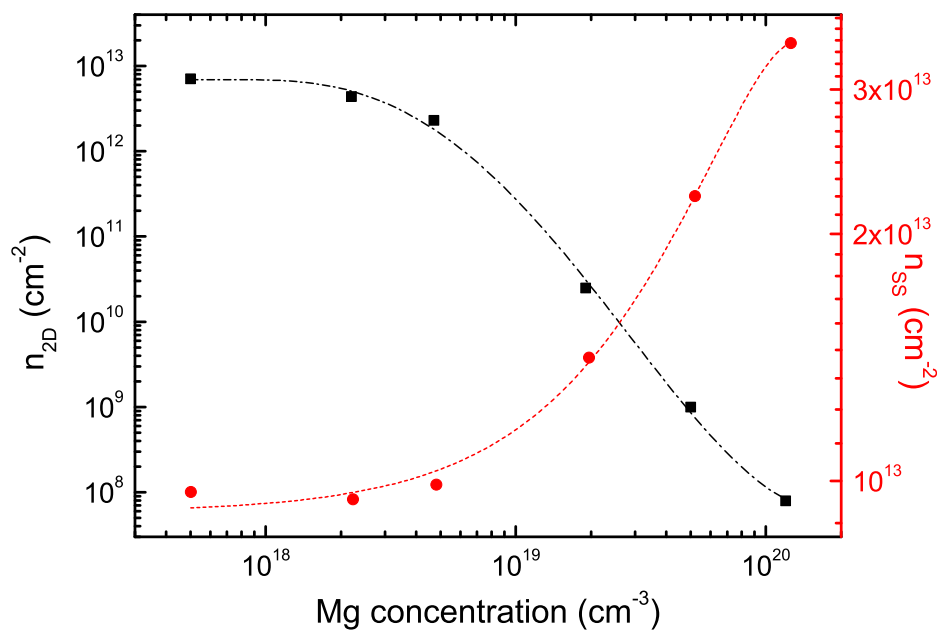


Figure 5.7: Surface electron sheet density (n_{2D}) (circles) and donor surface state density (n_{ss}) (squares) as a function of Mg concentration, with fits shown to guide the eye. The value of (n_{2D}) drastically decreases for the samples with high Mg concentration indicating a significant reduction of the electron accumulation.

5.3.2 Discussion

If the surface Fermi level is located below the CNL, some donor surface states will be unoccupied and hence positively charged. Incorporation of Mg into InN shifts the Fermi level at the surface towards the valence band maximum (VBM) and unoccupies some previously occupied donor surface states. Consequently, the positively charged surface donor density increases and it could be expected to result in huge accumulation layer. However, in contrast to undoped or n -type doped InN, the electron sheet density (accumulation layer) decreases significantly (Figure 5.7) as the Mg concentration increases. The surface in an equilibrium state must be neutral, therefore the positive surface charge must be balanced - this can be understood within the inversion layer model. The width of the depletion region decreases with increasing Mg content, therefore the near-surface Mg acceptors, N_A^- , can compensate the positively charged surface donor states, reducing the electron accumulation. For the highest Mg concentration, the accumulation layer is dramatically reduced, therefore the sample essentially exhibits a hole depletion layer (Figure 5.6 (c) and (f)).

Table 5.1: Values of the surface Fermi level E_{sF} above the VBM from XPS measurements and bulk Fermi level E_{bF} above the VBM calculated using Fermi-Dirac carrier statistics. The band bending V_{bb} is calculated from the relative surface and bulk Fermi level positions. Poisson-MTFA calculations give the surface state density n_{SS} and electron sheet density n_{2D} .

[Mg] (cm ⁻³)	E_{sF} (eV)	E_{bF} (eV)	V_{bb} (eV)	n_{SS} cm ⁻²)	n_{2D} cm ⁻²)
1.2×10^{20}	0.83 ± 0.05	-0.15	0.98	3.4×10^{13}	7.9×10^7
5.0×10^{19}	0.89 ± 0.05	-0.08	0.97	2.3×10^{13}	1.1×10^9
1.9×10^{19}	0.99 ± 0.05	-0.03	1.02	1.4×10^{13}	2.5×10^{10}
4.7×10^{18}	1.27 ± 0.05	0.02	1.25	9.9×10^{12}	2.3×10^{12}
2.2×10^{18}	1.32 ± 0.05	0.04	1.28	9.5×10^{12}	4.4×10^{12}
5.0×10^{17}	1.37 ± 0.05	0.08	1.29	9.7×10^{12}	7.1×10^{12}

As mentioned in Chapter 4, Segev and Van de Walle suggested that the microscopic origin of the occupied donor-type surface states is In-In bonding in In adlayers whereas the unoccupied donor surface states are associated with In dangling bonds without any In-adlayers at the InN surface [81, 82, 163]. Their theoretical results are presented in Figure 5.8 (a), where the donor surface states are located below the CNL in the virtual gap (ViG). The results achieved from our XPS measurements and space charge calculations are in good agreement with these theoretical results. The histogram of surface state densities of Mg-doped and Si-doped InN and the bulk density of states calculated numerically using quasiparticle-corrected density-functional theory (QPC-DFT) are presented in Figure 5.8 (b). This histogram is created as a difference between the surface state densities in a particular range of energy and then divided by the length of the energy range. The energy position of the donor surface states corresponds reasonably well to the theoretical surface states associated with In-In bonding in an In-adlayer, confirming the validity of Segev and Van de Walle’s theory. Moreover, these results correspond quite well to the results from core level XPS data. As shown in Figure 5.5, the In:N ratio decreases when the Mg concentration increases. The lowering of In:N ratio indicates a reduction of the In-adlayer at the surfaces, hence a reduction in the surface electron accumulation layer. The presence of a high concentration of Mg might induce changes in the surface reconstruction, making the indium adlayer reconstruction less favourable, and

hence reducing the position of the surface Fermi level. This situation is complicated and these suggestions are rather speculative, because some residual oxygen contamination remained following the surface preparation, making detailed quantitative analysis of the adlayer coverage rather difficult.

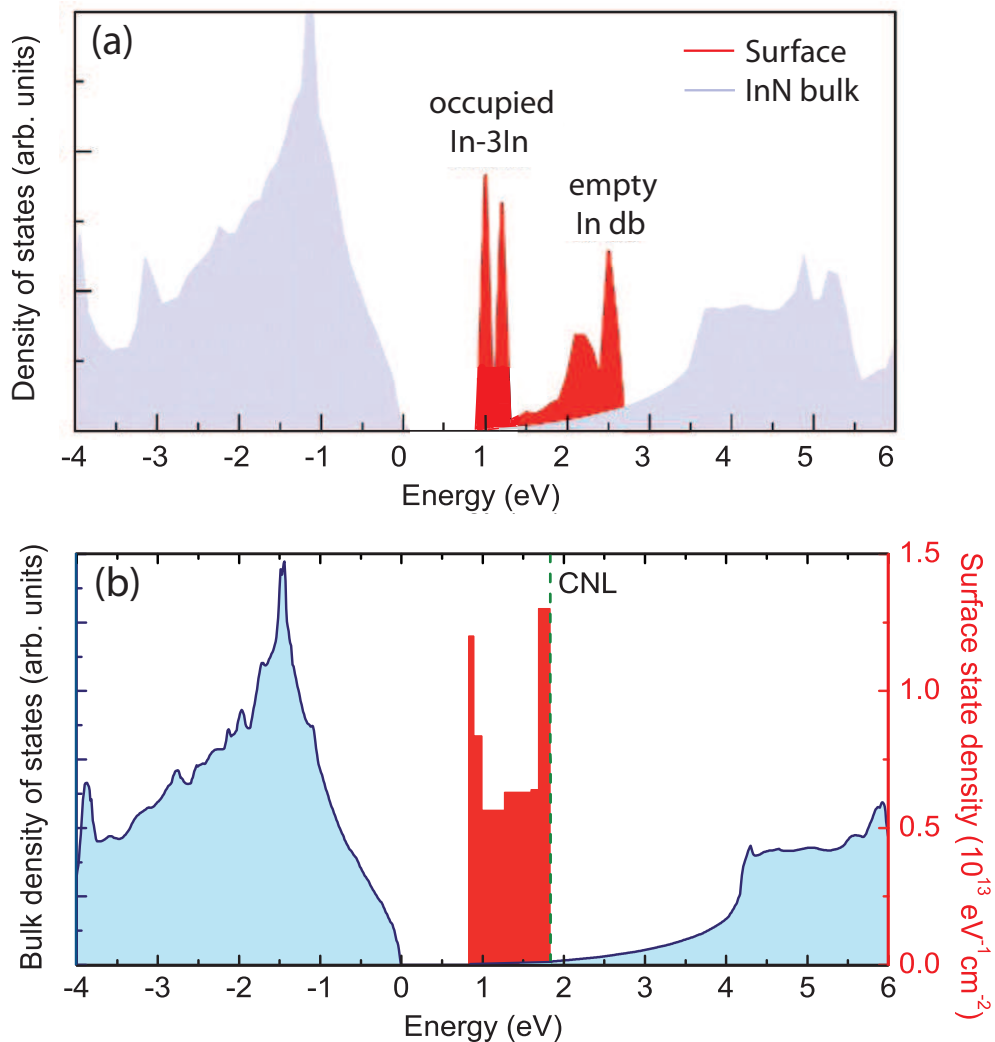


Figure 5.8: (a) Density of states (DOS) for the polar (0001) InN, calculated by Segev *et al.* [80] using density-functional theory (DFT) within the local density approximation (LDA). (b) Surface state density (red histogram) evaluated by numerically solving Poisson's equation within MTFA and bulk DOS (blue line) for the (0001) InN calculated by F. Bechstedt's group [148], using quasiparticle-corrected density-functional theory (QPC-DFT).

Incorporation of Mg into InN during growth should change the electronic properties of this material, switching the type of bulk conductivity from *n*-type to *p*-type. One might ask a question if *p*-type conductivity in high Mg-doped InN can

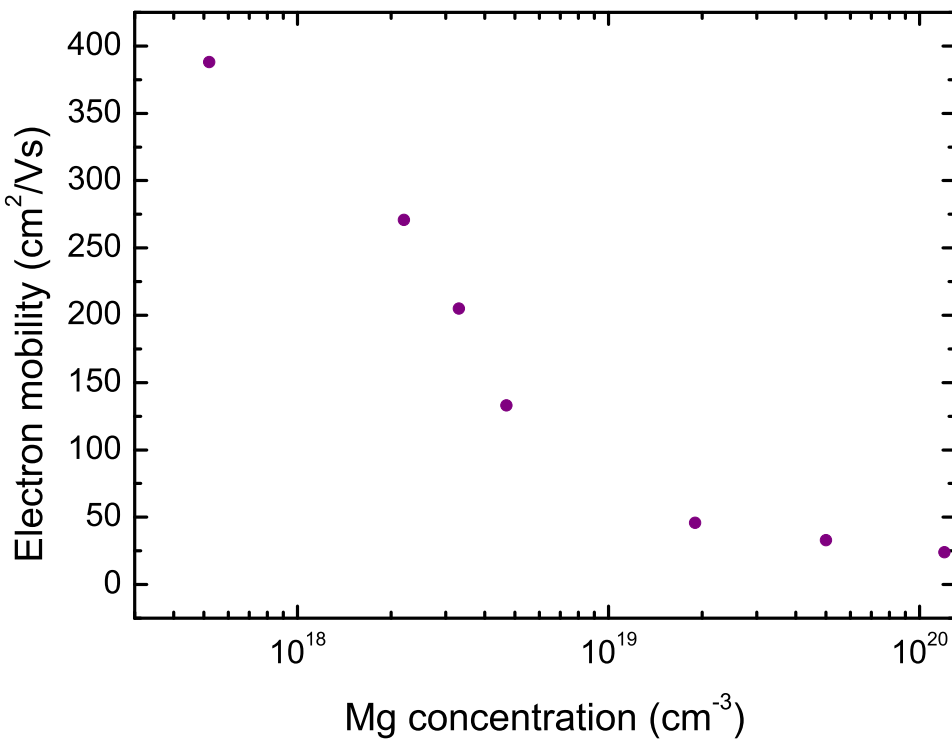


Figure 5.9: Comparison of the electron mobility measured by the Hall effect for Mg-doped InN. The mobilities of highly Mg-doped InN samples are roughly one magnitude lower than those of moderately Mg-doped InN.

be determined by Hall effect measurements due to extremely low electron accumulation near the surface? Unfortunately, the sign of the Hall coefficient suggests that the films are still *n*-type and even a low density electron accumulation layer will dominate the measurements. However, the measured mobilities are in the range of 24 to 50 cm^2/Vs . As shown in Figure 5.9, the corresponding electron mobility values in these samples are roughly one magnitude lower than those of moderately Mg-doped InN or undoped InN. This behaviour has been observed previously [88]. The significant decrease in mobility observed for heavily Mg-doped layers and the negative Hall coefficient might be the result of a much higher hole effective mass. Similarly to Zn-doped InAs [186] the large mobility of electrons compared to that of holes will result in a dominant contribution of electrons to the Hall effect, even in cases where electrons are minority carriers in the bulk of the layer.

An indication of the existence of active Mg acceptors and hence the possibility of *p*-type conductivity, is given by ECV measurements. The Mott-Schottky curves are presented in Figure 5.10. The slope of the reciprocal square capacitance changes

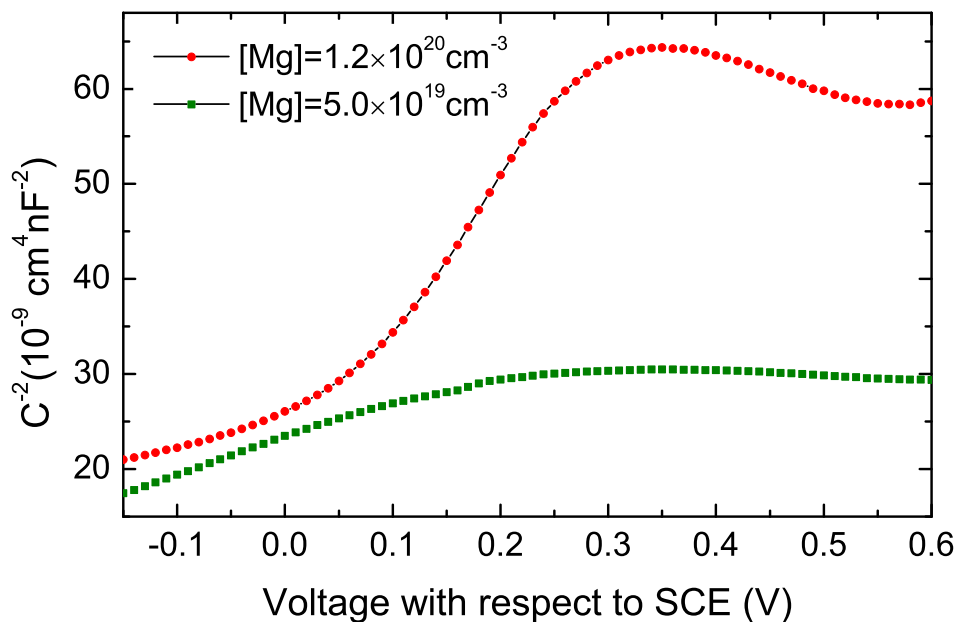


Figure 5.10: Electrolyte capacitance-voltage measurements on Mg-doped InN films. The slope of the Mott-Schottky curves changes from positive to negative for the heavily Mg-doped samples, indicating that a p-type bulk layer is buried beneath a n-type surface layer.

the from positive to negative for the heavily Mg-doped samples, indicating that a p-type bulk layer is buried beneath a n-type surface layer.

Figure 5.11 shows the position of the surface Fermi level as a function of carrier concentration for n-type and p-type InN, where it has been assumed that the hole concentration is equal to the Mg acceptor density. Within this assumption, the value of $\sim 1 \times 10^{19} \text{ cm}^{-3}$ is the cross-over point above which the surface Fermi level of n-type InN tends to increase to reduce the electron accumulation, producing flat bands and maintain charge neutrality. In the case of p-type InN the surface Fermi level tends to decrease to reduce the electron accumulation, producing a hole depletion layer and maintaining charge neutrality. Similar divergence of the surface Fermi level position with doping was previously observed for n- and p-type GaAs, the archetypal compound semiconductor [187]. However, rather than the surface states responsible for the space charge always being donors as in the InN case, for GaAs, the type of charged surface state changes from acceptors in n-type to donors in p-type GaAs. Equivalently, downward band bending is observed for InN for both n- and p-type doping, whereas upward band bending is present for n-type GaAs

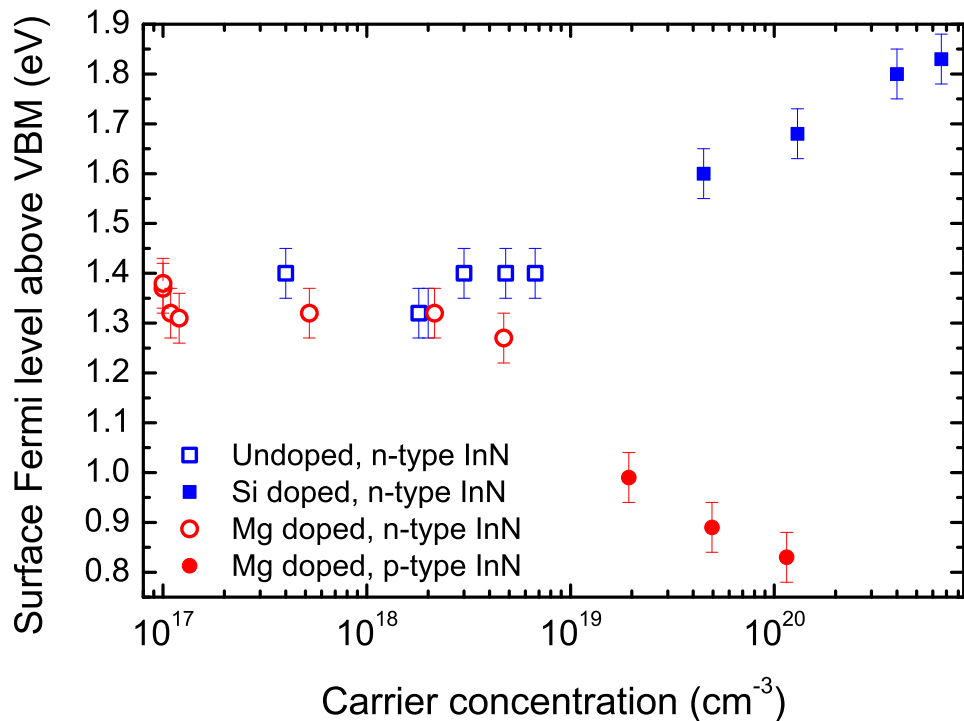


Figure 5.11: Surface Fermi level position of *n*-type (squares) and *p*-type (circles) InN as a function of carrier concentration.

and downward for *p*-type. This difference is due to the respective CNL positions in these two materials, with InN's being above the conduction band minimum [66] and that of GaAs just below the middle of the fundamental band gap [188, 189].

5.4 Conclusions

The results presented in this chapter demonstrate that the incorporation of Mg as a dopant into InN crucially changes the bulk and surface electronic properties of this material. Previous results have shown that Si acts as a donor and its incorporation increases the bulk electron concentration. For $n > 1 \times 10^{19} \text{ cm}^{-3}$, the donor surface state density decreases and the surface Fermi level saturates at the CNL, indicating a transition from an accumulation layer to flat bands. In contrast, Mg acts as an acceptor and its presence should change the type of conductivity from *n*-type to *p*-type. For $p > 1 \times 10^{19} \text{ cm}^{-3}$, the donor surface density increases while the surface Fermi level decreases, however, the surface sheet electron density decreases enormously, indicating a transition from electron accumulation to almost hole depletion

for high Mg-doped InN. As the Mg concentration increases, the donor surface states are increasingly compensated by Mg near-surface acceptors in the hole depletion region. These results give positive indications for the fabrication of InN *p-n* junctions, because electron accumulation naturally disappears at high Mg doping levels.

Chapter 6

Sulfur passivation of highly Mg-doped InN

6.1 Introduction

Undoped and Mg-doped InN exhibit a large electron accumulation at the surface and this is not desirable for a number of device applications. The results presented in Chapter 5 showed that the accumulation layer in *p*-type material can be drastically reduced by high Mg-doping, however, a complete reduction/removal has not yet been achieved. Therefore additional methods need to be developed to investigate a means of reducing the electron accumulation layer to zero and allowing a surface that can support a Schottky contact. However, the reduction of the electron accumulation at InN surface has been found to be difficult due to a resistance to chemical or physical surface treatments [6].

Plucinski *et al.* [190] deposited sulfur from an electrochemical cell onto the GaN(000 $\bar{1}$) surface and observed a 0.4 eV-0.5 eV shift in the Fermi level position toward low energy, suggesting the reduction of surface electron depletion. Surface chemistry of *n*- and *p*-doped InP(001) after treatment with sulfur was investigated by Chaseé *et al.* [109]. Their observations were similar to those reported by Plucinski [190] on GaN. Presented, core and valence band spectra and Auger transitions were related to changes in surface chemistry, indicating the changes in the surface Fermi energy position and band bending. Sulfur also was used successfully to passivate the surfaces of InAs [111–113], however, in this case the surface charge accumulation layer and associated downward band bending increased after treatment. Because sulfur changes the surface electronic properties of III-V semiconductors, hence sulfur treatment might be a very useful method to remove or reduce electron accumulation at the surface of InN films. Bailey *et al.* [106,108], Chang *et al.* [107] and Fishwick *et al.* [191] have all investigated the effects of treatment with ammonium polysulphide ($\text{NH}_4)_2\text{S}_x$ solution on the electronic properties of *c*-plane and *a*-plane InN. Their

results showed that after S treatment, the separation of the surface Fermi level to the valence band maximum was reduced by ~ 0.15 eV, indicating a reduction in the electron accumulation at the surface (see Figure 6.1). Moreover, exposing a sulfur treated InN sample to air for a significant time (ie a month) did not change the position of the surface Fermi level, indicating successful chemical passivation of the surface.

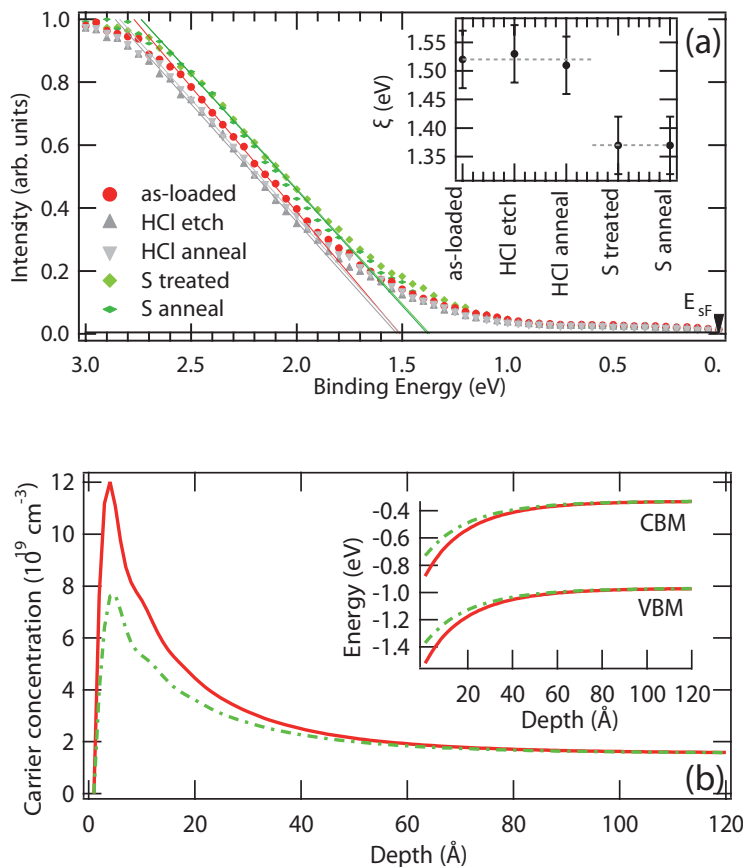


Figure 6.1: (a) Valence band edge XPS spectra for as-loaded, HCl etched, HCl etched and annealed, S treated, and S annealed InN with respect to the surface Fermi level E_{sF} . Inset: the separation of E_{sF} from the VBM, ξ , as a function of treatment (b) The carrier concentration as a function of depth from the InN surface for as-loaded (solid line) and S treated (dashed line). Inset: the CBM and VBM positions with respect to the Fermi level as a function of depth from the InN surface. These figures are taken from [106].

For this investigation, XPS was performed to study the surface electronic and chemical properties of highly Mg-doped InN treated with ammonium polysulphide $(\text{NH}_4)_2\text{S}_x$ solution. To determine the change in the surface electron carrier density with sulfur treatment, Poisson's equation was solved within the modified Thomas-Fermi approximation (MTFA).

6.2 Experimental details

Mg-doped InN samples were grown by PAMBE with a range of Mg cell temperatures (190°C - 320°C) at the University of Canterbury. All films were grown on *c*-plane sapphire substrate with a 3000 - 4000 nm GaN buffer layer, provided by Lumilog. The Mg concentration has been determined by SIMS using the Atomika 4500 SIMS instrument detailed in Section 3.5, using a 500 eV O₂⁺ incident ion beam. High-resolution XPS measurements were performed at room temperature using a monochromated Al-K_α X-ray source and an Omicron SPHERA spectrometer at the University of Warwick. Details of the spectrometer and its arrangement are described in Section 3.1.5. The Fermi level was calibrated from the position of the Fermi edge of a clean Ag(111) reference sample.

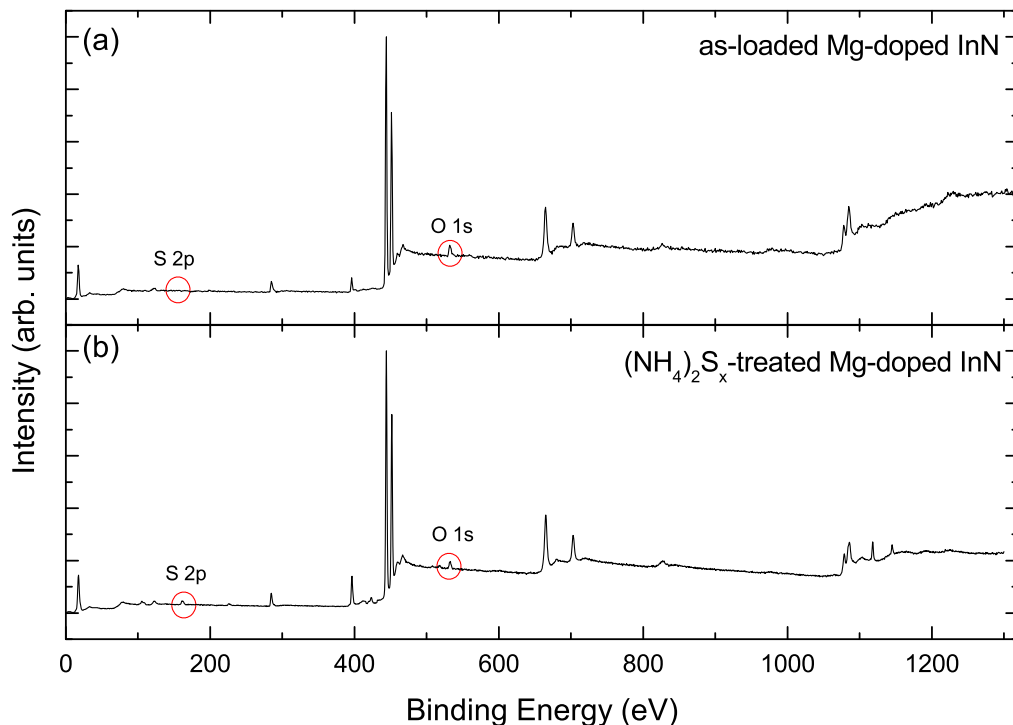


Figure 6.2: XPS wide energy scan from heavily doped Mg-doped InN ($h\nu = 1486.6$ eV) for (a) as-loaded film and (b) (NH₄)₂S_x-treated film. The binding energy scale is with respect to the Fermi level E_F .

Before (NH₄)₂S_x-treatment, the native oxide was observed in XPS from the Mg-doped InN surface, therefore the samples were etched in a 10 mol/l HCl solution for 60 s, followed by immediate rinsing in deionized water and drying by N₂ before

loading into the vacuum chamber. After measurements on cleaned Mg:InN, the samples were removed from the vacuum chamber and dipped, at room temperature, into the $(\text{NH}_4)_2\text{S}_x$ solution (20%) for 1 hour. The samples were then rinsed in deionized water and blown dry by N_2 before being reloaded into the vacuum chamber. Survey spectra from as loaded and $(\text{NH}_4)_2\text{S}_x$ -treated Mg-doped InN identifying the elements present in the near surface region are shown in 6.2.

6.3 Results and analysis

The valence band (VB) edge XPS spectra for cleaned Mg-doped InN and sulfur treated Mg-doped InN films are shown in Figure 6.3. The position of the surface Fermi level E_{sF} is again determined by extrapolating the leading edge of the VB spectra to the background level, accounting for a finite instrumental resolution. The lowering of the surface Fermi level with increasing Mg concentration for untreated samples was observed and this is explained in Chapter 5, however, some values observed are slightly different from what was observed previously on a similar set of samples. The lowest value of 0.90 eV is obtained for $[\text{Mg}] = 5.0 \times 10^{19}\text{cm}^{-3}$. After $(\text{NH}_4)_2\text{S}_x$ -treatment, the position of E_{sF} is shifted toward lower energies by ~ 0.08 eV, indicating that the surfaces have been passivated through the deposition of sulfur, similar to that previously found for undoped *c*-plane (see Figure 6.1) and *a*-plane InN [108,191]. The lowest value of E_{sF} has been found to be 0.82 eV for the sample with $[\text{Mg}] = 5.0 \times 10^{19}\text{cm}^{-3}$. The measured values of the E_{sF} are presented in Figure 6.4.

The XPS core level spectra presented below are deconvolved into components using a Voigt line shape, and a Shirley background. The Cl 2p and S 2p peaks are fitted with identical full width at half maximum values, and Voigt shape. After etching some amount of chlorine has remained on the surface. Chlorine is highly electronegative therefore its presence on the surface of InN can cause charge transfer from the surface, reducing the separation between the surface Fermi level and the valence band maximum [105]. However, after $(\text{NH}_4)_2\text{S}_x$ treatment the chlorine has been totally removed from the surface, therefore the shifts of surface Fermi level are

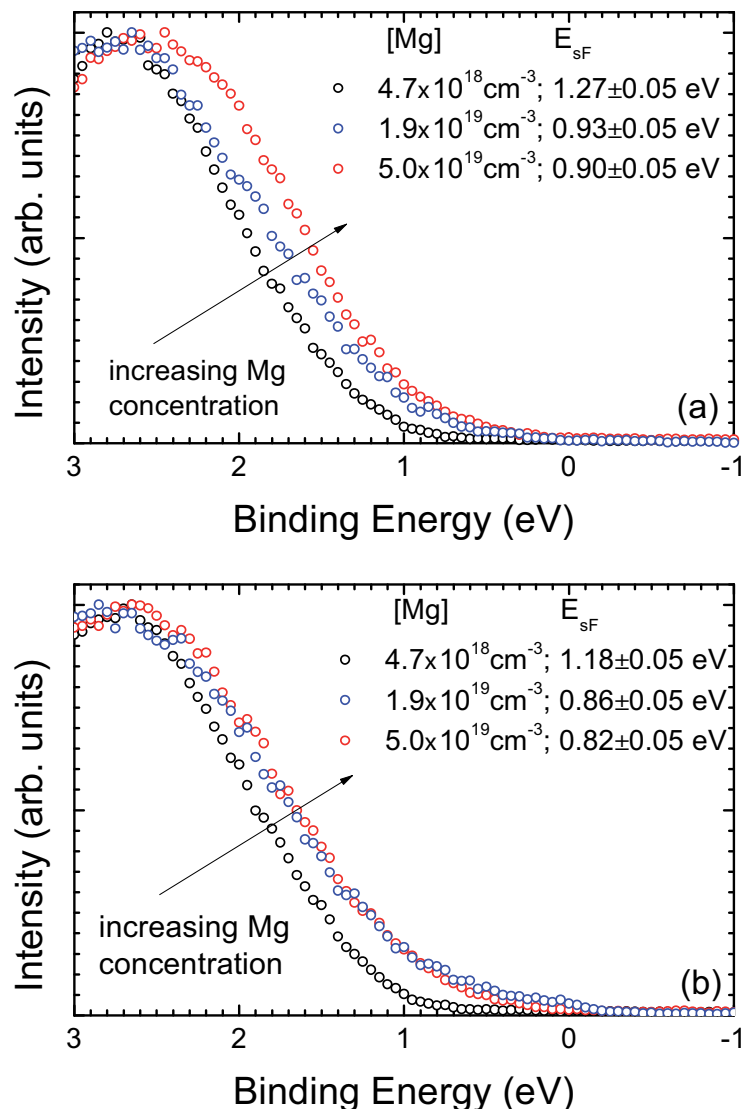


Figure 6.3: (a) Valence band photoemission spectra of Mg-doped InN for different Mg concentrations and (b) Valence band photoemission spectra for S-treated Mg-doped InN samples. The binding energy scale is with respect to the Fermi level E_F at zero.

not attributed to chlorine. The Cl 2p peak obtained from an HCl-etched sample is shown in Figure 6.5. This peak is fitted with two doublet peaks that are attributed to Cl-In bonding (~ 198.8 eV) and elemental Cl (~ 199.5).

The XPS core level spectra of In 3d_{5/2} and N 1s for untreated and $(\text{NH}_4)_2\text{S}_x$ -treated Mg-doped InN samples, demonstrating the effect of the shift in surface Fermi level, are shown in Figures 6.6 and 6.7. For In 3d_{5/2} and N 1s the average shift is found to be 0.07 ± 0.05 eV and 0.06 ± 0.05 eV respectively, which is consistent with the observed average shift of 0.08 ± 0.05 eV in the surface Fermi level position from the valence band spectra (Figures 6.3 and 6.4). These core level peaks have not

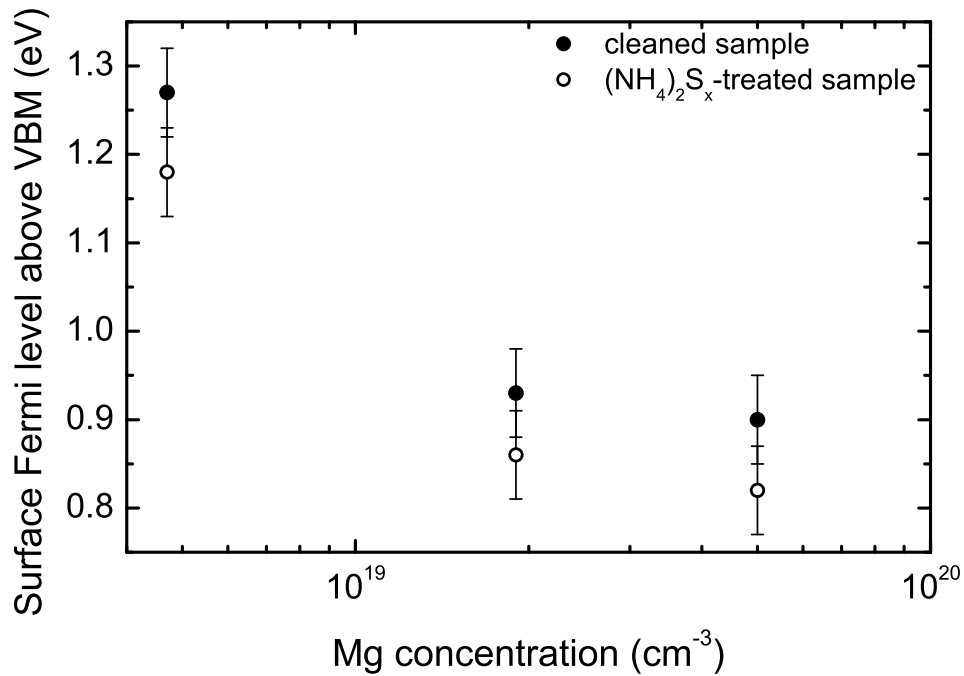


Figure 6.4: Position of the surface Fermi level with respect to the VBM as a function of Mg concentration for untreated (filled circles) and $(\text{NH}_4)_2\text{S}_x$ -treated (open circles) Mg-doped InN samples.

been fitted due to the effect of plasmon excitations of free electrons in the surface electron accumulation layer which have an influence on the line shape, resulting in an asymmetric peak [105]. Additionally, the oxygen, chlorine and sulfur bonding to indium also have a huge impact in a shoulder on the high binding energy side of the $\text{In } 3\text{d}_{5/2}$ line.

Studies on the surface chemistry and structure for the sulfur treated InP(100) reported by Tao *et al.* [192] and Lu *et al.* [193] showed that surfaces passivated using $(\text{NH}_4)_2\text{S}_x$ are terminated by S atoms, which form bridge bonds only to indium atoms. In this study, after a treatment of Mg:InN with $(\text{NH}_4)_2\text{S}_x$, different bridge-type bonds of In-S were also detected. The S 2p XPS spectrum for InN with $[\text{Mg}] = 1.9 \times 10^{19} \text{ cm}^{-3}$ is shown in Figure 6.8. This peak is fitted by three components with a spin-orbit splitting of 1.13 eV. These are for the different bonding environments observed at the surface, In-S-In (161.0 eV), In-S-S-In (162.0 eV) and elemental S (163.5 eV). Similar components in undoped InN have been observed previously by Bailey *et. al.* [194].

The surface coverage of chlorine, sulfur and oxygen are estimated using the

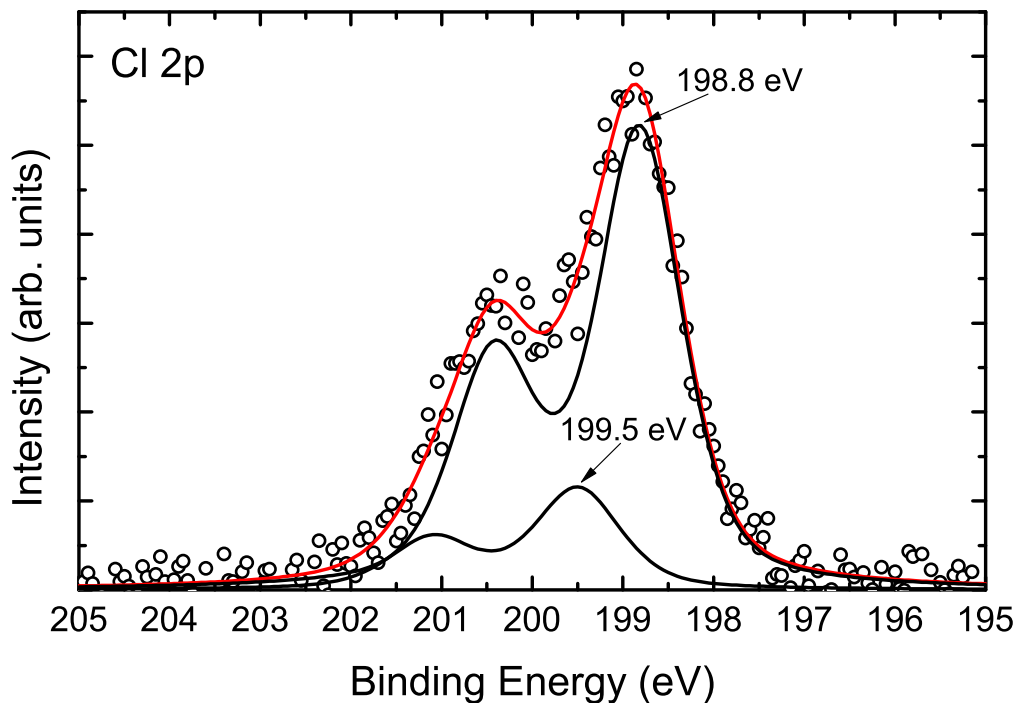


Figure 6.5: XPS spectrum of the Cl 2p peak for HCl etched Mg-doped InN sample. This peak is fitted with two doublet peaks that are attributed to Cl-In bonding (~ 198.8 eV) and Cl-Cl bonding (~ 199.5 eV).

Beer-Lambert law, with the area ratio of the core level peaks (Cl 2p, S 2p, O1s, In 3d_{5/2}). The kinetic energy of In 3d_{5/2}, O 1s, Cl 2p, and S 2p photoelectrons excited by a Al-K _{α} source are approximately 1043 eV, 955 eV, 1288 eV, and 1325 eV, respectively and therefore, from TPP-2M calculations [129] and using a density of 6.81 g cm⁻³ [195], the inelastic mean free path of the photoelectrons through InN is 18.08 Å, 16.93 Å, 21.23 Å, and 21.70 Å, respectively. The results of calculations are given in Table 6.1. It can be seen that S-treatment reduces the oxide layer. Moreover, a signal from Cl is undetectable, indicating a reduction of this element as well.

6.4 Discussion

The band bending and corresponding carrier concentration distribution as a function of depth from the surface of untreated and (NH₄)₂S_x treated Mg-doped InN films is shown in Figure 6.9. These profiles were evaluated numerically by solving Poisson's equation within MTFA, applying an inversion layer model and assuming that all

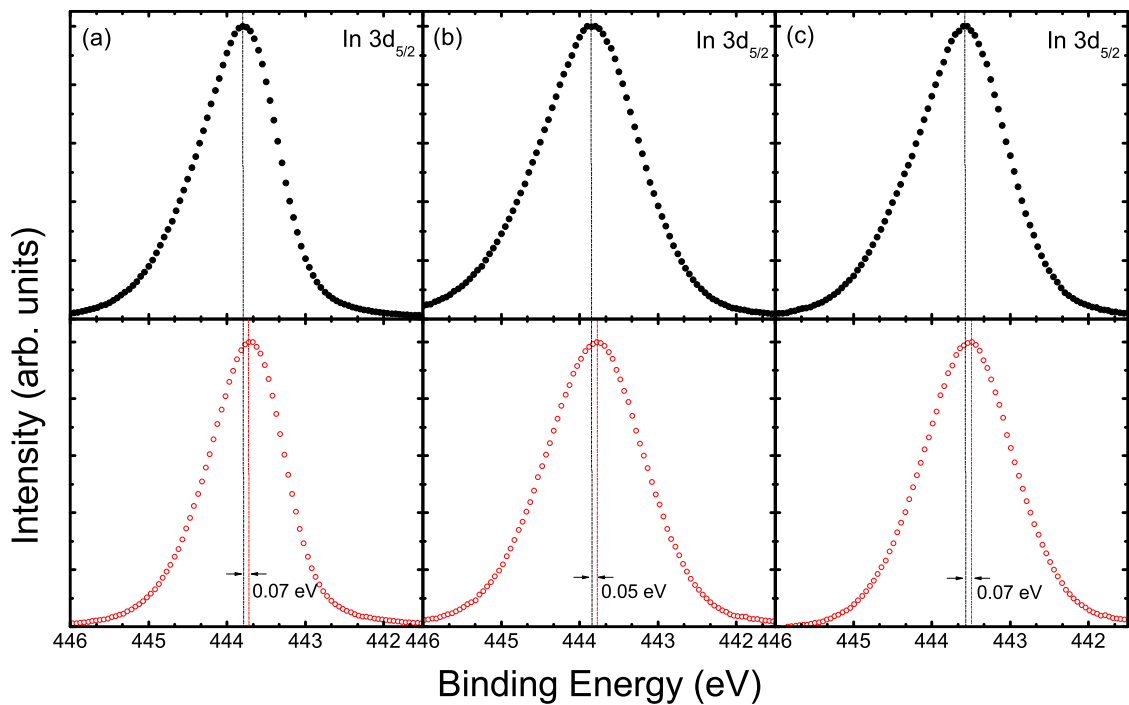


Figure 6.6: Core level XPS spectra of the In 3d_{5/2} for untreated (filled circles) and after (NH₄)₂S_x treatment (open circles) Mg-doped InN with different Mg concentrations a) [Mg]=4.7 × 10¹⁸ cm⁻³ b) [Mg]= 1.9 × 10¹⁹ cm⁻³ c) [Mg]=5.0 × 10¹⁹ cm⁻³.

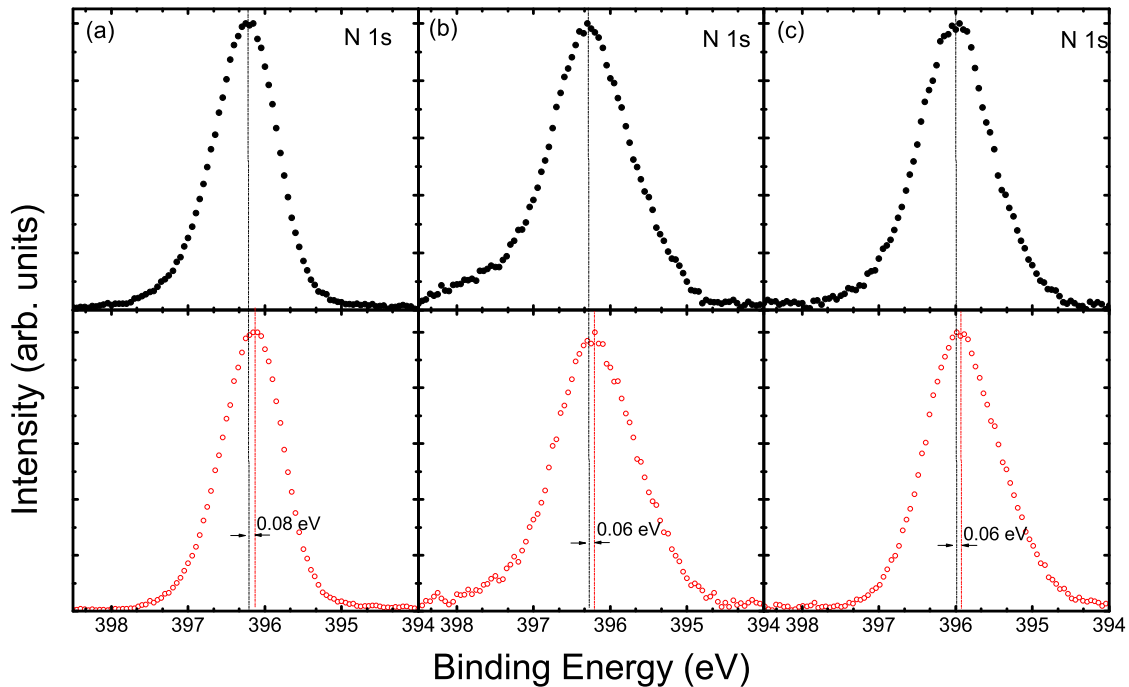


Figure 6.7: Core level XPS spectra of the N 1s for untreated (filled circles) and after (NH₄)₂S_x treatment (open circles) Mg-doped InN with different Mg concentrations a) [Mg]=4.7 × 10¹⁸ cm⁻³ b) [Mg]= 1.9 × 10¹⁹ cm⁻³ c) [Mg]=5.0 × 10¹⁹ cm⁻³.

Table 6.1: The estimated surface coverage of sulfur, chlorine and oxygen, as calculated from the Cl 2p, S 2p and O 1s core level peaks.

[Mg] (cm ⁻³)	treatment	S (Å)	Cl (Å)	O (Å)
4.7×10^{18}	untreated	—	0.17	1.12
	(NH ₄) ₂ S _x -treated	0.21	—	0.36
1.9×10^{19}	untreated	—	0.21	0.81
	(NH ₄) ₂ S _x -treated	0.16	—	0.57
5.0×10^{19}	untreated	—	0.15	0.79
	(NH ₄) ₂ S _x -treated	0.17	—	0.49

Mg atoms act as acceptors. The hole effective mass used in these calculations was $0.65m_e$ [182]. A giant reduction on the electron concentration in the accumulation layer, caused by compensation of the positively charged surface donor states by near-surface Mg acceptors in high Mg-doped InN films was explained in Chapter 5. After sulfur treatment the density of donor surface states slightly decreases, while the surface electron sheet density decreases markedly, indicating a significant reduction in the electron accumulation. For the sample with $[\text{Mg}] = 5.0 \times 10^{19} \text{ cm}^{-3}$, the surface electron sheet density decreases from $7.7 \times 10^8 \text{ cm}^{-2}$ to $2.1 \times 10^8 \text{ cm}^{-2}$, suggesting a reduction of 70%. The parameters used in space-charge calculations and values obtained from these calculations are presented in Table 6.2.

Table 6.2: Values of the surface Fermi level E_{sF} above the VBM from XPS measurements. The band bending V_{bb} is calculated from the relative surface and bulk Fermi level positions. Poisson-MTFA calculations give the surface state density n_{SS} and electron sheet density n_{2D} . Reduction in the surface electron accumulation is denoted as ΔR .

[Mg] (cm ⁻³)	treatment	E_{sF} (eV)	V_{bb} (eV)	n_{SS} (cm ⁻²)	n_{2D} (cm ⁻²)	ΔR %
4.7×10^{18}	untreated	1.27 ± 0.05	1.25	9.9×10^{12}	2.3×10^{12}	52
	(NH ₄) ₂ S _x -treated	1.18 ± 0.05	1.16	8.4×10^{12}	1.1×10^{12}	
1.9×10^{19}	untreated	0.93 ± 0.05	0.96	1.4×10^{13}	8.6×10^9	67
	(NH ₄) ₂ S _x -treated	0.86 ± 0.05	0.89	1.3×10^{13}	2.8×10^9	
5.0×10^{19}	untreated	0.89 ± 0.05	0.96	2.3×10^{13}	7.7×10^8	72
	(NH ₄) ₂ S _x -treated	0.82 ± 0.05	0.90	2.2×10^{13}	2.1×10^8	

The nature of the electron accumulation reduction caused by (NH₄)₂S_x treatment is different from that provided by Mg near-surface acceptors in the hole deple-

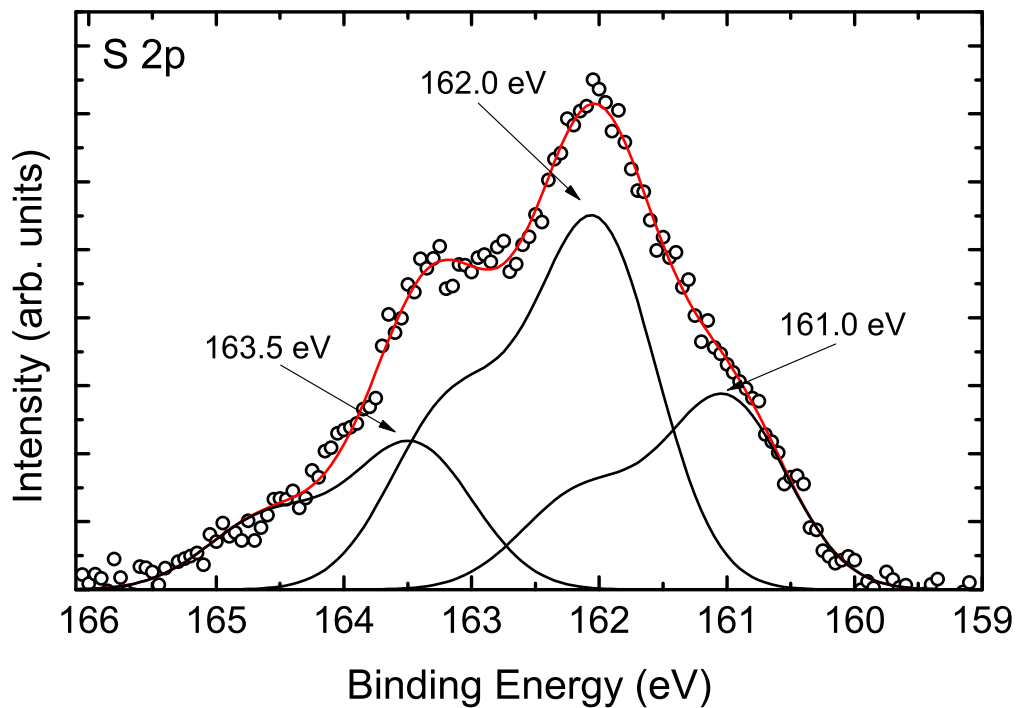


Figure 6.8: Core level XPS spectrum of S 2p for $(\text{NH}_4)_2\text{S}_x$ treated Mg-doped InN with $[\text{Mg}] = 1.9 \times 10^{19} \text{ cm}^{-3}$. This peak is fitted with three doublet peaks that are attributed to In-S-In bonding ($\sim 161.0 \text{ eV}$), In-S-S-In bonding ($\sim 162.0 \text{ eV}$) and elemental S ($\sim 163.5 \text{ eV}$).

tion region. It has been shown (see Chapter 5) that increasing the Mg concentration lowers both the bulk and surface Fermi levels, and this results in an increased density of donor surface states, n_{SS} , and a decrease in the surface sheet electron density, n_{2D} . In this case, the S-treatment lowers only the surface Fermi level without any influence on the bulk Fermi level position. This results in a decrease of both n_{SS} and n_{2D} . Therefore the reduction of surface electron accumulation might come from the transfer of charge from the InN to more electronegative sulfur atoms or indium sulphide. This could be achieved forming both In-S-In and In-S-S-In bonds at the surface. This is in agreement with the previous results on undoped *c*-plane and *a*-plane InN [106, 191], but in contrast to InAs where $(\text{NH}_4)_2\text{S}_x$ treatment results in an increased surface Fermi level caused by sulfur substitution on the group V sublattice, acting as a source of donors [113, 196]. In the case of InN, the sulfur atoms do not act as a source of donors because their substitution onto nitrogen sites is stopped by the indium adlayers at the surface of InN. An additional possibility of the lowering of the donor surface state density might be the breaking of In-In bonds

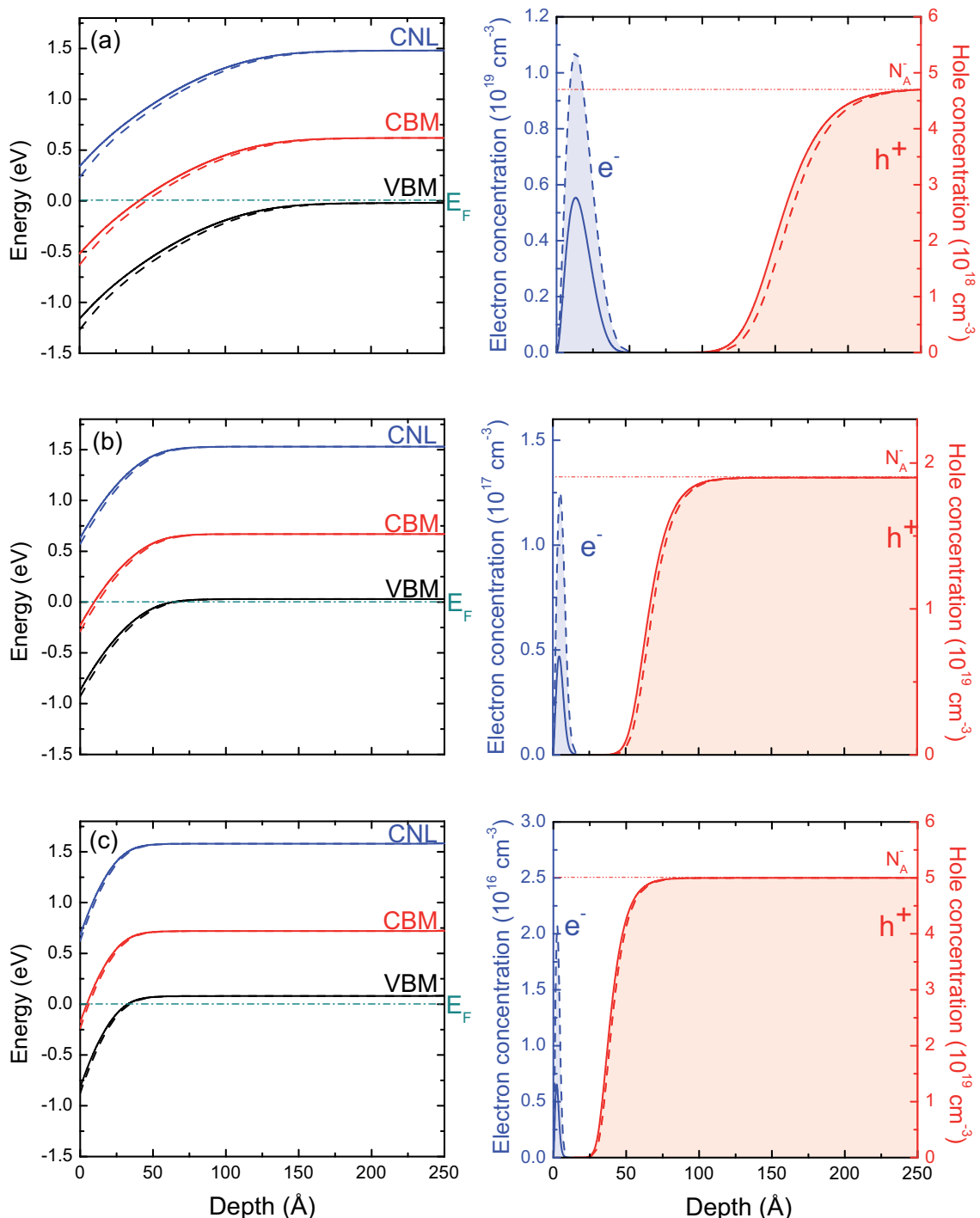


Figure 6.9: The conduction band minimum, valence band maximum and charge neutrality level respect to the Fermi level and corresponding carrier concentration profile, as a function of depth before (dashed line) and after $(\text{NH}_4)_2\text{S}_x$ treatment (solid line), for a Mg concentration of (a) $4.7 \times 10^{18} \text{ cm}^{-3}$, (b) $1.9 \times 10^{19} \text{ cm}^{-3}$ and (c) $5.0 \times 10^{19} \text{ cm}^{-3}$.

in In adlayer, being the microscopic origin of the surface electron accumulation.

In these studies, a small shift in the surface Fermi level (~ 0.08 eV) provides a huge reduction in the surface electron accumulation (Table 6.2). This is in contrast to previous reported studies on undoped sulfur passivated InN, where larger shifts ~ 0.15 eV [106] and 0.20 eV [107] gave the smaller reduction of 30%. A key to understanding this difference can be found in the density of states diagram and the Fermi level position on it.

For undoped *c*-plane InN, the surface Fermi level before and after S-treatment was located at ~ 1.50 eV and ~ 1.35 eV above the valence band maximum, respectively [106]. In the Figure 6.10 these Fermi levels are located in the region where the surface state density histogram is relatively flat and low, therefore a small shift of the surface Fermi level gives a small impact in electron accumulation reduction. The other situation is when the surface Fermi level is located at ~ 0.90 eV above the VBM in density of states diagram. Here the surface state density histogram is high and steep, therefore even small changes in position of the surface Fermi level lead to a significant reduction of the surface electron accumulation.

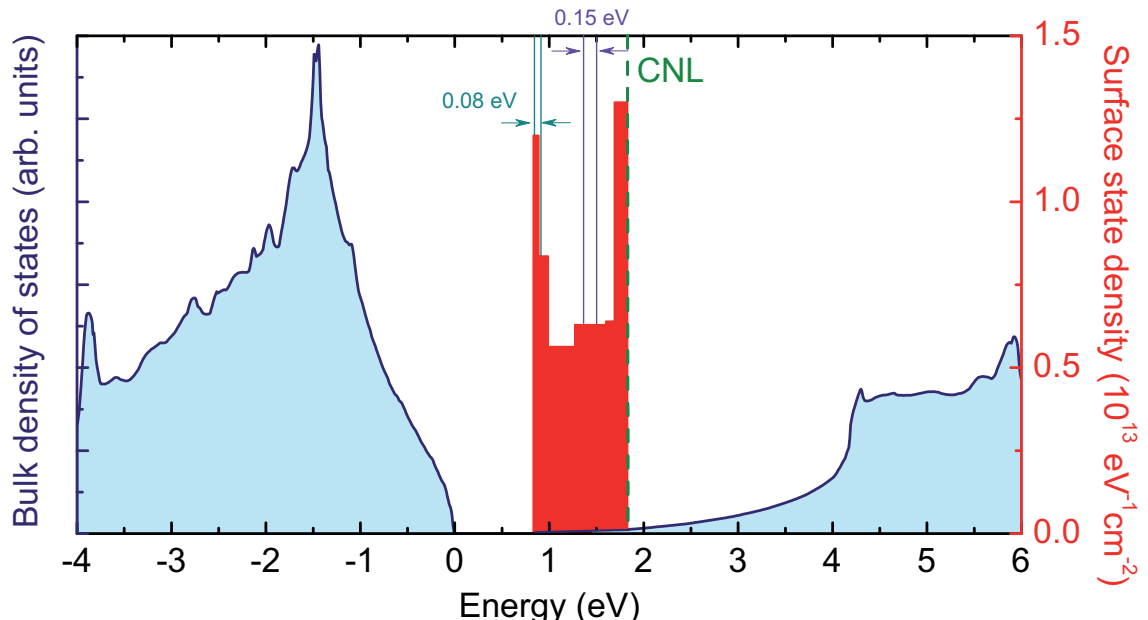


Figure 6.10: Surface state density (red histogram) evaluated by numerically solving Poisson's equation within MTFA as described in Chapter 2.2 and bulk DOS (blue line) for the InN(0001) calculated by F. Bechstedt's group [148], using quasiparticle-corrected density-functional theory (QPC-DFT).

6.5 Conclusions

In conclusion, X-ray photoemission spectroscopy has been used to investigate the influence of ammonium sulfide on electron accumulation in highly Mg-doped InN films. After $(\text{NH}_4)_2\text{S}_x$ treatment a small shift of surface Fermi level (~ 0.08 eV) towards low energy results in the surface sheet electron density reducing by 50–70%. This reduction is possibly due to the transfer of charge from the InN to more electronegative sulfur atoms or indium sulphide, achieved by forming In-S-In and In-S-S-In bonds at the surface. Previous results on undoped *c*-plane InN [106] show much smaller reduction (30%) than that presented here. This discrepancy can be explained by the shape of the distribution of the donor surface sheet density.

A complete reduction of electron accumulation has not been achieved but the results presented in this thesis show that this might be possible, especially for highly Mg-doped InN, where Mg near-surface acceptors naturally compensate donor surface states.

Chapter 7

Surface electronic properties of In-rich InGaN alloys grown by MOCVD

7.1 Introduction

$\text{In}_x\text{Ga}_{1-x}\text{N}$ alloys have many fundamental properties that make them promising for use in device applications. The band gap of $\text{In}_x\text{Ga}_{1-x}\text{N}$ alloys span a wide range of energies from 0.64 eV to 3.44 eV [53, 55]. As shown in Figure 1.1, this range of band gaps cover the entire solar spectrum from the ultraviolet to the near infrared, making this material beneficial in multi-junction photovoltaic devices with a large spectral window. This allows a multi-junction solar cell to be constructed from a single material with a efficiency potentially higher than 50% [197]. Currently, only Ga-rich $\text{In}_x\text{Ga}_{1-x}\text{N}$ alloys have been used successfully in applications such as blue, green and ultraviolet nitride-based light-emitting diodes (LEDs) and laser structures. This is in part due to high defect and dislocation densities in In-rich $\text{In}_x\text{Ga}_{1-x}\text{N}$ alloys [198]. Additionally, growing high quality In-rich $\text{In}_x\text{Ga}_{1-x}\text{N}$ layers remains a challenge due to a large difference in the thermal stability and inter-atomic spacing in InN and GaN. Typically $\text{In}_x\text{Ga}_{1-x}\text{N}$ layers are grown by either MBE [199] or Metal Organic Chemical Vapour Deposition (MOCVD) [200]. However, MOCVD is more challenging due to the ineffective cracking of NH_3 at the required low growth temperature of $\text{In}_x\text{Ga}_{1-x}\text{N}$ layer [201]. Tuna *et al.* investigated the effect of the subjacent InN layer on In content variation in $\text{In}_x\text{Ga}_{1-x}\text{N}$ by inserting a thin InN interlayer in between GaN templates and $\text{In}_x\text{Ga}_{1-x}\text{N}$ layer [202]. The electronic properties of samples grown in this manner have been investigated and the results are presented in this chapter.

The surface electronic properties of $\text{In}_x\text{Ga}_{1-x}\text{N}$ play a very important role in devices. Undoped, *n*-type and *p*-type doped InN exhibit electron accumulation at

the surface (see Chapters 4 and 5). *n*-type GaN exhibits electron depletion [203] near the surface, therefore there is an expected transition from electron depletion to electron accumulation for *n*-type $\text{In}_x\text{Ga}_{1-x}\text{N}$ at some alloy composition. This transition has previously been reported many times for materials grown by PAMBE [27, 28, 194, 204], however, no investigation as yet has reported the surface electronic properties of $\text{In}_x\text{Ga}_{1-x}\text{N}$ grown by MOCVD. Additionally, previous XPS results have been presented for surfaces in the presence of native oxides [27, 28, 194, 204]. Veal *et al.* [27, 204] reported that the transition appears at $x = 0.43$, where the surface Fermi level crosses the charge neutrality level (CNL). In 2008 Bailey *et al.* [194] postulated that the previous reported results were a first approximation and that the true transition point can only be obtained from knowledge of both the surface and bulk Fermi level positions.

This chapter contains an investigation of the surface and bulk Fermi level positions for a range of compositions of cleaned $\text{In}_x\text{Ga}_{1-x}\text{N}$ samples grown by MOCVD using high-resolution XPS, IR reflectivity measurements and solutions of Poisson's equation within the MTFA, as described in Section 2.2.

7.2 Experimental details

Several series of samples of 120-230 nm thick In-rich and Ga-rich $\text{In}_x\text{Ga}_{1-x}\text{N}$ were investigated with a composition range of $0.20 \leq x \leq 1.00$. All the samples were grown in an AIXTRON MOCVD system [201]. The $\text{In}_{0.20}\text{Ga}_{0.80}\text{N}$ sample was grown on a *c*-plane sapphire substrate with a GaN buffer layer. All other samples were grown on a *c*-plane sapphire substrate with a GaN buffer and a very thin InN buffer layer.

XPS measurements were performed using an Omicron SPHERA spectrometer at the University of Warwick, UK. The samples were probed with a photon beam of energy $h\nu = 1486.6$ eV produced by a monochromated $\text{Al } K_{\alpha}$ x-ray source. The IR reflection spectra from the $\text{In}_x\text{Ga}_{1-x}\text{N}$ samples were measured using a Bruker Vertex 70v Fourier transform IR spectrometer. The reflection spectra were recorded for an incident and reflected angle of 11° to the surface normal. ECV measurements

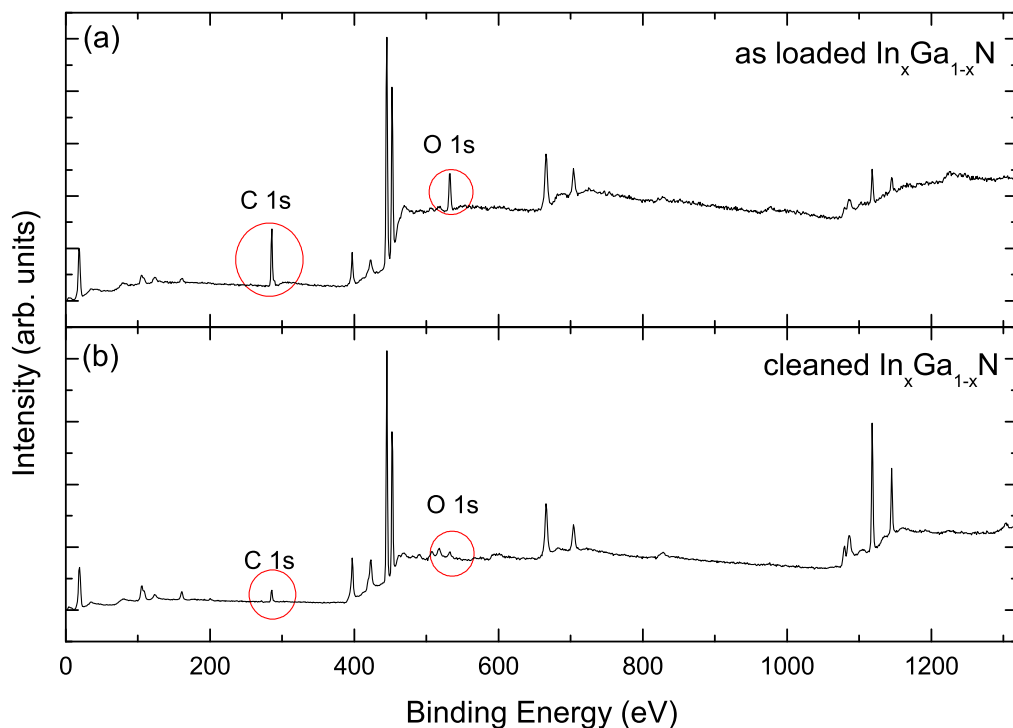


Figure 7.1: XPS wide energy scan from $\text{In}_x \text{Ga}_{1-x}\text{N}$ ($h\nu = 1486.6$ eV) for (a) as-loaded film and (b) cleaned film. The binding energy scale is with respect to the Fermi level E_F .

were performed in 0.1 mol/l solution of potassium hydroxide using a Dage Wafer Profiler CVP21.

Before any treatments were performed, native oxides were observed on the surfaces of $\text{In}_x \text{Ga}_{1-x}\text{N}$ alloys by XPS. In order to investigate the valence band spectra without the influence of effects due to the native oxide, the samples were subjected to HCl etching and *in situ* annealing (shown in Figure 7.1). The sample were dipped in a solution of HCl (10 mol/l) for 60 s, rinsed in deionized water and immediately blown dry with N_2 before loading into the vacuum chamber and then annealing in vacuo at 300°C for 2 hours. All measurements were performed at room temperature.

7.3 Results and analysis

The In 3d, Ga 2p_{3/2}, N 1s, and O 1s core level XPS spectra were all recorded from the $\text{In}_{0.62}\text{Ga}_{0.38}\text{N}$ sample before and after cleaning and are shown in Figure 7.2. The In 3d_{3/2} and 3d_{5/2} peaks measured before cleaning consist of In-N components at

Table 7.1: Values of the surface Fermi level E_{sF} above the VBM from XPS measurements and bulk Fermi level E_{bF} above the VBM calculated using Fermi-Dirac carrier statistics. The band bending V_{bb} is calculated from the relative surface and bulk Fermi level positions. The bulk carrier concentration is determined from the plasma frequency using a non-parabolic band structure approximation [79]. The band gap was calculated using Equation 7.1.

Sample	E_{sF} (eV)	E_{bF} (eV)	E_g (eV)	V_{bb} (eV)	n_b (10^{18}cm^{-3})	n_{ss} (10^{13}cm^{-2})
InN	1.42 ± 0.05	0.84 ± 0.05	0.64	0.58	6.2	1.28
$\text{In}_{0.82}\text{Ga}_{0.18}\text{N}$	1.55 ± 0.05	1.09 ± 0.05	0.88	0.46	9.5	1.06
$\text{In}_{0.75}\text{Ga}_{0.25}\text{N}$	1.65 ± 0.05	1.18 ± 0.05	1.02	0.47	7.2	1.05
$\text{In}_{0.62}\text{Ga}_{0.38}\text{N}$	1.82 ± 0.05	1.43 ± 0.05	1.30	0.39	6.7	0.88
$\text{In}_{0.54}\text{Ga}_{0.46}\text{N}$	1.94 ± 0.05	1.60 ± 0.05	1.51	0.34	5.2	0.70
$\text{In}_{0.40}\text{Ga}_{0.60}\text{N}$	2.10 ± 0.05	1.95 ± 0.05	1.91	0.15	2.9	0.20
$\text{In}_{0.20}\text{Ga}_{0.80}\text{N}$	2.68 ± 0.05	2.65 ± 0.05	2.61	0.03	4.1	0.01

452.1 eV and 444.5 eV respectively (Figure 7.2 (a)), and each has a high binding energy shoulder due to In-O components. After etching, the In-O components are completely removed or still exist but in smaller quantity. Due to the high electronegativity of N, large chemical shifts are observed for N 1s core level peaks. The N 1s peaks at 396.9 eV (Figure 7.2 (c)) and at 395.2 eV are due to N-In and N-Ga bonding, respectively. Before and after cleaning, the O 1s peak consists of a component at 532.2 eV (Figure 7.2 (d)), coming from incidental oxygen and a lower energy component at 530.4 eV due to In-O bonding. After surface treatment, a reduction of the oxide layer of $\geq 75\%$ was achieved. The core level spectra from the other $\text{In}_x\text{Ga}_{1-x}\text{N}$ alloys exhibit similar behaviour and the reduction in oxygen coverage as a result of the cleaning process.

The valence band (VB) edge XPS spectra for cleaned $\text{In}_x\text{Ga}_{1-x}\text{N}$ samples are shown in Figure 7.3. The position of the surface Fermi level (E_{sF}) was again determined by extrapolating a linear fit to the leading edge of the valence band photoemission to account for the finite resolution of the spectrometer. It has been found that the E_{sF} for InN is 1.42 eV above the valence band maximum (VBM) and increases to 2.76 eV for $\text{In}_{0.20}\text{Ga}_{0.80}\text{N}$, as shown in Table 7.1. This change is monotonic with alloy composition and this behaviour has previously been observed for n - $\text{In}_x\text{Al}_{1-x}\text{N}$ [205] and n - $\text{In}_x\text{Ga}_{1-x}\text{N}$ [204] grown by PAMBE.

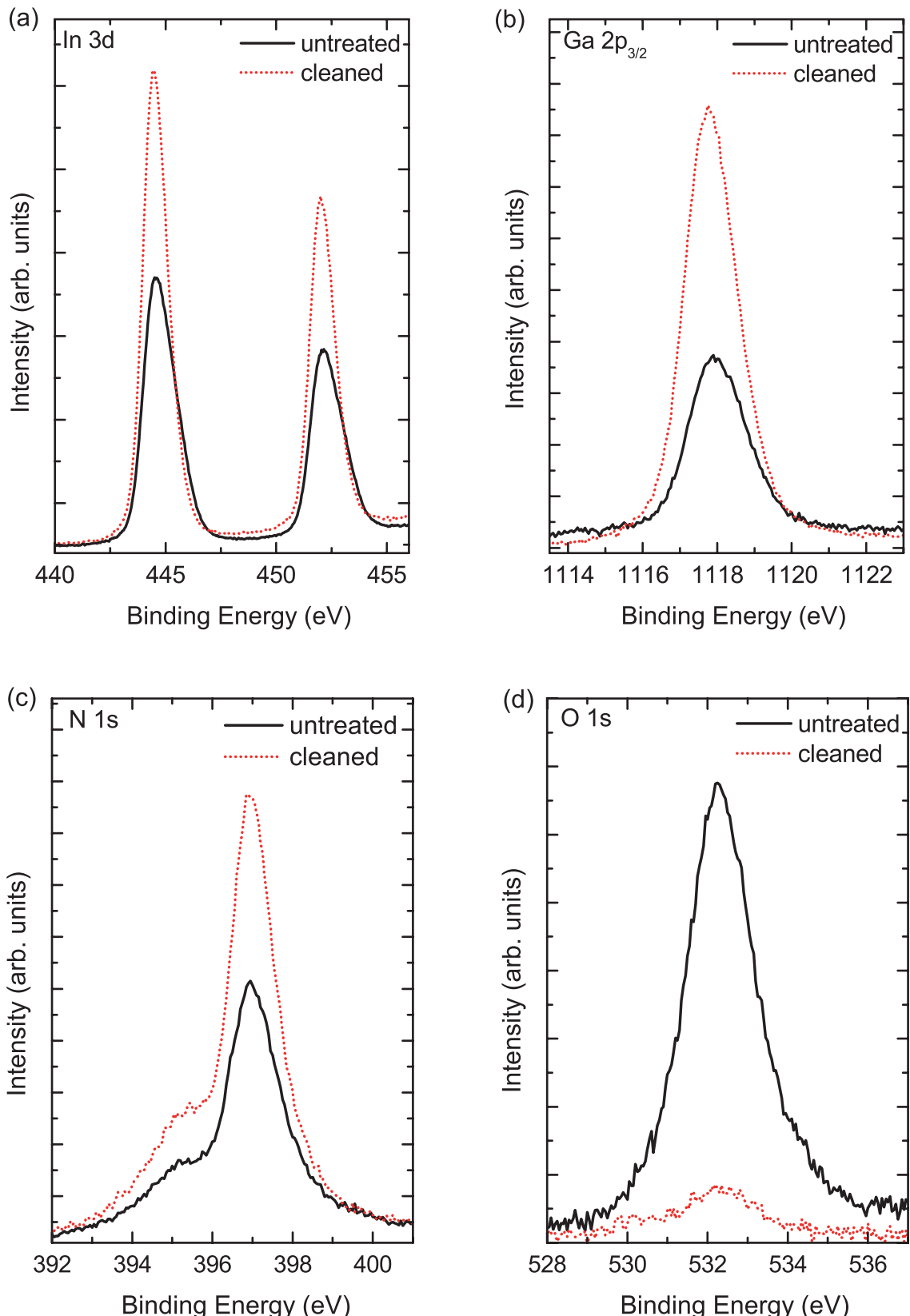


Figure 7.2: Core level spectra recorded at normal emission (emission angle 90°) from an untreated (black), and treated (red) $\text{In}_{0.62}\text{Ga}_{0.38}\text{N}$ sample for (a) In 3d, (b) Ga 2p_{3/2}, (c) N 1s and (d) O 1s.

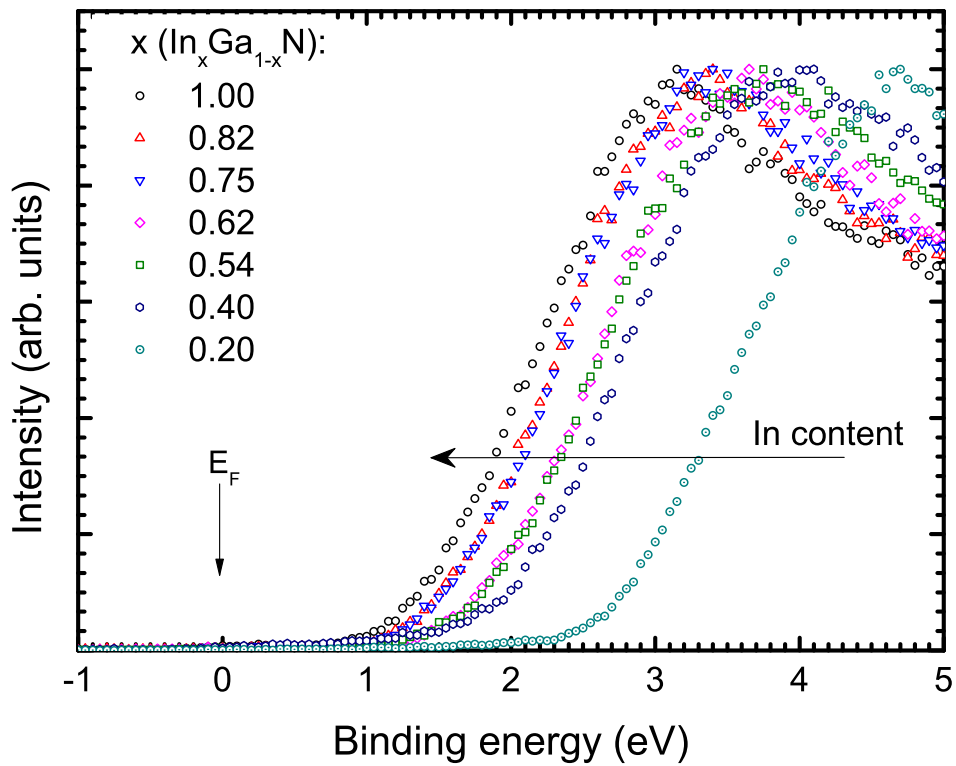


Figure 7.3: Valence band photoemission spectra with respect to the Fermi level (E_F) of cleaned $In_xGa_{1-x}N$ alloys across the composition range of $0.20 \leq x \leq 1.00$. The binding scale is with respect to the Fermi level E_F .

To determine the position of the bulk Fermi level, infrared reflectivity with modelling and Hall effect measurements were performed. Because the measured conductivity in the $In_xGa_{1-x}N$ samples might well be influenced by parallel conduction in the InN buffer layer and GaN, IR reflectivity measurements were performed firstly on GaN/sapphire and InN/GaN/sapphire. The parameters, such as plasma frequency and thickness obtained from these samples, were used in the modelling of the IR reflectivity measurements on $In_xGa_{1-x}N$ layers. The reflectivity spectra for the GaN/sapphire, InN/GaN/sapphire and $In_xGa_{1-x}N$ /InN/GaN/sapphire are presented in Figures 7.4, 7.5 and 7.6. To model the IR spectra of $In_xGa_{1-x}N$, a four layer model consisting of an $In_xGa_{1-x}N$ layer, an InN interface layer, a GaN layer, and bulk sapphire was applied. Additionally, the dielectric function of sapphire was simulated using the factorised model (described in Section 3.2.2), whereas the dielectric function of GaN, InN, and $In_xGa_{1-x}N$ was simulated with a two-oscillator dielectric model (described in Section 3.2.1). The high frequency dielectric con-

Table 7.2: Parameters used in the infrared reflectivity simulations, where ω_{TO} , ω_P , τ , d are the longitudinal optical phonon frequency, the plasma frequency, the free-carrier lifetime, and layer thickness, respectively.

Sample	$\varepsilon(\infty)$	$\varepsilon(0)$	ω_P (meV)	τ (meV)	d (nm)
GaN	5.35	8.9	29.5 ± 2	13 ± 2	5800 ± 20
InN	6.7	10.50	200 ± 10	25 ± 2	15 ± 2
GaN	5.35	8.9	29.5 ± 2	14 ± 2	5880 ± 20
InN	6.7	10.50	140 ± 5	15 ± 3	180 ± 5
InN	6.7	10.50	200 ± 10	25 ± 2	12 ± 2
GaN	5.35	8.9	29 ± 2	13 ± 2	6580 ± 30
$\text{In}_{0.82}\text{Ga}_{0.18}\text{N}$	6.45	10.20	160 ± 4	30 ± 5	145 ± 5
InN	6.7	10.50	200 ± 10	25 ± 6	8 ± 1
GaN	5.35	8.9	36 ± 5	60 ± 5	2290 ± 20
$\text{In}_{0.75}\text{Ga}_{0.25}\text{N}$	6.36	10.10	132 ± 3	50 ± 5	245 ± 5
InN	6.7	10.50	200 ± 10	25 ± 2	12 ± 1
GaN	5.35	8.9	28 ± 2	20 ± 3	6640 ± 20
$\text{In}_{0.62}\text{Ga}_{0.38}\text{N}$	6.20	9.90	120 ± 3	30 ± 4	215 ± 5
InN	6.7	10.50	200 ± 10	25 ± 2	12 ± 1
GaN	5.35	8.9	30 ± 4	26 ± 3	6700 ± 20
$\text{In}_{0.54}\text{Ga}_{0.46}\text{N}$	6.10	9.76	100 ± 4	18 ± 3	210 ± 2
InN	6.7	10.50	200 ± 10	25 ± 2	12 ± 1
GaN	5.35	8.9	20 ± 3	80 ± 5	5340 ± 15
$\text{In}_{0.40}\text{Ga}_{0.60}\text{N}$	5.89	9.54	70 ± 6	8 ± 2	220 ± 5
InN	6.7	10.50	200 ± 10	25 ± 2	10 ± 1
GaN	5.35	8.9	40 ± 4	17 ± 2	4325 ± 10
$\text{In}_{0.20}\text{Ga}_{0.80}\text{N}$	5.62	9.22	72 ± 5	12 ± 2	50 ± 2
GaN	5.35	8.9	36 ± 5	10 ± 2	2220 ± 10

stant and static dielectric constant for InN (GaN), $\varepsilon(\infty)=6.90$ (5.35) [77, 194] and $\varepsilon(0)=12.48$ (8.90) [77, 194] have been used to simulate the infrared reflectivity spectra. It has been assumed that high frequency dielectric and static dielectric constants for $\text{In}_x\text{Ga}_{1-x}\text{N}$ change linearly with the composition [206]. The parameters used in the simulations are given in Table 7.2.

The oscillations observed in the experimental spectra arise from Fabry-Pérot interference, corresponding to the total film thickness. Calculations using Fermi-Dirac statistics were undertaken to determine the carrier concentration and position of the bulk Fermi level from the measured conduction electron plasma frequency.

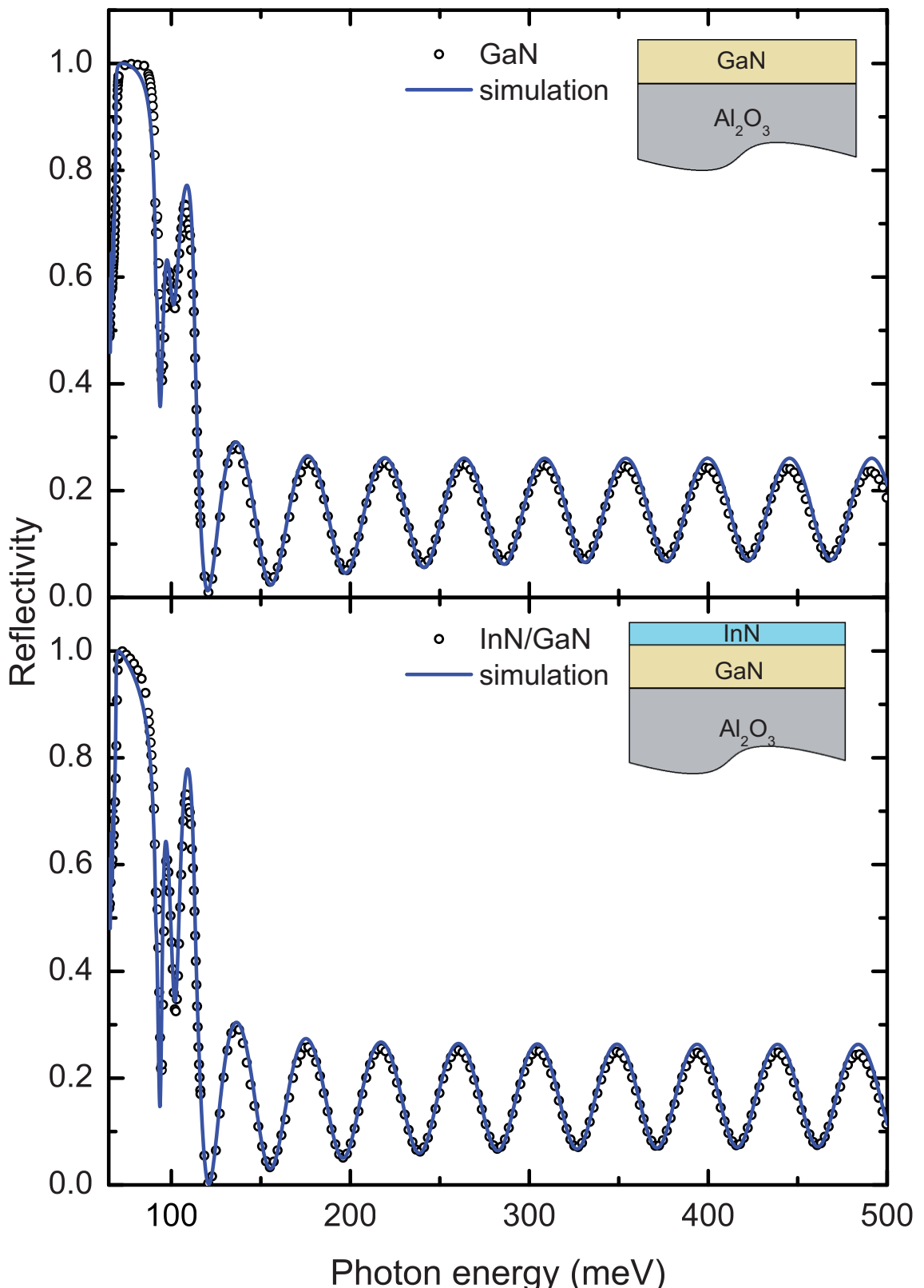


Figure 7.4: The experimental infrared reflectivity spectra for GaN and InN/GaN with the simulated spectra. In the modelling of GaN a two layer model consisting of a GaN layer and bulk sapphire was applied, whereas the IR spectrum for InN/GaN was obtained by applying a three layer model consisting of an InN layer, a GaN layer and bulk sapphire. The layer models are schematically presented in the insets.

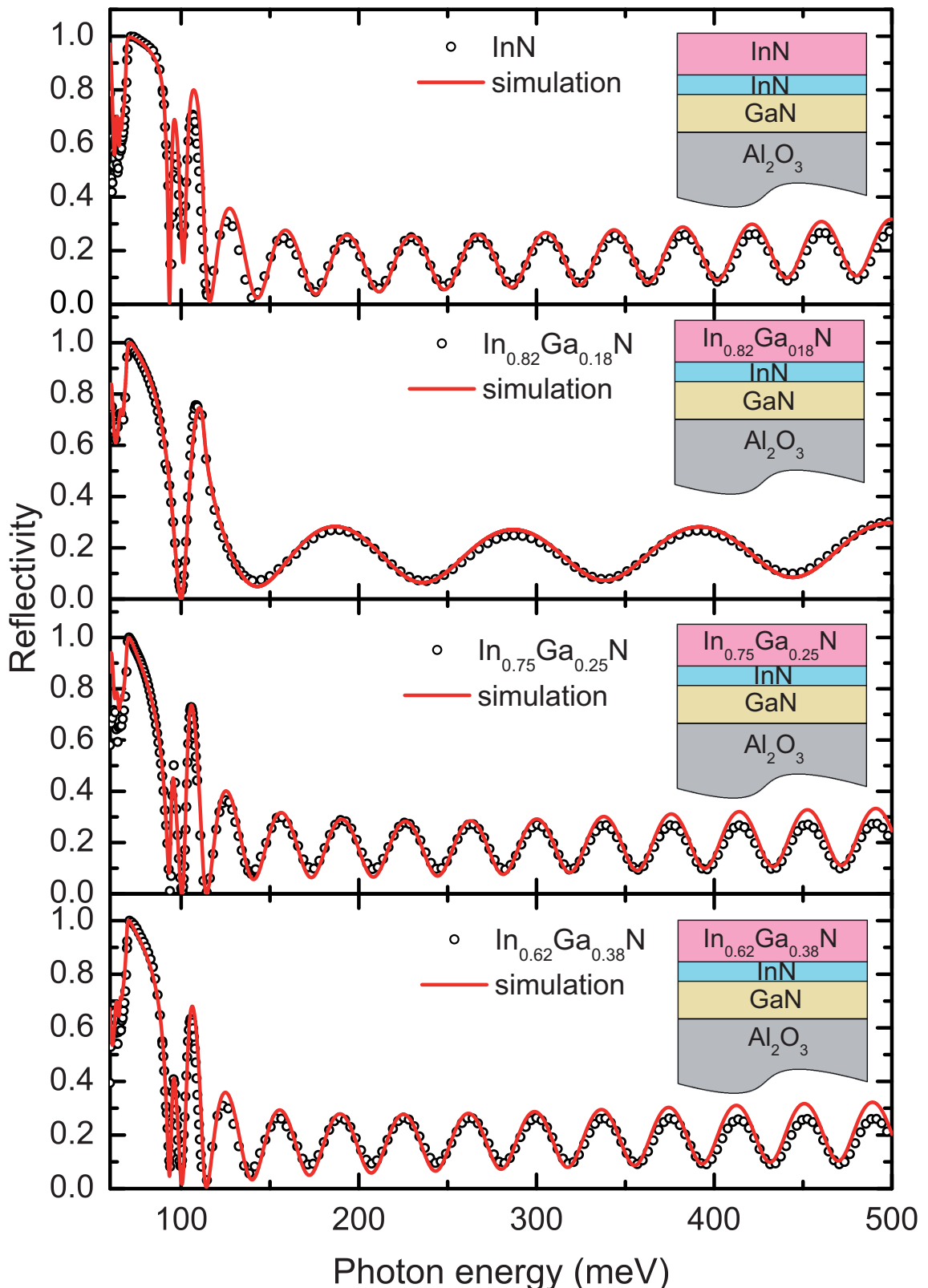


Figure 7.5: The experimental infrared reflectivity spectra for InN , $\text{In}_{0.82}\text{Ga}_{0.18}\text{N}$, $\text{In}_{0.75}\text{Ga}_{0.25}\text{N}$ and $\text{In}_{0.62}\text{Ga}_{0.38}\text{N}$ with the simulated spectra. In the modelling a four layer model consisting of an $\text{In}_x\text{Ga}_{1-x}\text{N}$ layer, an InN interface layer, a GaN layer and bulk sapphire was used, schematically presented in the insets.

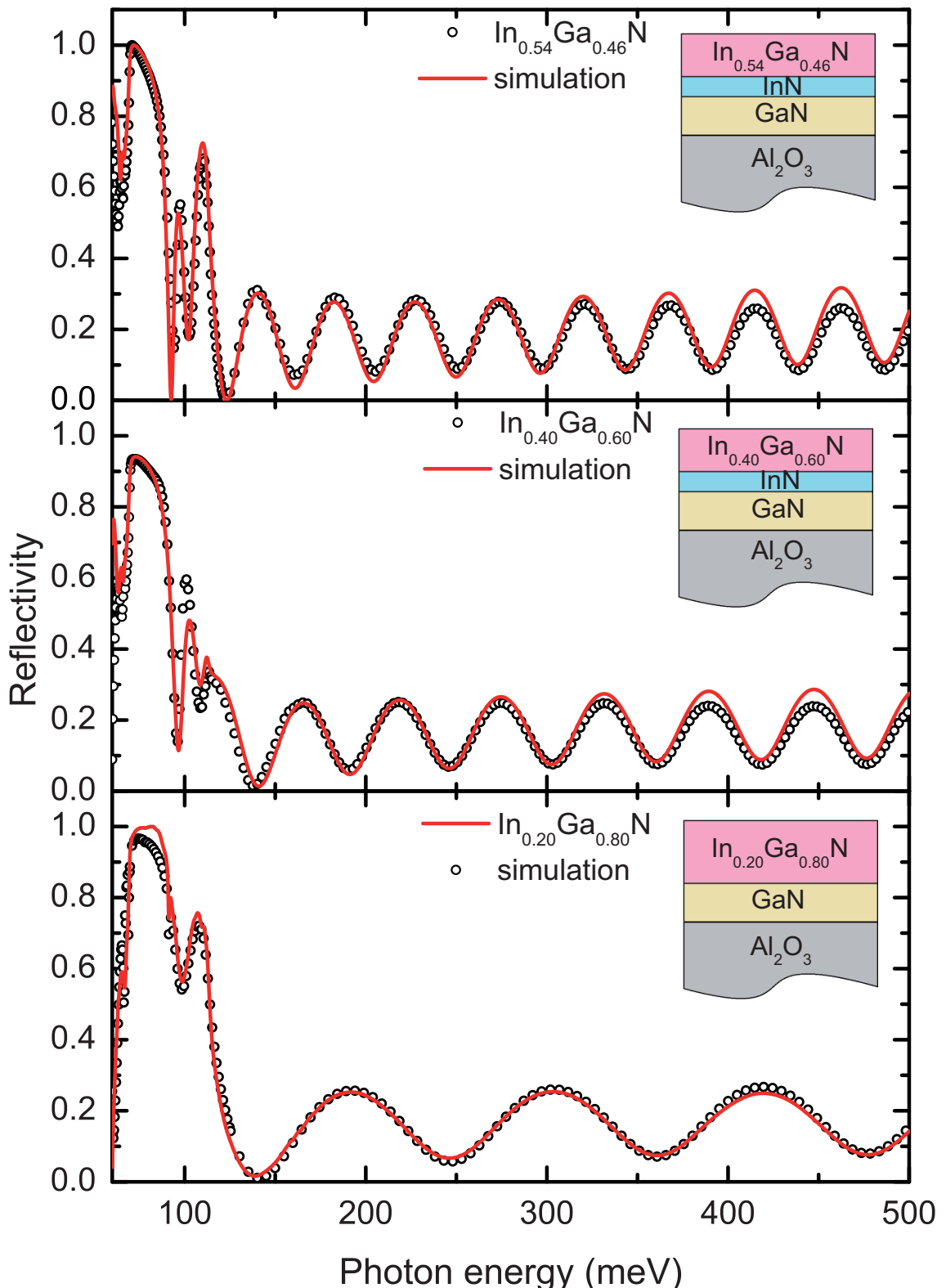


Figure 7.6: The experimental infrared reflectivity spectra for $\text{In}_{0.54}\text{Ga}_{0.46}\text{N}$, $\text{In}_{0.40}\text{Ga}_{0.60}\text{N}$ and $\text{In}_{0.20}\text{Ga}_{0.80}\text{N}$ with the simulated spectra. In the modelling a four layer model consisting of an $\text{In}_x\text{Ga}_{1-x}\text{N}$ layer, an InN interface layer, a GaN layer and bulk sapphire was used, schematically presented in the insets.

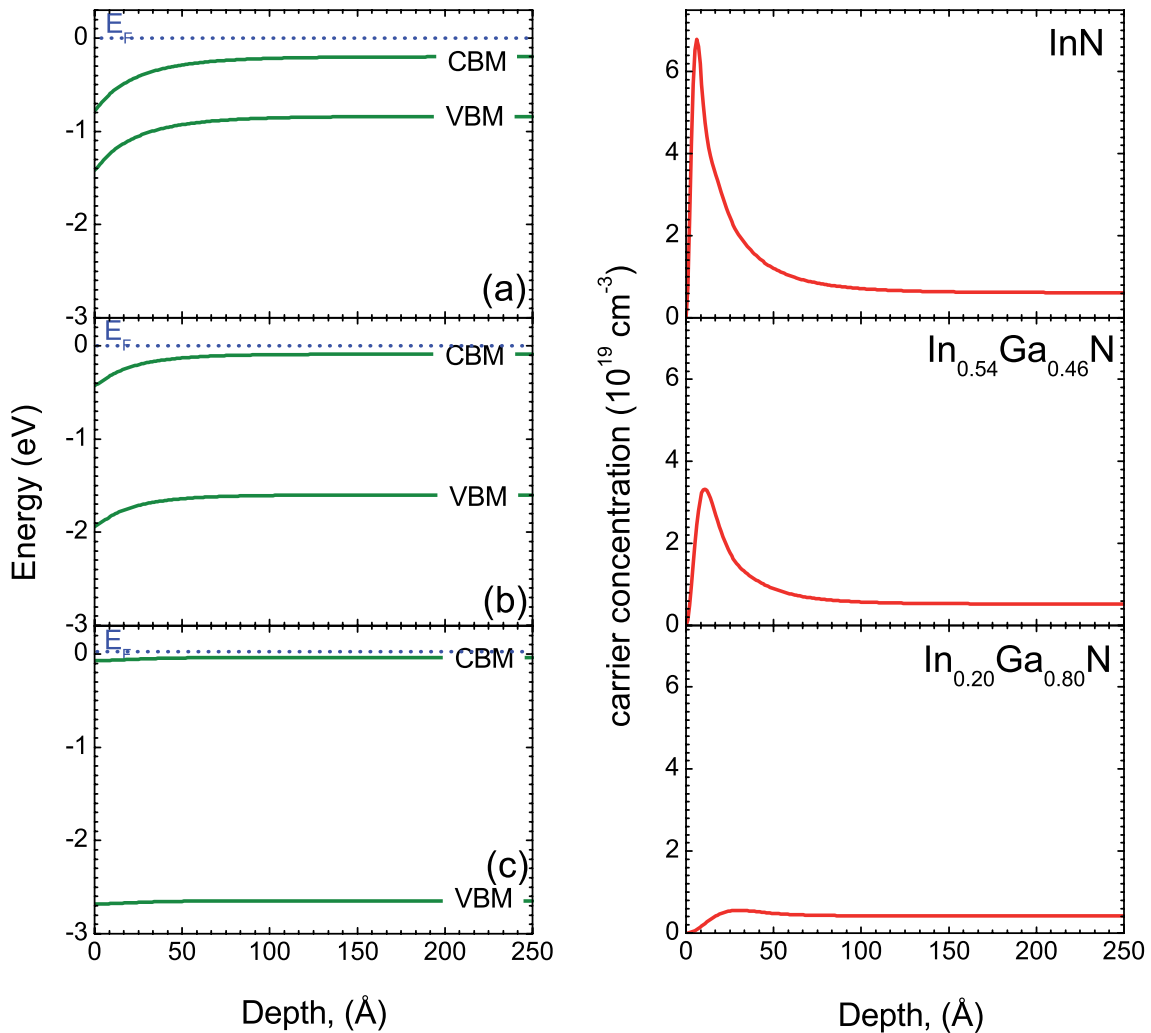


Figure 7.7: The conduction band minimum (CBM) and valence band maximum (VBM) positions with respect to the Fermi level, E_F , and carrier concentration as a function of depth from the surface for (a) InN, (b) $In_{0.54}Ga_{0.46}N$ and (c) $In_{0.20}Ga_{0.80}N$.

This procedure is described in Section 3.2 and refs [77] and [194]. Within these calculations, the electron effective mass at the CBM for InN and GaN was taken to be $0.045m_e$ and $0.20m_e$ respectively. Table 7.1 shows the estimated bulk Fermi level noindent positions increase with the fraction of Ga from 0.84 eV above the VBM for InN to 2.65 eV above the VBM for $In_{0.20}Ga_{0.80}N$.

Using Equation 7.1, where E_g^{GaN} , the band gap of GaN, equals 3.44 eV [55], E_g^{InN} , the band gap of InN, equals 0.64 eV [53] and b denotes the band gap bowing parameter of 1.7 eV [58], the band gap of $In_xGa_{1-x}N$ across the composition has been determined, and are also listed in Table 7.1. Following the empirical relationship $m_e^* \sim 0.07E_g$, the variation of band edge electron effective mass is assumed to be

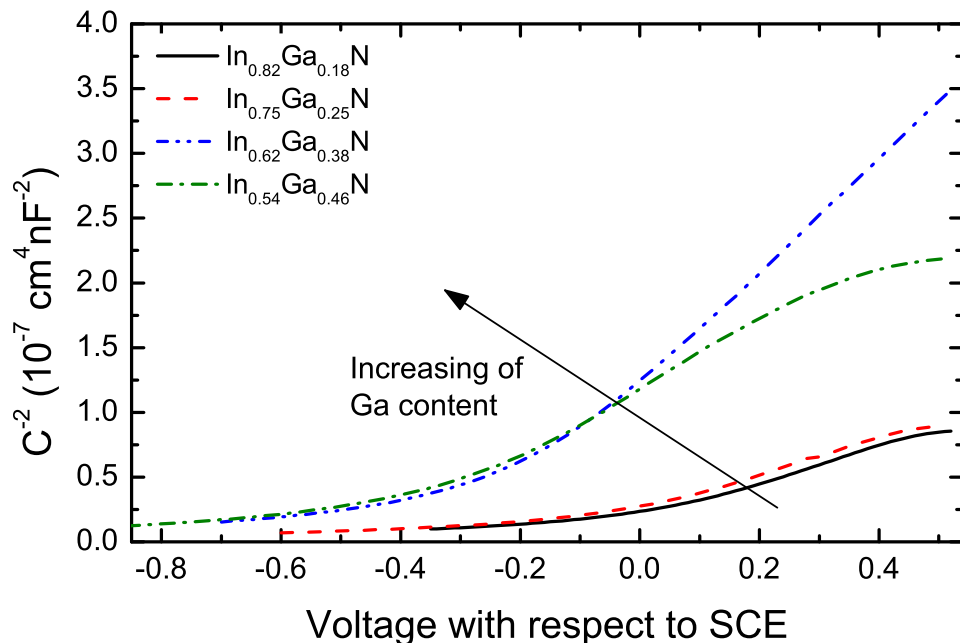


Figure 7.8: Mott-Schottky plot of capacitance-voltage data obtained from $\text{In}_x\text{Ga}_{1-x}\text{N}$ films using an electrolyte contact. The shallow gradient region at lower bias reflects depletion of the surface electron accumulation, whereas steeper gradient region at higher bias reflects a lower net space-charge in the bulk.

described by a bowing parameter $b_m = 0.07b$.

$$E_g^{\text{In}_x\text{Ga}_{1-x}\text{N}} = (1 - x)E_g^{\text{GaN}} + xE_g^{\text{InN}} - bx(1 - x) \quad (7.1)$$

The surface Fermi level is located above the bottom of the conduction band, indicating a downward band bending at the surface of all the $\text{In}_x\text{Ga}_{1-x}\text{N}$ samples presented in this chapter, see Table 7.1. The surface state densities were determined by solving Poisson's equation within the modified Thomas-Fermi approximation (MTFA). Details of these calculations are reported in Section 2.2. Figure 7.7 shows the band bending and carrier concentration profile for InN, $\text{In}_{0.54}\text{Ga}_{0.46}\text{N}$ and $\text{In}_{0.20}\text{Ga}_{0.80}\text{N}$. From Gauss's law, the surface sheet density (n_{ss}) can be calculated from the gradient of the band bending potential at the surface. With increasing Ga contents the n_{ss} continuously decreases and the values are shown in Table 7.1.

Capacitance-voltage data in the form of Mott-Schottky plots (C^{-2} vs. V) for selected $\text{In}_x\text{Ga}_{1-x}\text{N}$ films are shown in Figure 7.8. The positive slope and increasing experimental Mott-Schottky curves correspond to the electron-rich surface layer due to unoccupied surface donor states. The shallow gradient region at lower bias

reflects depletion of the surface electron accumulation, whereas steeper gradient region at higher bias reflects a lower net space-charge in the bulk. The magnitude of C^{-2} increases with increasing Ga content, indicating a reduction of the electron accumulation. The measurements were performed in the range of applied potential where current flow at the surface was not observed. This range approximately corresponds to the band gap of $\text{In}_x\text{Ga}_{1-x}\text{N}$ alloys.

7.4 Discussion

The barrier height (separation between the conduction band minimum (CBM) and the surface Fermi level), analogous to the Schottky barrier height of a metal/semiconductor contact has been determined from the valence band XPS spectra across a range of alloy composition and is shown in Figure 7.9. The barrier height is negative for In-rich $\text{In}_x\text{Ga}_{1-x}\text{N}$ alloys and almost zero for $\text{In}_{0.20}\text{Ga}_{80}\text{N}$, corresponding to the surface Fermi level lying above the CBM. The composition dependence of the barrier height is found by the least squares method to be $\Phi_B = 0.22 - 1.38x + 0.36x^2$ for $\text{In}_x\text{Ga}_{1-x}\text{N}$, suggesting the transition from electron accumulation to electron depletion at $x = 0.17$.

Figure 7.10 shows the VBM, CBM, and surface and bulk Fermi level as a function of composition referenced to the charge neutrality level (CNL). The CNL is the energy level denoting the boundary between surface states that are predominantly donor-like (below) and surface states that are predominantly acceptor like (above) [63]. The surface and bulk Fermi level positions of $\text{In}_x\text{Ga}_{1-x}\text{N}$ alloys with the composition $x \geq 0.40$ are located below the CNL indicating the existence of unoccupied donor like surface states, causing a downward bending of the bands relative to the Fermi level and an accumulation of electrons at the surface, in order to maintain charge neutrality. Additionally, the surface and bulk Fermi levels move closer together with increasing Ga content, providing a lowering of band bending from 0.58 eV to 0.15 eV and hence a reduction of electron accumulation at the surface. Further increasing the Ga fraction changes the position of surface Fermi level to be located above the CNL and causing some acceptor states to be occupied and

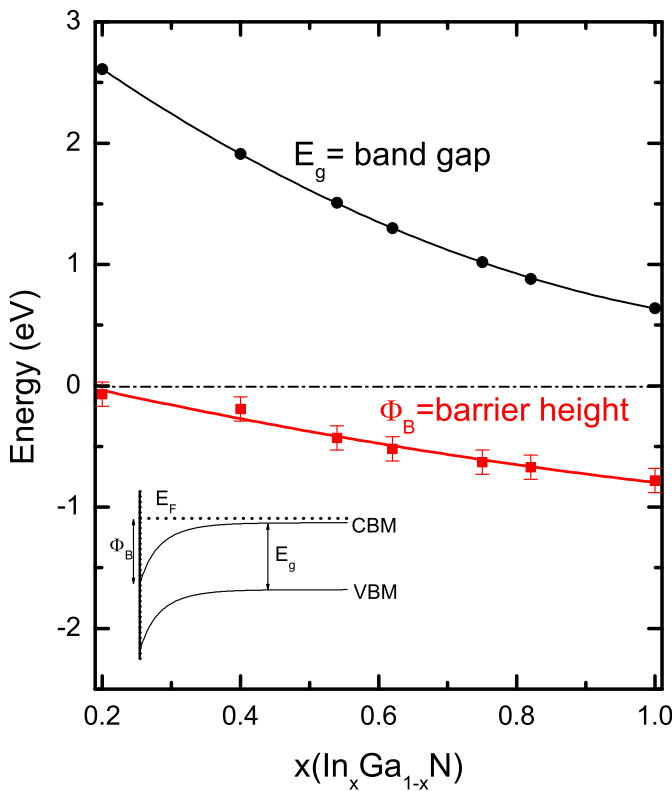


Figure 7.9: Variation of band gap and barrier height Φ_B (the separation between the Fermi level and CBM) at $\text{In}_x\text{Ga}_{1-x}\text{N}$ surfaces with varying In concentration x . The barrier heights are obtained by subtracting the position of the surface Fermi level from the band gap. The red solid line is a second order polynomial least squares fit to the Φ_B data points. The dot-dashed line indicates the zero of energy. Inset depicts the downward band bending.

hence indicating a surface electron depletion layer.

For the $\text{In}_{0.20}\text{Ga}_{0.80}\text{N}$ alloy, the surface Fermi level is located 0.44 eV above the CNL, suggesting a surface electron depletion layer. However, the bulk Fermi level for this alloy is situated slightly below the surface Fermi level, consequently the small downward band bending of 0.03 eV and a small surface accumulation layer should be present. Any uncertainty in the surface and bulk Fermi level positions will result in a wider range of possible surface sheet charge densities and within the error bars the surface and bulk Fermi levels could be located at the same position and consequently the presence of flat bands is highly probable. These results indicate that the transition from an accumulation layer of $\text{In}_x\text{Ga}_{1-x}\text{N}$ to a depletion layer at the surface will be at a composition slightly less than $x = 0.20$.

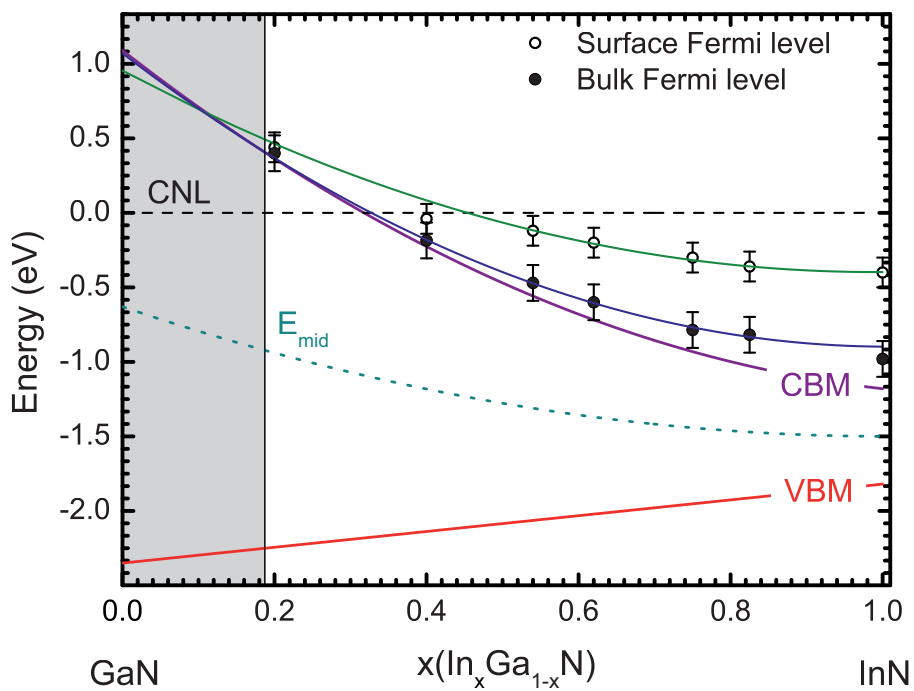


Figure 7.10: The CBM, VBM, and mid-gap position (E_{mid}) as a function of $In_x Ga_{1-x} N$ composition with respect to the charge neutrality level. The relative positions of the surface and bulk Fermi levels, determined by XPS and infrared reflection, are also shown as open and closed circles, respectively. The green (blue) line is a guide to the eye for the surface (bulk) Fermi level position.

7.5 Conclusions

In conclusion, XPS has been used to determine the Fermi level at the cleaned surfaces of MOCVD-grown $In_x Ga_{1-x} N$ alloys as a function of composition. Wet etching of $In_x Ga_{1-x} N$ in HCl successfully reduced the native oxides at the surface. The bulk Fermi levels have been determined by IR reflectivity measurements with simulations. A large electron accumulation has been observed for InN, consistent with previous observations [76, 77]. This was reduced with increasing Ga content for the In-rich alloys. A transition from electron accumulation layer to electron depletion layer was observed at $x \approx 0.20$. This transition has previously been reported to occur at $x = 0.43$ [27] and $x = 0.39$ [194] in undoped MBE grown alloys. The differences in this transition composition between different sets of samples are attributed to different unintentional bulk doping levels.

Chapter 8

General conclusions

This project has focused on the electronic properties of InN and $\text{In}_x\text{Ga}_{1-x}\text{N}$ thin films. In particular, a major focus has been on determining the properties of Mg-doped InN with a view to understanding and reproducibly achieving *p*-type material. Despite several claims in the literature, whether any InN samples have been produced that are really *p*-type is still an open question. Previously, published works on InN surfaces has consisted of both the discovery and explanation of the phenomena of electron accumulation and the quantised subband states observed [71, 72, 76, 79]. The associated inversion layer, thought to exist at the surface of *p*-type InN, is one of the factors that makes it difficult to determine whether InN is really *p*-type or not. This is a major challenge which needs to be overcome when characterizing Mg-doped InN samples. In order for InN to realise its potential in a variety of device applications, it is important for *p*-type doping to be reproducibly achieved and understood. Understanding the properties of *n*-type (both undoped and intentionally doped) InN and $\text{In}_x\text{Ga}_{1-x}\text{N}$ has also formed a vital part of the project.

In this thesis XPS, SIMS, IR reflectivity and ECV results on non-polar InN, Mg-doped InN and $\text{In}_x\text{Ga}_{1-x}\text{N}$ have been presented. The common feature for these materials is a presence of an electron accumulation near the surface, which in many cases is a major problem in the fabrication of *p-n* junctions. The existence of electron accumulation in all the materials can be explained by the extremely low conduction band minimum at the Brillouin Zone centre (Γ point). Consequently the CNL is typically located high in the conduction band and the surface Fermi level is pinned below the CNL, resulting in an electron accumulation layer [66]. Previously reported results showed a high electron sheet density of $1.6 \times 10^{13} \text{ cm}^{-2}$ near the surface [76, 106]. In this thesis the lower surface Fermi level and an associated lower electron accumulation near the surface in all non-polar InN films was found, much lower than

previously observed in undoped InN [76], and solutions of Poisson's equation gave a sheet density of accumulated electrons of $\sim 9.7 \times 10^{12} \text{ cm}^{-2}$. Moreover, the XPS core level analysis of In 3d and N 1s peaks indicates $\sim 1 \text{ ML}$ of In above the non-polar InN bulk-like termination in each case, significantly lower than found in a previous study of both *a*- and *c*-plane InN (3.0 ML and 3.4 ML, respectively) [164, 165]. This result is consistent with Segev and Van de Walle's theoretical predictions, where they suggested that microscopic origin of electron accumulation is In-In bonding within the In adlayers at the InN surface [81, 82, 163].

Using IR reflectivity, the bulk carrier concentration was found to be lower than previously observed in non-polar InN films [156]. This indicates that the quality of all measured *a*-plane and *m*-plane InN was significantly improved by the PAMBE growth process. Additionally, it has been shown that the increased carrier concentration toward the InN/GaN interface increases due to impurities (mainly oxygen), potentially located at basal-plane stacking faults. This was confirmed by SIMS measurements and IR reflectivity measurements, and these results correspond very well with the three layer model, proposed by King *et al.* [89]

In the case of *p*-type InN, the downward band bending at the surface is much more severe than for undoped InN. For *p*-type InN the bulk Fermi level is located near the VBM, hence one would expect the accumulation layer to be greater [207]. However, the studies of highly Mg-doped InN presented in this thesis show that high Mg concentrations dramatically lower the surface Fermi level and hence reduces a surface electron accumulation. This also increases the band bending, resulting in increased density of unoccupied donor surface states. This situation corresponds to a transition from an electron accumulation to hole depletion, where negatively charged surface donors are compensated by near-surface Mg acceptors and charge neutrality is maintained. This mechanism is different in *n*-type Si-doped InN, where the electron accumulation near the surface is decreased due to a saturation of both the bulk and surface Fermi levels at the CNL, producing flat bands and maintaining charge neutrality [66, 185]. Additionally, Si increases the electron concentration in the bulk of InN, whereas Mg produces *p*-type conductivity, however, the *p*-type

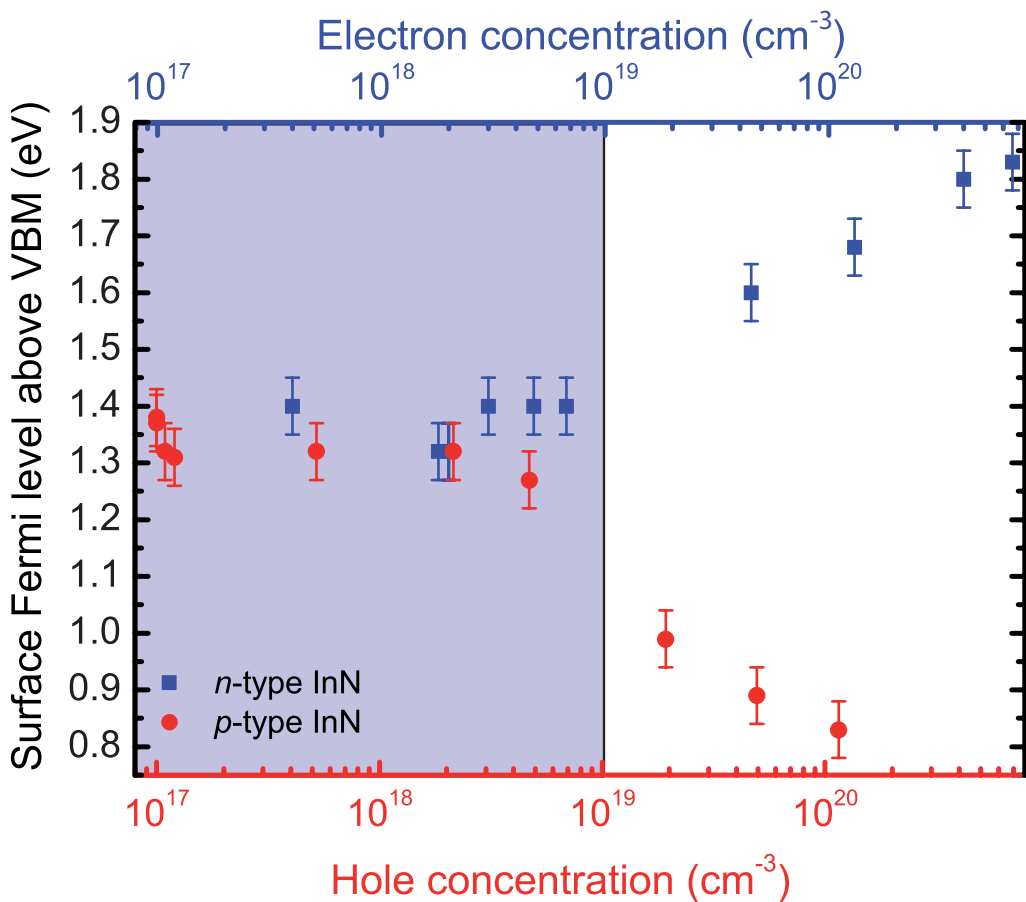


Figure 8.1: Surface Fermi level position of *n*-type (squares) and *p*-type (circles) InN as a function of carrier concentration.

region is buried beneath the *n*-type surface. Moreover, within the assumptions presented in this thesis, a carrier concentration of $\sim 1.9 \times 10^{19} \text{ cm}^{-3}$ is likely the cross-over point above which the surface Fermi level tends to reduce the electron accumulation (see Figure 8.1).

Because a small amount of surface electron accumulation still existed in highly Mg doped InN, and the sign of the Hall coefficient suggested the films are still *n*-type, additional chemical treatment was performed to further reduce undesirable electron density at the surface. To obtain this, the films were treated in $(\text{NH}_4)_2\text{S}_x$. This method has previously been used to passivate the surface of InAs [111–113] GaN [190] and InN [106, 107], however in the case of undoped InN complete reduction of electron accumulation was not achieved [106, 107]. Chapter 6 shows that the presence of sulfur at the surface can shift the position of the surface Fermi level to a lower energy, due to a transfer of charge from the InN to the more electronegative

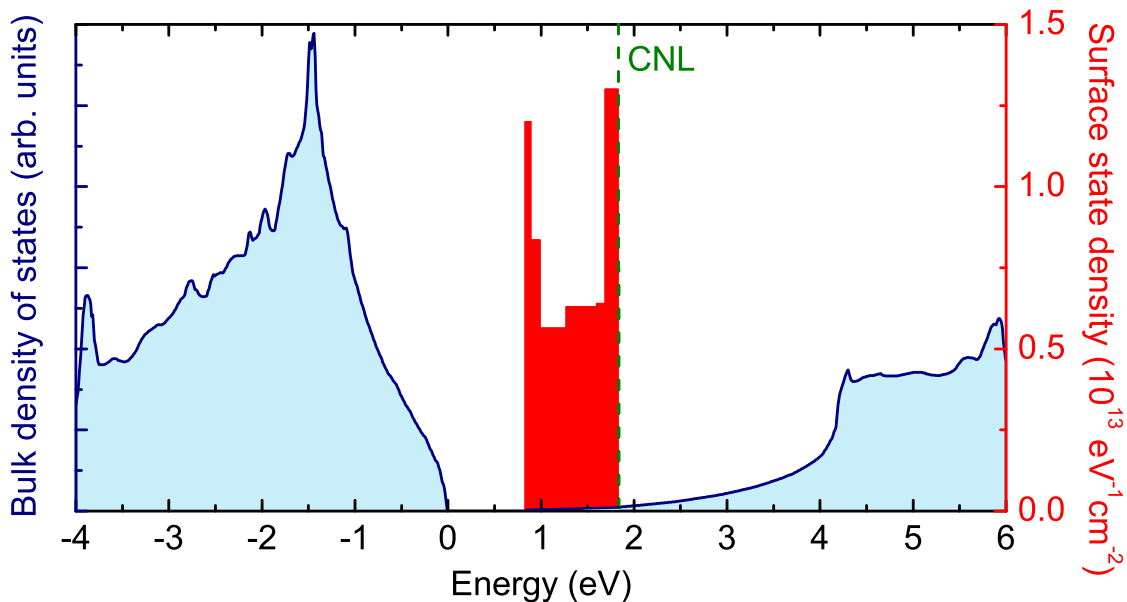


Figure 8.2: Surface state density (red histogram) evaluated by numerically solving Poisson’s equation within MTFA as described in Chapter 2.2 and bulk DOS (blue line) for the (0001) InN calculated by F. Bechstedt’s group [148], using quasiparticle-corrected density-functional theory (QPC-DFT).

sulfur via the breaking of In-In bonds in the In adlayer. This shift was much smaller than previously observed in undoped InN [106, 191], but the overall reduction of the accumulated electron sheet density was much higher $\sim 70\%$ (compared to $\sim 30\%$ for undoped InN [106]). This phenomena is explained by the shape of the distribution of the donor surface state density (see Figure 8.2) where the position of the surface Fermi level plays the important role.

Band bending and the related surface electron accumulation was also observed in MOCVD grown $\text{In}_x\text{Ga}_{1-x}\text{N}$ samples above $x \approx 0.20$. The surface electron accumulation decreases with increasing Ga content, and the transition from an electron accumulation to a depletion layer was observed at $x \approx 0.20$. This transition was previously reported to occur at $x = 0.43$ [27] and $x = 0.39$ [194], however previous results were obtained on oxidized MBE grown alloys. Here, the wet etching in HCl and annealing *in vacuo* was used, successfully reducing the native oxide on the surface of $\text{In}_x\text{Ga}_{1-x}\text{N}$. A reduction of the oxide layer greater than 75% in all $\text{In}_x\text{Ga}_{1-x}\text{N}$ alloys was achieved. Additionally, the differences in this transition composition between different sets of samples are attributed to different unintentional

bulk doping levels.

Electrochemical capacitance-voltage (ECV) profiling is a very useful technique to determine electronic properties of semiconductor materials with an electron depletion region near the surface. However, for InN this is complicated by the presence of an electron accumulation layer. Therefore, modelling of the ECV curves (called Mott-Schottky plots) is necessary. The ECV results presented in Chapter 4 show that the electron accumulation model, based on Poisson's equation, also reproduces the experimental. Moreover, some parameters obtained from XPS and IR reflectivity measurements were used in ECV modelling, indicating that this technique is powerful and complementary to XPS and IR reflectivity. The surface quality plays a very important role in ECV measurements. Surface roughness might have a huge impact on the measured capacitance, providing a discrepancy between modelled and experimental curves. The modelling of *p*-type InN Mott-Schottky curves would give more accurate information about this material, however an inversion layer model makes these calculations much more complicated.

Appendix A

Perturbation theory

For $\mathbf{k} \cdot \mathbf{p}$ theory it is necessary to introduce some elementary results of time-independent perturbation theory. The $\mathbf{k} \cdot \mathbf{p}$ equation is obtained from the one electron Schrödinger equation

$$H_{1e}^{(0)} |n\rangle = E_n^{(0)} |n\rangle, \quad (\text{A.1})$$

where $|n\rangle$ and $E_n^{(0)}$ are the eigenfunctions and eigenvalues, respectively. Let us now denote a new Hamiltonian by $H' = H^{(0)} + W$, where W is the perturbation. For the non-degenerate eigenvalues, the first order energy correction at $\mathbf{k}=\mathbf{0}$ is given by

$$\Delta E_n^{(1)} \approx \langle n | W | n \rangle, \quad (\text{A.2})$$

and this determines the diagonal matrix element of the perturbing potential. The second order correction at $\mathbf{k}=\mathbf{0}$ comes from non-diagonal terms and it is given by

$$\Delta E_n^{(2)} \approx \sum_{m \neq n} \frac{|\langle n | W | m \rangle|^2}{E_n^{(0)} - E_m^{(0)}}. \quad (\text{A.3})$$

Thus, the total perturbed energy is given by

$$E_n \approx E_n^{(0)} + \langle n | W | n \rangle + \sum_{m \neq n} \frac{|\langle n | W | m \rangle|^2}{E_n^{(0)} - E_m^{(0)}}. \quad (\text{A.4})$$

The second order perturbation, $\Delta E_n^{(2)}$ denotes the interaction between different eigenvalues. Whether the interaction between states exist or not is determined by the matrix elements $\langle n | W | m \rangle$ and this can be inferred by invoking the symmetry properties of the eigenfunctions.

A.1 Symmetry

The atoms in III-V semiconductors are tetrahedrally bonded as a consequence of sp^3 hybridization. The individual atoms have valence electrons located in s - and p -type

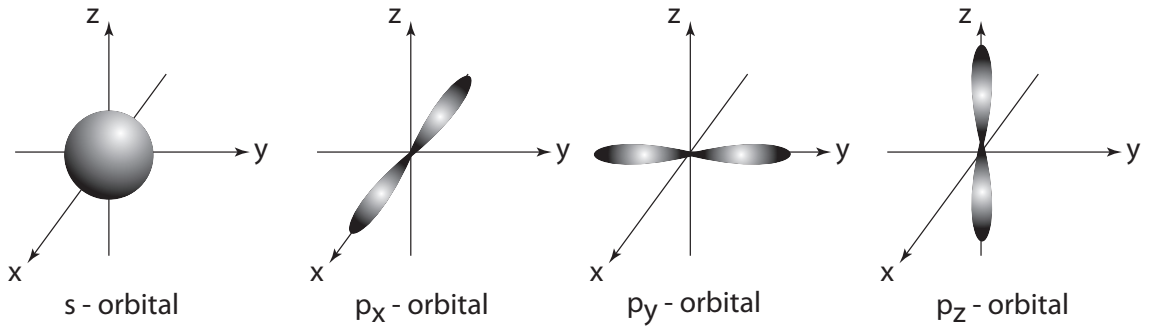


Figure A.1: A schematic representation of s - and p -orbitals. The s -orbital is spherical, and hence symmetric along all axes. The p -orbitals are antisymmetric or odd along the direction they are oriented.

orbitals. The symmetry of these orbitals is depicted in Figure A.1 and described by the following equations

$$s = 1, \quad (\text{A.5a})$$

$$p_x = \frac{x}{r} = \sqrt{3}\sin\theta\cos\phi, \quad (\text{A.5b})$$

$$p_y = \frac{y}{r} = \sqrt{3}\sin\theta\sin\phi, \quad (\text{A.5c})$$

$$p_z = \frac{z}{r} = \sqrt{3}\cos\theta, \quad (\text{A.5d})$$

where r , θ and ϕ are spherical coordinates. For direct-gap semiconductors, the states near the conduction band minimum possess s -type character. In other words, they have spherical symmetry, whereas the states near the valence band maxima have the symmetry of p -orbitals. Therefore the valence band states may be described by a set of Kramers-conjugate pairs of states [208], representing the basis of coupled angular momenta

$$u_{HH,\uparrow} = -\frac{1}{\sqrt{2}}(u_x + iu_y), \quad (\text{A.6a})$$

$$u_{HH,\downarrow} = \frac{1}{\sqrt{2}}(\bar{u}_x - i\bar{u}_y), \quad (\text{A.6b})$$

$$u_{LH,\uparrow} = -\frac{1}{\sqrt{6}}(\bar{u}_x + i\bar{u}_y - 2u_z), \quad (\text{A.6c})$$

$$u_{LH,\downarrow} = \frac{1}{\sqrt{6}}(u_x - iu_y + 2\bar{u}_z), \quad (\text{A.6d})$$

$$u_{SO,\uparrow} = -\frac{1}{\sqrt{3}}(\bar{u}_x + i\bar{u}_y + u_z), \quad (\text{A.6e})$$

$$u_{SO,\downarrow} = \frac{1}{\sqrt{3}}(u_x - iu_y - \bar{u}_z), \quad (\text{A.6f})$$

where u_s , u_x , u_y , u_z are the Bloch functions that possess the symmetry of the s -, p_x -, p_y - p_z -type orbitals, respectively.

A.2 $\mathbf{k} \cdot \mathbf{p}$ theory with no spin-orbit interaction

The $\mathbf{k} \cdot \mathbf{p}$ method can be obtained from the one-electron Schrödinger equation given by

$$H_{1e}\psi_\nu(\mathbf{r}) = \left(\frac{p^2}{2m_0} + V(\mathbf{r}) \right) \psi_\nu(\mathbf{r}) = E_\nu \psi_\nu(\mathbf{r}), \quad (\text{A.7})$$

where H_{1e} , $\psi_\nu(\mathbf{r})$ and E_ν denote the one-electron Hamiltonian, the wavefunction and energy of an electron in an eigenstate labeled by ν . Using Bloch's theorem the solutions of A.7 can be expressed as

$$\psi_{\nu\mathbf{k}} = \exp(i\mathbf{k} \cdot \mathbf{r}) u_{\nu\mathbf{k}}(\mathbf{r}), \quad (\text{A.8})$$

where ν is the band index, \mathbf{k} lies within the first Brillouin zone, and $u_{\nu\mathbf{k}}$ has the periodicity of the lattice. Substituting the Bloch function into (A.7) we obtain an equation in $u_{n\mathbf{k}}$ of the form

$$\left(\frac{p^2}{2m_0} + \frac{\hbar\mathbf{k} \cdot \mathbf{p}}{m_0} + \frac{\hbar^2 k^2}{2m_0} + V \right) u_{\nu\mathbf{k}} = E_{\nu\mathbf{k}} u_{\nu\mathbf{k}} \quad (\text{A.9})$$

In the case without spin-orbit interaction, the three valence bands are degenerate at $\mathbf{k}=0$. This situation is presented in Figure A.2. At $\mathbf{k}=0$ the solutions of equation (A.7) form a complete and orthonormal set of basis functions. Assuming that these solutions are known and using the standard perturbation theory, the eigenvalues $E_{\nu\mathbf{k}}$ at a neighboring point \mathbf{k} can be expressed as

$$E_{\nu\mathbf{k}} = E_{\nu\mathbf{0}} + \frac{\hbar^2 k^2}{2m_0} + \frac{\hbar^2}{m_0^2} \sum_{\nu' \neq \nu} \frac{|\langle u_{\nu\mathbf{0}} | \mathbf{k} \cdot \mathbf{p} | u_{\nu'\mathbf{0}} \rangle|^2}{E_{\nu\mathbf{0}} - E_{\nu'\mathbf{0}}} \quad (\text{A.10})$$

It is conventional to express the energy $E_{\nu\mathbf{k}}$, for small values of k , as

$$E_{\nu\mathbf{k}} = E_{\nu\mathbf{0}} + \frac{\hbar^2 k^2}{2m_0^*}, \quad (\text{A.11})$$

where m_0^* is defined as the effective mass of the band and is given by

$$\frac{1}{m_0^*} = \frac{1}{m_0} + \frac{2}{m_0 k^2} \sum_{\nu' \neq \nu} \frac{|\langle u_{\nu\mathbf{0}} | \mathbf{k} \cdot \mathbf{p} | u_{\nu'\mathbf{0}} \rangle|^2}{E_{\nu\mathbf{0}} - E_{\nu'\mathbf{0}}}. \quad (\text{A.12})$$

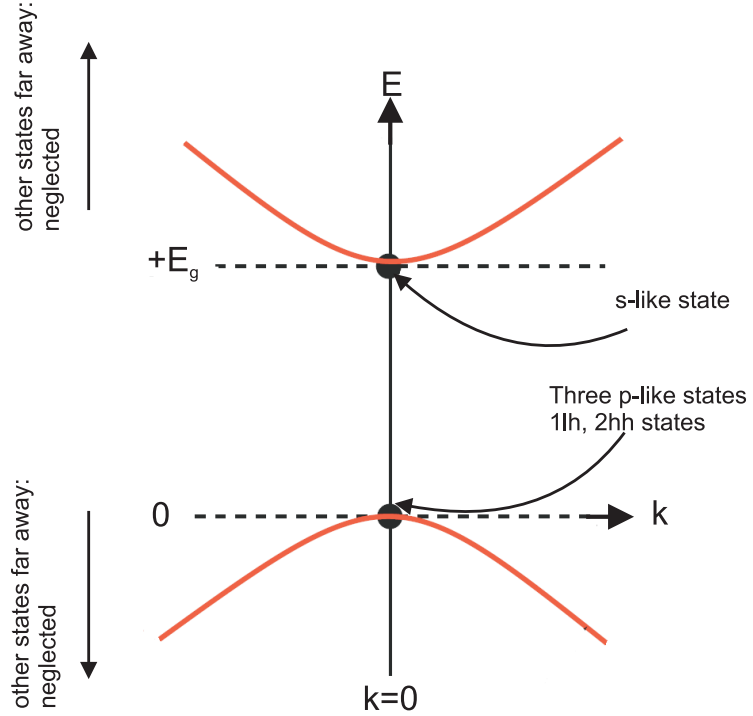


Figure A.2: A schematic representation of $k \cdot p$ band structure around $k=0$ for the semiconductor with a direct band gap without spin-orbit coupling. The valence band states are a linear combination of p -type orbitals, whereas the conduction band has s -type character.

Using the equations (A.6a)-(A.6f), and the relations

$$\langle u_s | p_i | u_i \rangle \equiv P \text{ for } i = x, y, z \quad (\text{A.13a})$$

$$\langle u_s | p_i | u_j \rangle \equiv 0 \text{ for } i \neq j \quad (\text{A.13b})$$

the conduction band effective mass can be presented as

$$\frac{1}{m_0^*} = \frac{1}{m_0} \left(1 + \frac{2}{m_0 k^2} \left[\frac{k^2 P^2}{2E_g} + \frac{k^2 P^2}{6E_g} + \frac{k^2 P^2}{3E_g} \right] \right) \quad (\text{A.14})$$

and hence

$$m_0^* = \frac{m_0}{1 + \frac{2P^2}{m_0 E_g}}. \quad (\text{A.15})$$

In the presence of spin-orbit interactions, the three degenerate valence bands at $\mathbf{k}=0$ are split into a degenerate heavy hole (hh), light hole (lh) states and split-off (SO) state separated by the spin-orbit splitting energy (Δ_{so}) as shown in Figure A.3. In this case the conduction band effective mass is given by

$$\frac{1}{m_0^*} = \frac{1}{m_0} \left(1 + \frac{2}{m_0 k^2} \left[\frac{k^2 P^2}{2E_g} + \frac{k^2 P^2}{6E_g} + \frac{k^2 P^2}{3(E_g + \Delta_{so})} \right] \right) \quad (\text{A.16})$$

which can be rewritten as

$$m_0^* = \frac{m_0}{1 + \frac{2P^2}{3m_0} \left(\frac{2}{E_g} + \frac{1}{E_g + \Delta_{SO}} \right)}. \quad (\text{A.17})$$

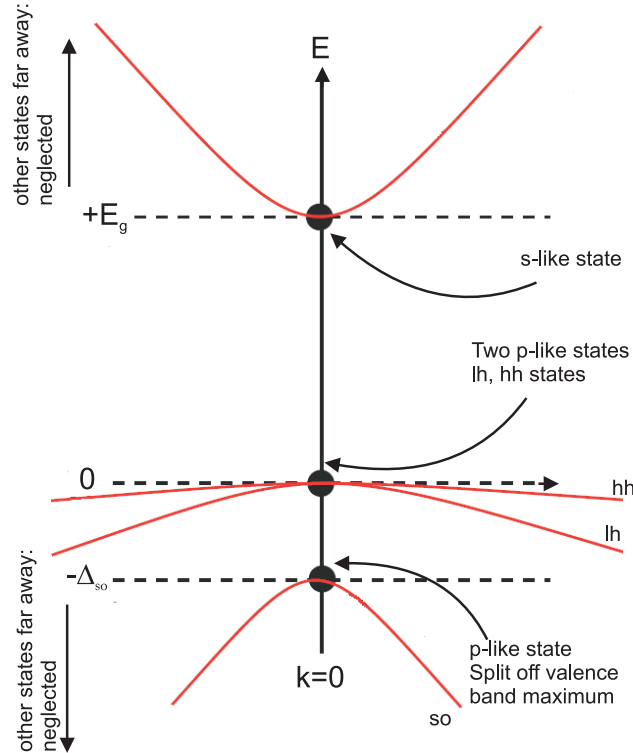


Figure A.3: A schematic representation of $k \cdot p$ band structure around $k=0$ for the semiconductor with a direct band gap with spin-orbit coupling. The valence band states are a linear combination of p-type orbitals, whereas the conduction band has s-type character.

Appendix B

Optical phonon parameters for Al₂O₃

Optical phonon parameters used in the infrared reflectivity simulations of sapphire are presented in Table B.1.

j	$\varepsilon(\infty)$	ω_{LO} (cm ⁻¹)	γ_{LO} (cm ⁻¹)	ω_{TO} (cm ⁻¹)	γ_{TO} (cm ⁻¹)
<i>E</i> ₁					
1	3.05 (± 0.07)	387.57 (± 0.1)	2.8 (± 0.3)	385.15 (± 0.2)	2.7 (± 0.4)
2		481.57 (± 0.06)	2.1 (± 0.1)	439.48 (± 0.4)	3.1 (± 0.7)
3		629.90 (± 0.3)	6.5 (± 0.5)	569.07 (± 0.4)	4.5 (± 0.9)
4		906.5 (± 0.9)	19.3 (± 1.0)	634.18 (± 0.3)	4.9 (± 0.5)
<i>A</i> ₁					
1	3.04 (± 0.03)	510.90 (± 0.04)	1.2 (± 0.07)	397.22 (± 0.5)	1.5 (± 0.9)
2		878.62 (± 0.5)	19.2 (± 1.1)	583.04 (± 0.3)	1.5 (± 0.6)

Table B.1: Optical phonon parameters for sapphire at room temperature. Taken from [209]

Bibliography

- [1] V. W. L. Chin, T. L. Tansley, and T. Osotchan, *J. Appl. Phys.* **75**, 7365 (1994)
- [2] V. M. Polyakov and F. Schwierz, *Appl. Phys. Lett.* **88**, 032101 (2006)
- [3] V. M. Polyakov and F. Schwierz, *J. Appl. Phys.* **99**, 113705 (2006)
- [4] V. Y. Davydov, A. A. Klochikhin, R. P. Seisyan, V. V. Emtsev, S. V. Ivanov, F. Bechstedt, J. Furthmüller, H. Harima, A. V. Mudryi, J. Aderhold, O. Semchinova, and J. Graul, *Phys. Stat. Sol. B* **229**, R1 (2002)
- [5] J. Wu, W. Walukiewicz, K. M. Yu, J. W. Ager III, E. E. Haller, H. Lu, W. J. Schaff, Y. Saito, and Y. Nanishi, *Appl. Phys. Lett.* **80**, 3967 (2002)
- [6] W. Walukiewicz, J. W. Ager III, K. M. Yu, Z. Liliental-Weber, J. Wu, S. X. Li, R. E. Jones, and J. D. Denlinger, *J. Phys. D: Appl. Phys.* **39**, R83 (2006)
- [7] E. Matioli, C. Neufeld, M. Iza, S. C. Cruz, A. A. Al-Heji, X. Chen, R. M. Farrell, S. Keller, S. DenBaars, U. Mishra, S. Nakamura, J. Speck, and C. Weisbuch, *Appl. Phys. Lett.* **98**, 021102 (2011)
- [8] X. Chen, K. D. Matthews, D. Hao, W. J. Schaff, and L. F. Eastman, *Phys. Stat. Sol. A* **205**, 1103 (2008)
- [9] J.-K. Sheu, C.-C. Yang, S.-J. Tu, K.-H. Chang, M.-L. Lee, W.-C. Lai, and L.-C. Peng, *Elect. Dev. Lett.* **30**, 225 (2009)
- [10] L. Hsu and W. Walukiewicz, *J. Appl. Phys.* **104**, 024507 (2008)
- [11] G. W. Crabtree and N. S. Lewis, *Physics Today* **3**, 37 (2007)
- [12] D. Ginley, *MRS Bulletin* **33**, 355 (2008)
- [13] D. V. Shenai-Khatkhate, R. J. Goyette, R. L. DiCarlo, and G. Dripps, *J. Cryst. Growth.* **272**, 816 (2004)

- [14] J. Wu, W. Walukiewicz, K. M. Yu, J. W. Ager III, E. E. Haller, H. Lu, and W. J. Schaff, *Appl. Phys. Lett.* **80**, 4741 (2002)
- [15] R. Goldhahn, J. Scheiner, S. Shokhovets, T. Frey, U. Khler, D. As, and K. Lischka, *Phys. Stat. Sol. b* **216**, 265 (1999)
- [16] T. Onuma, S. F. Chichibu, Y. Uchinuma, T. Sota, S. Yamaguchi, S. Kamiyama, H. Amano, and I. Akasaki, *J. Appl. Phys.* **94**, 2449 (2003)
- [17] R. E. Jones, R. Broesler, K. M. Yu, J. W. Ager III, E. E. Haller, W. Walukiewicz, X. Chen, and W. J. Schaff, *J. Appl. Phys.* **104**, 123501 (2008)
- [18] M. Ikeda and S. Uchida, *Phys. Stat. Sol. (a)* **194**, 407 (2002)
- [19] H. Y. Ryu, K. H. Ha, S. N. Lee, T. Jang, H. K. Kim, J. H. Chae, K. S. Kim, K. K. Choi, J. K. Son, H. S. Paek, Y. J. Sung, T. Sakong, O. H. Nam, and Y. J. Park, *Appl. Phys. Lett.* **89**, 031122 (2006)
- [20] T. Miyoshi, S. Masui, T. Okada, T. Yanamoto, T. Kozaki, S. Nagahama, and T. Mukai, *Appl. Phys. Express* **2**, 062201 (2009)
- [21] A. Khan, *Nature Photonics* **3**, 432 (2009)
- [22] W. Walukiewicz, K. M. Yu, J. W. Ager III, R. E. Jones, and N. Miller, *Electronic properties of InN and InGaN: Defects and doping in Indium Nitride and Related Alloys*, by T. D. Veal, C. F. McConville and W. J. Shaff (Eds) (CRC Press, 2009) pp. 377–417
- [23] R. Pengelly, S. Sheppard, T. Smith, B. Pribble, S. Wood, and C. Platis, in *Commercial GaN Devices For Switching and Low Noise Applications* (CS MANTECH Conference, May 16th-19th, 2011, Palm Springs, California, USA)
- [24] Y. F. Ng, Y. G. Cao, M. H. Xie, X. L. Wang, and S. Y. Tong, *Appl. Phys. Lett.* **81**, 3960 (2002)
- [25] F.-H. Yang, Jih-Shang, Hwang, K.-H. Chen, Y.-J. Yang, T.-H. Lee, L.-G. Hwa, and L.-C. Chen, *Thin Solid Films* **405**, 194 (2002)

- [26] R. E. Jones, K. M. Yu, S. X. Li, W. Walukiewicz, J. W. Ager III, E. E. Haller, H. Lu, and W. J. Schaff, Phys. Rev. Lett. **96**, 125505 (2006)
- [27] P. D. C. King, T. D. Veal, H. Lu, P. H. Jefferson, S. A. Hatfield, W. J. Schaff, and C. F. McConville, Phys. Stat. Sol. B **245**, 881 (2008)
- [28] P. D. C. King, T. D. Veal, P. H. Jefferson, C. F. McConville, H. Lu, and W. J. Schaff, Phys. Rev. B **75**, 115312 (2007)
- [29] H. Lu, W. J. Schaff, and L. F. Eastman, J. Appl. Phys. **96**, 3577 (2004)
- [30] R. Ascázubi, I. Wilke, K. Denniston, H. Lu, and W. J. Schaff, Appl. Phys. Lett. **84**, 4810 (2004)
- [31] H. Ahn, Y.-J. Yeh, Y.-L. Hong, and S. Gwo, Appl. Phys. Lett. **95**, 232104 (2009)
- [32] G. Xu, Y. J. Ding, H. Zhao, G. Liu, M. Jamil, N. Tansu, L. B. Zotova, C. E. Stutz, D. E. Diggs, N. Fernelius, F. K. Hopkins, C. S. Gallinat, G. Koblmüller, and J. S. Speck, Semicond. Sci. Technol. **25**, 015004 (2010)
- [33] C.-L. Hsiao, T.-W. Liu, C.-T. Wu, H.-C. Hsu, G.-M. Hsu, L.-C. Chen, W.-Y. Shiao, C. C. Yang, A. Gllstrm, P.-O. Holtz, C.-C. Chen, and K.-H. Chen, Appl. Phys. Lett. **92**, 111914 (2008)
- [34] D. Fritsch, H. Schmidt, and M. Grundmann, Phys. Rev. B **69**, 165204 (2004)
- [35] M. Briki, A. Zaoui, F. Boudaiba, and M. Ferhat, Appl. Phys. Lett. **91**, 182105 (2007)
- [36] P. Specht, J. Ho, X. Xu, R. Armitage, E. Weber, E. Erni, and C. Kisielowski, J. Cryst. Growth **288**, 225 (2006)
- [37] E. S. Hellman, MRS Internet J. Nitride Semicond. Res. **3**, 11 (1998)
- [38] T. D. Veal, P. D. C. King, P. H. Jefferson, L. F. J. Piper, C. F. McConville, H. Lu, W. J. Schaff, P. A. Anderson, S. M. Durbin, D. Muto, H. Naoi, and Y. Nanishi, Phys. Rev. B **76**, 075313 (2007)

- [39] J. Bhattacharyya, S. Ghosh, M. R. Gokhale, B. M. Arora, H. Lu, and W. J. Schaff, *Appl. Phys. Lett.* **89**, 151910 (2006)
- [40] V. Darakchieva, M.-Y. Xie, N. Franco, F. Giuliani, B. Nunes, E. Alves, C. L. Hsiao, L. C. Chen, T. Yamaguchi, Y. Takagi, K. Kawashima, and Y. Nanishi, *J. Appl. Phys.* **108**, 073529 (2010)
- [41] K. Wang, T. Yamaguchi, A. Takeda, T. Kimura, K. Kawashima, T. Araki, and Y. Nanishi, *Phys. Stat. Sol. A* **207**, 1356 (2010)
- [42] I. L. Guy, Z. Zheng, M. Wintrebert-Fouquet, K. S. A. Butcher, P. Chen, and T. L. Tansley, *J. Cryst Growth* **269**, 72 (2004)
- [43] M. Wintrebert-Fouquet, K. S. A. Butcher, I. L. Guy, and Z. Zheng, *Thin Solid Films* **516**, 7267 (2008)
- [44] Z. Li, B. Zhang, J. Wang, J. Liu, X. Liu, S. Yang, Q. Zhu, and Z. Wang, *Nanoscale Research Lett.* **6**, 193 (2011)
- [45] J. J. Hovel, H. J. nad Cuomo, *Appl. Phys. Lett.* **20**, 71 (1972)
- [46] J. W. Trainor and K. Rose, *J. Electron. Mater.* **3**, 821 (1974)
- [47] K. Osamura, K. Nakajima, and Y. Murakami, *Solid State Commun.* **11**, 617 (1972)
- [48] N. Puychevrier and M. Menoret, *Thin Solid Films* **36**, 141 (1976)
- [49] T. L. Tansley and C. P. Foley, *J. Appl. Phys.* **59**, 3241 (1986)
- [50] J. Wu, W. Walukiewicz, S. X. Li, R. Armitage, J. C. Ho, E. R. Weber, E. E. Haller, H. Lu, W. J. Schaff, A. Barcz, and R. Jakielka, *Appl. Phys. Lett.* **84**, 2805 (2004)
- [51] V. Davydov, A. Klochikhin, V. Emtsev, S. Ivanov, V. Vekshin, F. Bechstedt, J. Furthmüller, H. Harima, A. Mudryi, A. Hashimoto, A. Yamamoto, J. Aderhold, J. Graul, and E. Haller, *Phys. Stat. Sol. B* **230**, R4 (2002)

- [52] F. Bechstedt and J. Furthmüller, *J. Cryst. Growth* **246**, 315 (2002)
- [53] J. Wu, W. Walukiewicz, W. Shan, K. M. Yu, J. W. Ager III, S. X. Li, E. E. Haller, H. Lu, and W. J. Schaff, *J. Appl. Phys.* **94**, 4457 (2003)
- [54] S.-H. Wei and A. Zunger, *Phys. Rev. B* **60**, 5404 (1999)
- [55] I. Vurgaftman and J. R. Meyer, *J. Appl. Phys.* **94**, 3675 (2003)
- [56] J. Furthmüller, P. H. Hahn, F. Fuchs, and F. Bechstedt, *Phys. Rev. B* **72**, 205106 (2005)
- [57] F. Fuchs, J. Furthmüller, F. Bechstedt, M. Shishkin, and G. Kresse, *Phys. Rev. B* **76**, 115109 (2007)
- [58] P. Schley, R. Goldhahn, A. T. Winzer, G. Gobsch, V. Cimalla, O. Ambacher, H. Lu, W. J. Schaff, M. Kurouchi, Y. Nanishi, M. Rakel, C. Cobet, and N. Esser, *Phys. Rev. B* **75**, 205204 (2007)
- [59] P. G. Moses and C. G. Van de Walle, *Appl. Phys. Lett.* **96**, 021908 (2010)
- [60] M. D. McCluskey, C. G. Van de Walle, L. T. Romano, B. S. Krusor, and N. M. Johnson, *J. Appl. Phys.* **93**, 4340 (2003)
- [61] T. I., *Physikalische Zeitschrift der Sowjetunion* **1**, 733 (1932)
- [62] H. V., *Phys. Rev. B* **138**, A1689 (1965)
- [63] W. Mönch, *Semiconductor Surfaces and Interfaces* (Springer, Berlin, 2001)
- [64] J. Tersoff, *Phys. Rev. Lett.* **52**, 465 (1984)
- [65] W. Mönch, *Electronic Properties of Semiconductor Interfaces* (Springer, 2003)
- [66] P. D. C. King, T. D. Veal, P. H. Jefferson, S. A. Hatfield, L. F. J. Piper, C. F. McConville, F. Fuchs, J. Furthmüller, F. Bechstedt, H. Lu, and W. J. Schaff, *Phys. Rev. B* **77**, 045316 (2008)
- [67] I. Vurgaftman, J. R. Meyer, and L. R. Ram-Mohan, *J. Appl. Phys.* **89**, 5815 (2001)

- [68] P. D. C. King, T. D. Veal, P. H. Jefferson, C. F. McConville, T. Wang, P. J. Parbrook, H. Lu, and W. J. Schaff, *Appl. Phys. Lett.* **90**, 132105 (2007)
- [69] P. D. C. King, T. D. Veal, C. E. Kendrick, L. R. Bailey, S. M. Durbin, and C. F. McConville, *Phys. Rev. B* **78**, 033308 (2008)
- [70] H. Lu, W. J. Schaff, L. F. Eastman, and C. E. Stutz, *Appl. Phys. Lett.* **82**, 1736 (2003)
- [71] I. Mahboob, T. D. Veal, C. F. McConville, H. Lu, and W. J. Schaff, *Phys. Rev. Lett.* **92**, 036804 (2004)
- [72] I. Mahboob, T. D. Veal, L. F. J. Piper, C. F. McConville, H. Lu, W. J. Schaff, J. Furthmüller, and F. Bechstedt, *Phys. Rev. B* **69**, 201307 (2004)
- [73] M. Noguchi, K. Hirakawa, and T. Ikoma, *Phys. Rev. Lett.* **66**, 2243 (1991)
- [74] L. Colakerol, T. D. Veal, H. Jeong, L. Plucinski, A. DeMasi, T. Learmonth, P.-A. Glans, S. Wang, Y. Zhang, L. F. J. Piper, P. H. Jefferson, A. Fedorov, T. C. Chen, T. D. Moustakas, C. F. McConville, and K. E. Smith, *Phys. Rev. Lett.* **97**, 237601 (2006)
- [75] T. D. Veal, L. F. J. Piper, M. R. Phillips, M. H. Zareie, H. Lu, W. J. Schaff, and C. F. McConville, *Phys. Stat. Sol. A* **204**, 536 (2007)
- [76] P. D. C. King, T. D. Veal, C. F. McConville, F. Fuchs, J. Furthmüller, F. Bechstedt, P. Schley, R. Goldhahn, J. Schörmann, D. J. As, K. Lischka, D. Muto, H. Naoi, Y. Nanishi, H. Lu, and W. J. Schaff, *Appl. Phys. Lett.* **91**, 092101 (2007)
- [77] W. M. Linhart, T. D. Veal, P. D. C. King, G. Koblmüller, C. S. Gallinat, J. S. Speck, and C. F. McConville, *Appl. Phys. Lett.* **97**, 112103 (2010)
- [78] T. D. Veal, L. F. J. Piper, M. R. Phillips, M. H. Zareie, H. Lu, W. J. Schaff, and C. F. McConville, *Phys. Stat. Sol. A* **203**, 85 (2006)
- [79] P. D. C. King, T. D. Veal, and C. F. McConville, *Phys. Rev. B* **77**, 125305 (2008)

- [80] D. Segev and C. G. Van de Walle, Surf. Sci. **601**, L15 (2007)
- [81] D. Segev and C. G. Van de Walle, J. Cryst. Growth **300**, 199 (2007)
- [82] D. Segev and C. G. Van de Walle, Europhys. Lett. **76**, 305 (2006)
- [83] C.-L. Wu, H.-M. Lee, C.-T. Kuo, C.-H. Chen, and S. Gwo, Phys. Rev. Lett. **101**, 106803 (2008)
- [84] C. S. Gallinat, G. Koblmüller, J. S. Brown, S. Bernardis, J. S. Speck, G. D. Chern, E. D. Readinger, H. Shen, and M. Wraback, Appl. Phys. Lett. **89**, 032109 (2006)
- [85] W. Walukiewicz, Physica B **302**, 123 (2001)
- [86] S. X. Li, K. M. Yu, J. Wu, R. E. Jones, W. Walukiewicz, J. W. Ager III, W. Shan, E. E. Haller, H. Lu, and W. J. Schaff, Phys. Rev. B **71**, 161201 (2005)
- [87] J. Oila, A. Kemppinen, A. Laasko, K. Saarinen, W. Egger, L. Liszkay, P. Sperr, H. Lu, and W. J. Schaff, Appl. Phys. Lett. **84**, 1486 (2004)
- [88] W. Walukiewicz, R. E. Jones, S. X. Li, K. M. Yu, J. W. Ager III, E. E. Haller, H. Lu, and W. J. Schaff, J. Cryst. Grow. **288**, 278 (2006)
- [89] P. D. C. King, T. D. Veal, and C. F. McConville, J. Phys.: Condens. Matt. **21**, 174201 (2009)
- [90] C. Stampfl, C. G. Van de Walle, D. Vogel, P. Krüger, and J. Pollman, Phys. Rev. B. **61**, R7846 (2000)
- [91] A. Janotti and C. G. Van de Walle, *Theory of native point defects and impurities in InN*, by T. D. Veal, C. F. McConville and W. J. Shaff (Eds) (CRC Press, 2009) pp. 419–444
- [92] W. Götz, R. S. Kern, C. H. Chen, H. Liu, D. A. Steigerwald, and Fletcher, Mat. Sci. Eng. B **59**, 211 (1999)

- [93] P. R. Hageman, W. J. Schaff, J. Janinski, and Z. Liliental-Weber, *J. Cryst. Growth* **267**, 123 (2004)
- [94] M. L. Colussi, R. J. Baierle, and R. H. Miwa, *J. Appl. Phys.* **110**, 033709 (2011)
- [95] K. M. Tracy, W. J. Mecouch, R. F. Davis, and J. Nemanich, *J. Appl. Phys.* **94**, 3163 (2003)
- [96] N. S., T. Mukai, M. Senoh, and N. Iwasa, *Jpn.J. Appl. Phys.* **31**, L139 (1992)
- [97] B. A. Hull, S. E. Mohney, H. S. Venugopalan, and J. C. Ramer, *Appl. Phys. Lett.* **76**, 2271 (2000)
- [98] X. Zhang, S. J. Chua, P. Li, K. B. Chong, and W. Wang, *Appl. Phys. Lett.* **73**, 1772 (1998)
- [99] M. E. Zvanut, Y. Uprety, J. Dashdorj, M. Moseley, and W. A. Doolittle, *J. Appl. Phys.* **110**, 044508 (2011)
- [100] J. H. Chai, T. H. Myers, Y. W. Song, R. J. Reeves, W. M. Linhart, R. J. H. Morris, T. D. Veal, M. G. Dowsett, C. F. McConville, and S. M. Durbin submitted to *J. Vac. Sci. Tech. B*
- [101] P. P. Chen, H. Makino, and T. Yai, *J. Cryst. Growth* **269**, 66 (2004)
- [102] A. Ney, R. Rajaram, E. Arenholz, J. S. Harris, M. Samant, R. F. C. Farrow, and S. S. P. Parkin, *J. Magn. Magn. Mater.* **300**, 7 (2006)
- [103] P. A. Anderson, C. H. Swartz, D. Carder, R. J. Reeves, S. M. Durbin, S. Chandril, and T. H. Myers, *Appl. Phys. Lett.* **89**, 184104 (2006)
- [104] J. W. Ager III, N. Miller, R. E. Jones, K. M. Yu, J. Wu, W. J. Schaff, and W. Walukiewicz, *Phys. Stat. Sol. B* **245**, 873 (2008)
- [105] P. D. C. King, T. D. Veal, H. Lu, S. A. Hatfield, W. J. Schaff, and C. F. McConville, *Surf. Sci.* **602**, 871 (2008)

- [106] L. R. Bailey, T. D. Veal, C. E. Kendrick, S. M. Durbin, and C. F. McConville, Appl. Phys. Lett **95**, 192111 (2009)
- [107] Y.-H. Chang, Y.-S. Lu, Y.-L. Hong, C.-T. Kuo, S. Gwo, and J. A. Yeh, J. Appl. Phys. **107**, 043710 (2010)
- [108] L. R. Bailey, T. D. Veal, and C. F. McConville, Phys. Stat. Sol. C **8**, 1605 (2011)
- [109] T. Chassé, H. Peisert, P. Streubel, and R. Szargan, Surf. Sci. **331-333**, 434 (1995)
- [110] C. J. Sandroff, R. N. Nottenburg, J.-C. Bischoff, and R. Bhat, Appl. Phys. Lett **51**, 33 (1987)
- [111] D. Y. Petrovykh, M. J. Yang, and L. J. Whitman, Surf. Sci. **523**, 231 (2003)
- [112] M. J. Lowe, T. D. Veal, C. F. McConville, G. R. Bell, S. Tsukamoto, and N. Koguchi, Surf. Sci. **523**, 179 (2003)
- [113] M. J. Lowe, T. D. Veal, A. P. Mowbray, and C. F. McConville, Surf. Sci. **544**, 320 (2003)
- [114] V. Y. Aristov, G. L. Lay, P. Soukiassian, K. Hricovini, J. E. Bonnet, J. Osvald, and O. Olsson, J. Vac. Sci. Technol. B **12**, 2709 (1994)
- [115] J. J. Mudd, T. D. Veal, and C. F. McConville, private communication.
- [116] B. K. Ridley, *Quantum Processes in Semiconductors* (Oxford Science Publications, 1993)
- [117] E. O. Kane, J. Phys. Chem. Solids **1**, 249 (1957)
- [118] B. Nag, *Electron Transport in Compound Semiconductors* (Springer-Verlag, 1980)
- [119] T. D. Veal, *High-Resolution Electron-Energy-Loss Spectroscopy of Narrow Gap III-V Semiconductor Surfaces and Interfaces*, Ph.D. thesis, University of Warwick (2002)

- [120] P. Carrier and S.-H. Wei, *J. Appl. Phys.* **97**, 033707 (2005)
- [121] R. Goldhahn, P. Schley, A. Winzer, G. Gobsch, V. Cimalla, O. Ambacher, M. Rakel, C. Cobet, N. Esser, H. Lu, and W. Schaff, *Phys. Stat. Sol. A* **203**, 42 (2006)
- [122] M. Suzuki and T. Uenoyama, *Jpn. J. Appl. Phys.* **35**, 543 (1996)
- [123] A. D. Andreev and E. P. O'Reilly, *Phys. Rev. B* **62**, 15851 (2000)
- [124] H. Lüth, *Solid Surfaces, Interfaces and Thin Films* (Springer, 2001)
- [125] G. Paasch and H. Übensee, *Phys. Stat. Sol. B* **113**, 165 (1982)
- [126] J.-P. Zöllner, H. Übensee, G. Paasch, T. Fiedler, and G. Gobsch, *Phys. Stat. Sol. B* **134**, 837 (1986)
- [127] D. P. Woodruff and T. A. Delchar, *Modern Techniques of Surface Science*, 2nd ed. (Cambridge University Press, 1994)
- [128] C. N. Berglund and W. E. Spicer, *Phys. Rev.* **136**, A1030 (1964)
- [129] S. Tanuma, C. J. Powell, and D. R. Penn, *Surf. Interface Anal.* **21**, 165 (1994)
- [130] D. A. Shirley, *Phys. Rev. B* **5**, 4709 (1972)
- [131] G. K. Woodgate, *Elementary Atomic Structure*, 2nd ed. (OUP, Oxford, 1980)
- [132] G. B. D. Briggs, *High Resolution XPS of Organic Polymers: The Scientia ESCA300 Database* (Wiley, New York, 1992)
- [133] U. Gelius, B. Wannberg, P. Baltzer, H. Fellner-Feldegg, G. Carlsson, C. G. Johansson, J. Larsson, P. Munger, and G. M. Vegerfors, *J. Electron Spectrosc. Relat. Phenom.* **52**, 747 (1990)
- [134] C. Pickering, *J. Phys. C* **13**, 2959 (1980)
- [135] D. W. Berreman and F. C. Unterwald, *Phys. Rev.* **174**, 791 (1968)
- [136] M. Schubert, T. E. Tiwald, and C. M. Herzinger, *Phys. Rev. B* **61**, 8187 (2002)

- [137] J. L. Ribeiro and L. G. Vieira, Eur. Phys. J. B **36**, 21 (2003)
- [138] C. C. Katsidis and D. I. Siapkas, Appl. Opt. **41**, 3978 (2002)
- [139] M. Born and E. Wolf, *Principles of Optics*, 7th ed. (Cambridge University Press, 1999)
- [140] C. L. Mitsas and D. I. Siapkas, Appl. Opt. **34**, 1678 (1995)
- [141] N. W. Ashcroft and N. D. Mermin, *Solid State Physics* (Saunders College, Philadelphia, 1976)
- [142] L. J. Van der Pauw, Philips Technical Review(1958)
- [143] P. Blood, Semicond. Sci. Technol. **1**, 7 (1986)
- [144] T. Ambridge and M. M. Faktor, J. Appl. Electrochem. **4**, 135 (1974)
- [145] A. Bard and L. Faulkner, *Electrochemical Methods: Fundamentals and Applications* (Wiley, 2001)
- [146] R. J. H. Clark and R. Hester, *Spectroscopy for Surface Science* (Wiley, 1998)
- [147] P. Sigmund, Phys. Rev. **184**, 383 (1969)
- [148] T. D. Veal, C. F. McConville, W. J. Shaff, and (Eds), *Indium Nitride and Related Alloys* (CRC Press, 2009)
- [149] E. Calleja, J. Grandal, M. A. Sánchez-García, M. Niebelshütz, V. Cimalla, and O. Ambacher, Appl. Phys. Lett. **90**, 262110 (2007)
- [150] S. Lazić, E. Gallardo, J. M. Calleja, F. Agulló-Rueda, J. Grandal, M. A. Sánchez-Garcia, E. Calleja, E. Luna, and A. Trampert, Phys. Rev. B **76**, 205319 (2007)
- [151] H. Lu, W. J. Schaff, L. F. Eastman, J. Wu, W. Walukiewicz, V. Cimalla, and O. Ambacher, Appl. Phys. Lett. **83**, 1136 (2003)
- [152] T. Nagata, G. Koblmüller, O. Bierwagen, C. S. Gallinat, and J. S. Speck, Appl. Phys. Lett. **95**, 132104 (2009)

- [153] G. Koblmüller, C. S. Gallinat, S. Bernardis, J. S. Speck, G. D. Chern, E. D. Readinger, H. Shen, and M. Wraback, *Appl. Phys. Lett.* **89**, 071902 (2006)
- [154] T. A. Komissarova, T. V. Shubina, V. N. Jemrik, S. V. Ivanov, L. I. Ryabova, D. R. Khokhlov, A. Vasson, J. Leymarie, T. Araki, and Y. Nanishi, *Semiconductors* **43**, 285 (2009)
- [155] S. P. Fu, T. J. Lin, W. S. Su, C. Y. Shieh, Y. F. Chen, C. A. Chang, N. C. Chen, and P. H. Chang, *J. Appl. Phys.* **96**, 126102 (2006)
- [156] V. Darakchieva, M. Schubert, T. Hofmann, B. Monemar, C.-L. Hsiao, T.-W. Liu, L.-C. Chen, W. J. Schaff, Y. Takagi, and Y. Nanishi, *Appl. Phys. Lett.* **95**, 202103 (2009)
- [157] A. Janotti and C. G. Van de Walle, *Appl. Phys. Lett.* **92**, 032104 (2008)
- [158] G. Koblmüller, A. Hirai, F. Wu, C. S. Gallinat, G. D. Metcalfe, H. Shen, M. Wraback, and J. S. Speck, *Appl. Phys. Lett.* **93**, 171902 (2008)
- [159] G. Koblmüller, G. D. Metcalfe, M. Wraback, F. Wu, C. S. Gallinat, and J. S. Speck, *Appl. Phys. Lett.* **94**, 091905 (2009)
- [160] R. Goldhahn, P. Schley, and M. Röppischer, *Ellipsometry of InN and related alloys in Indium Nitride and Related Alloys*, by T. D. Veal, C. F. McConville and W. J. Shaff (Eds) (CRC Press, 2009) pp. 315–375
- [161] P. D. C. King, T. D. Veal, C. S. Gallinat, G. Koblmüller, L. R. Bailey, J. S. Speck, and C. F. McConville, *J. Appl. Phys.* **104**, 103703 (2008)
- [162] S. A. Chambers, T. Droubay, T. C. Kaspar, and M. Gutowski, *J. Vac. Sci. Technol. B* **22**, 2205 (2004)
- [163] C. G. Van de Walle and D. Segev, *J. Appl. Phys.* **101**, 081704 (2007)
- [164] T. D. Veal, P. D. C. King, M. Walker, C. F. McConville, H. Lu, and W. J. Schaff, *Physica B* **401**, 351 (2007)

- [165] T. D. Veal, P. D. C. King, P. H. Jefferson, L. F. J. Piper, C. F. McConville, H. Lu, W. J. Schaff, P. A. Anderson, S. M. Durbin, D. Muto, H. Naoi, and Y. Nanishi, Phys. Rev. B **76**, 075313 (2007)
- [166] Y. Ishitani, X. Wang, S.-B. Che, and A. Yoshikawa, J. Appl. Phys. **103**, 053515 (2008)
- [167] C. Stampfl, C. G. Van de Walle, D. Vogel, P. Krüger, and J. Pollmann, Phys. Rev. B **61**, R7846 (2000)
- [168] L. F. J. Piper, T. D. Veal, C. F. McConville, H. Lu, and W. J. Schaff, Appl. Phys. Lett. **88**, 252109 (2006)
- [169] V. Lebedev, V. Cimalla, T. Baumann, O. Ambacher, F. M. Morales, J. G. Lozano, and D. González., J. Appl. Phys. **100**, 094903 (2006)
- [170] X. Wang, S.-B. Che, Y. Ishitani, and A. Yoshikawa, Appl. Phys. Lett. **90**, 151901 (2007)
- [171] X. Wang, S.-B. Che, Y. Ishitani, and A. Yoshikawa, Appl. Phys. Lett. **90**, 201913 (2007)
- [172] J. W. L. Yim, R. E. Jones, K. M. Yu, J. W. Ager III, W. Walukiewicz, W. J. Schaff, and J. Wu, Phys. Rev. B **76**, 041303 (2007)
- [173] X. Wang, S.-B. Che, Y. Ishitani, A. Yoshikawa, H. Sasaki, T. Shinagawa, and S. Yoshida, Appl. Phys. Lett. **91**, 081912 (2007)
- [174] N. Khan, N. Nepal, A. Sedhain, J. Y. Lin, and H. X. Jiang, Appl. Phys. Lett. **91**, 012101 (2007)
- [175] X. Wang, S.-B. Che, Y. Ishitani, and A. Yoshikawa, Appl. Phys. Lett. **91**, 242111 (2007)
- [176] X. Wang, S.-B. Che, Y. Ishitani, and A. Yoshikawa, Appl. Phys. Lett. **92**, 132108 (2008)

- [177] L. H. Dmowski, M. Baj, T. Suski, J. Przybytek, R. Czernecki, X. Wang, A. Yoshikawa, H. Lu, W. J. Schaff, D. Muto, and Y. Nanishi, *J. Appl. Phys.* **105**, 123713 (2009)
- [178] S. F. Ding, X. P. Qu, and G. H. Fan, *Physica B* **404**, 1279 (2009)
- [179] N. Miller, J. W. Ager III, H. M. Smith, M. A. Mayer, K. M. Yu, E. E. Haller, W. Walukiewicz, W. J. Schaff, C. S. Gallinat, G. Koblmüller, and J. S. Speck, *J. Appl. Phys.* **107**, 113712 (2010)
- [180] N. Ma, X. Q. Wang, F. J. Xu, N. Tang, B. Shen, Y. Ishitani, and A. Yoshikawa, *Appl. Phys. Lett.* **97**, 222114 (2010)
- [181] H. Ahn, K.-J. Yu, Y.-L. Hong, and S. Gwo, *Appl. Phys. Lett.* **97**, 062110 (2010)
- [182] K. Wang, N. Miller, R. Iwamoto, T. Yamaguchi, M. A. Mayer, T. Araki, Y. Nanishi, K. M. Yu, E. E. Haller, W. Walukiewicz, and J. W. Ager III, *Appl. Phys. Lett.* **98**, 042104 (2011)
- [183] E. Alarcón-Lladó, M. A. Mayer, B. W. Boudouris, R. A. Segelman, N. Miller, T. Yamaguchi, K. Wang, Y. Nanishi, E. E. Haller, and J. W. Ager III, *Appl. Phys. Lett.* **99**, 102106 (2011)
- [184] N. Miller, J. W. Ager III, R. E. Jones, H. M. Smith III, M. A. Mayer, K. M. Yu, M. E. Hawkridge, Z. Liliental-Weber, E. E. Haller, W. Walukiewicz, W. J. Schaff, C. S. Gallinat, G. Koblmüller, and J. S. Speck, *Physica B* **404**, 4862 (2009)
- [185] P. D. C. King, *Charge Neutrality Level in Significantly Cation-Anion Mis-matched Semiconductors*, Ph.D. thesis, University of Warwick (2009)
- [186] A. Venter, P. Shamba, L. Botha, and J. Botha, *Thin Solid Films* **517**, 4468 (2009)
- [187] M. D. Pashley, K. W. Haberern, R. M. Feenstra, and P. D. Kirchner, *Phys. Rev. B* **48**, 4612 (1993)

- [188] J. Tersoff, Phys. Rev. B **32**, 6968 (1985)
- [189] W. Mönch, Appl. Surf. Sci. **117**, 380 (1997)
- [190] L. Plucinski, L. Colakerol, S. Bernardis, Y. Zhang, S. Wang, C. O'Donnell, K. E. Smith, I. Friel, and T. D. Moustakas, Surf. Sci **600**, 116 (2006)
- [191] L. A. Fishwick, W. M. Linhart, M. Walker, A. Stachel, T. D. Veal, H. Lu, W. J. Shaff, and C. F. McConville, *unpublished*
- [192] Y. Tao, A. Yelon, E. Sacher, Z. H. Lu, and M. J. Graham, Appl. Phys. Lett **60**, 2669 (1992)
- [193] Z. H. Lu, M. J. Graham, X. H. Feng, and B. X. Yang, Appl. Phys. Lett. **60**, 2773 (1992)
- [194] L. R. Bailey, T. D. Veal, P. D. C. King, C. F. McConville, J. Pereiro, J. Grandal, M. A. Sánchez-García, E. Muñoz, and E. Calleja, J. Appl. Phys. **104**, 113716 (2008)
- [195] W. B. Pearson, *A Handbook of Lattice Spacings and Structures of Metals and Alloys* (Pergamon Press, 1967)
- [196] M. Katayama, M. Aono, H. Oigawa, Y. Nannichi, H. Sugahara, and M. Ohshima, Jpn. J. Appl. Phys. **30**, L786 (1991)
- [197] A. Martí and G. L. Araújo, Solar Energy Materials and Solar Cells **43**, 203 (1996)
- [198] S. F. Chichibu, A. Uedono, T. Onuma, B. A. Haskell, A. Chakraborty, T. Koyama, P. T. Fini, S. Keller, S. P. DenBaars, J. S. Speck, U. K. Mishra, S. Nakamura, S. Yamaguchi, S. Kamiyama, H. Amano, I. Akasaki, J. Han, and T. Sota, Nature Mater. **5**, 810 (2006)
- [199] H. Komaki, T. Shimohara, K. Sakai, R. Katayama, K. Onabe, A. Fukuyama, and T. Ikari, Phys. Stat. Sol. C **5**, 499 (2008)

- [200] M. Moret, S. Ruffenach, O. Briot, and B. Gil, Eur. Phys. J. Appl. Phys. **45**, 20305 (2009)
- [201] Ö. Tuna and *et al.*, private communication.
- [202] O. Tuna, W. M. Linhart, E. V. Lutsenko, G. P. Yablonskii, T. D. Veal, C. F. McConville, C. Giesen, H. Kalisch, A. Vescan, and M. Heukens, J. Cryst. Growth, submitted(2012)
- [203] K. M. Tracy, W. J. Mecouch, R. F. Davis, and R. J. Nemanich, J. Appl. Phys. **94**, 3163 (2003)
- [204] T. D. Veal, P. H. Jefferson, L. F. J. Piper, C. F. McConville, T. B. Joyce, P. R. Chalker, L. Considine, H. Lu, and W. J. Schaff, Appl. Phys. Lett. **89**, 202110 (2006)
- [205] P. D. C. King, T. D. Veal, A. Adikimenakis, H. Lu, L. R. Bailey, E. Iliopoulos, A. Georgakilas, W. J. Schaff, and C. F. McConville, Appl. Phys. Lett. **92**, 172105 (2008)
- [206] T. Inushima, M. Higashiwaki, and T. Matsui, Phys. Rev. B **68**, 235201 (2003)
- [207] T. D. Veal, L. F. J. Piper, W. J. Schaff, and C. F. McConville, J. Cryst. Growth **288**, 268 (2006)
- [208] M. V. Kisim, B. L. Gelmont, and S. Luryi, Phys. Rev. B **58**, 4605 (1998)
- [209] G. Yu, N. L. Rowell, and D. J. Lockwood, J. Vac. Sci. Technol. A **22**, 1110 (2004)